Stony Brook University

Co-Design of Wireless Power Transfer and Data Links for Next Generation Passive Devices

A Dissertation Presented

by

Jinghui Jian

to

The Graduate School

in Partial Fulfillment of the Requirements

for the Degree of

Doctor of Philosophy

in

Electrical Engineering

Stony Brook University

December 2015

Stony Brook University

The Graduate School

Jinghui Jian

We, the dissertation committee for the above candidate for the
Doctor of Philosophy degree, hereby recommend
acceptance of this dissertation.

Milutin Stanaćević – Dissertation Advisor
Associate Professor, Department of Electrical and Computer Engineering

Sangjin Hong
Professor, Department of Electrical and Computer Engineering

Emre Salman
Assistant Professor, Department of Electrical and Computer Engineering

Perena Gouma
Professor, Department of Materials Science and Engineering

This dissertation is accepted by the Graduate School.

Charles Taber
Dean of the Graduate School

Abstract of the Dissertation

Co-Design of Wireless Power Transfer and Data Links for Next Generation Passive Devices

by

Jinghui Jian

Doctor of Philosophy

in

Electrical Engineering

Stony Brook University

2015

Microsystems that harvest ambient power for their operation have been present in RFID technology and implantable medical devices (IMDs) for couple of decades. With the recent applications under the framework of the Internet of Thing (IoT) and with miniaturization of implantable devices interest in these devices has significantly grown. Two of the critical subjects in the passive devices technology are wireless power transfer (WPT) and data link. The focus of this work is on two distinct applications: design of wireless power transfer for IMDs and backscatter-based tag-to-tag (BBTT) communication system.

Our goal in the design of WPT to IMDS is to deliver maximum power through optimization of the inductive coupling link without violating the regulation of the maximum tissue exposure to the electromagnetic (EM) field radiation. The adaptive transmitting coil array is investigated to reduce specific absorption rate (SAR) on the tissue and mitigate coil misalignment problem. Two analysis methods, traditional quasi-static method and full-wave analysis method, are discussed and combined to optimize the inductive link.

BBTT devices communicate by backscattering existing external excitation field,

which can come from multiple sources, e.g., dedicated exciters, WiFi access points, TV towers, cell phone towers. This is contrary to the traditional backscattering devices like RFID tags which are designed to communicate directly with an active reader leading to a centralized network focused on the reader. Focus of this work is on design of the analog front end (AFE) and the backscatter modulator (BM), which determine BBTT communication range and link robustness. We propose novel solutions to optimize architecture and parameters of the AFE and BM circuits for the unique BBTT link. Design of the BBTT prototype and the experimental results are presented.

Contents

List of Figures

List of Tables

Acknowledgements

I would like to thank all the people that ever help and support me through my whole graduate study.

First, my deepest gratitude goes to my advisor, Prof. Milutin Stanaćević, who gives excellent guidance and support to me through my graduate education. I was always inspired by his enthusiasm , wide knowledge and amazing ideas in this area. Without his help, I could never finish this tough work. I would also like to thank my the rest of my committee members, Prof. Hong, Prof. Salman and Prof. Gouma, for spending time for it and providing invaluable feedback.

I would like to thank team members in RIBBN group: Prof. Das, Prof. Djurić, Akshay, Prof. Stanaćević, Jihoon, Zhe and Yasha. It was very lucky for me to work with these genius people, and have the opportunity to work for the development of innovative network of next generation.

I would like to thank other members in integrated microsystems Lab lab: Xiao, Shuo, Yingkan, Yasha. Thank you for all the unwavering help and inspirations. I have learned a lot of things from your guys.

I would like to thank all my friends in Stony Book and Long Island. Thank you for your companies these years. Because of you, my graduate life here was never boring.

Last but not least, I would like to thank my family, especially my father and my mother,

who always give me unconditional love and support, let me chase my dream and never restrict me because I am a girl. No matter where I am and what I am going to face, I always know that you are my best backup.

This work was supported by National Science Foundation CAREER Award 0846265 and Award CNS 1405740.

Chapter 1

Introduction

1.1 Wireless power transfer for implantable devices

Since 1958, when Dr. Ake Senning [1], a pionieering Swedish surgeon, implanted the fully implantable artificial cardiac pacemaker into Arne H. W. Larsson, implantable medical devices (IMD) has become more and more important treatment method in modern medicine field and promising technique in health care industry. It relieves patient's illness, extends length of life and improve patient's life quality by managing and providing direct medical therapy to diseases within human body. Applications of IMDs penetrate into many areas of medical treatment. By delivering electrical pulses to heart muscles to regulate heart beating, artificial cardiac pacemakers treat heart abnormal rhythms and maintain the pace for heart. Implantable Cardioverter Defibrillators (ICDs) detect and treat ventricular tachyarrhythmias by sending a electrical shork directly to patient's heart to stop ventricular fibrillations. Recently pacemaker and ICD are combined together as one implantable device. Implantable drug delivery devices try to enhance therapy for diseases that require long time drug management by regularly delivering drugs to physiological target. Cochlear implant is

another popular and well-established electronic implants today. Relative research undergoing nowadays covers even wider fields, including RFID based drug intake monitoring system, neural recording and neurostimulators that can help relieve disorder like blindness, deafness, Parkinson's disease, etc.

One of the big problems that prevents the development of miniature size IMDs is the power source. Traditional wired power supply restrict patients' mobility by "tethering" patients to a single location with the wiring harness; besides, wires through skin increase the risk of body infection. Embedded battery may be a good option, and is the major energy source for many IMDs nowadays, like cardiac pacemakers and drug delivery devices. However, because of the limit battery power density, restriction on size of the IMDs limit its efficiency and available energy amount; also implanted batteries have the issues of corrosion and require regular replacement every several years.

To solve this problem a different set of power harvesting technologies or energy scavengers were proposed [2]. Some popular harvesting technologies have developed ground on biological mechanism, such as kinetic harvesters which obtain energy from human motion [3, 4], thermoelectric generator that can generate energy by exploiting excess heat within or around human body [5], full cells utilizing biochemicals inside the body to generate power through electrochemical reactions [6] and infrared radiation harvesting, ultrasound energy harvesting.

The solution that has received the most attention in the last decade is the wireless power transmission (WPT). WPT is not a newly-emerged idea, and has been proposed and proved by Nikola Tesla as early as 1899 [7]. Even the concept of applying this technology into IMDs has emerged nearly half century ago [8–12]. WPT technology powers the IMDs by placing an external antenna outside body, generating electromagnetic (EM) or radio frequency (RF) field which can penetrate human body and delivery EM power to implanted devices. Electrically small loop shaped antenna is preferable option, since compared with

antennas of other shape, EM field produced by loop or a coil will have magnetic field (H-field) predominate over electric field (E-field), and H-field will have less effort and be less affected by human body as compared to E-field. In the near field, bounded to the distance of $d = \lambda/2\pi$ from the antenna, energy is stored in the EM field, which means that the energy can be absorbed by any coupling object within this region. Thus the wireless power transfer from external antenna to the inside the body antenna goes through a near-field inductive link. Besides providing energy to in vivo IMDs, near-field inductive link also serves as a data transmission channel through a technique called backscattering.

This work will focus on the investigation of WPT link for IMDs, particularly those implanted device like RFID based drug intake monitoring system and deep-brain recording and stimulation implant. The remainder of this chapter provides motivation for these systems as a particular examples of WPT to miniature implanted devices.

1.1.1 Drug Intake Monitoring System

RFID technology is an automatic, contactless identification system, which utilize electromagnetic fileds as the medium transmitting data for the purpose of identification without physically contact. RFID system usually consists of two parts: RFID reader - which plays a role of interrogator by observing nearby environment and deliver the observation results back to computer or microprocessor for processing, and RFID tags, which are data carrying devices, usually small enough to be attached to the object and can be tracked or identified by reader. The advantages of miniaturization, flexibility, convenience and low cost to made the tags ubiquitous made this technology quite popular in plenty of areas. Currently RFID technology is being used for wide variety of applications ranging from inventory control to automatic tracking systems; here we spread its usage into health care area.

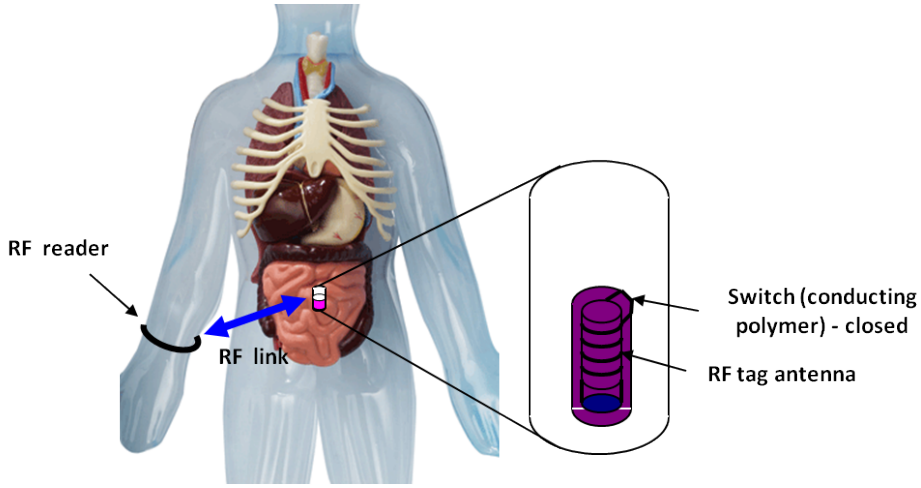

Figure 1.1: Envisioned system for drug intake monitoring system

System Overview

The main task of our project is to demonstrate a system containing RFID tag that is inserted in a pill and enables monitoring of ingestion of medicine and absorption into the body to insure proper dosage control and usage. The designed system will be able to reliable detect if the patient has taken a certain medication and dosage. The envisioned system is shown in Fig. 1.1.

Tag inside the pill:

Pills with medicine inside usually come in similar shapes, with different sizes, with diameter of 5 mm and length ranging from 10 mm to 22 mm. We envision using a small passive RFID tag embedded into a capsule that is inserted into the pill, as illustrated in Fig. 1.2. The RFID tag will be encapsulated with biocompatible material insoluble in gastrointestinal (GI) tract. Typical RFID tag contains an antenna, a microchip and sometimes a battery. Microchip is used to store unique identifying data which indicates the pill's identification and will be conveyed to the reader. In the passive tag, no battery is used and the power comes from radiating RF signal generated by the reader. In the case of active tag, that incorpo-

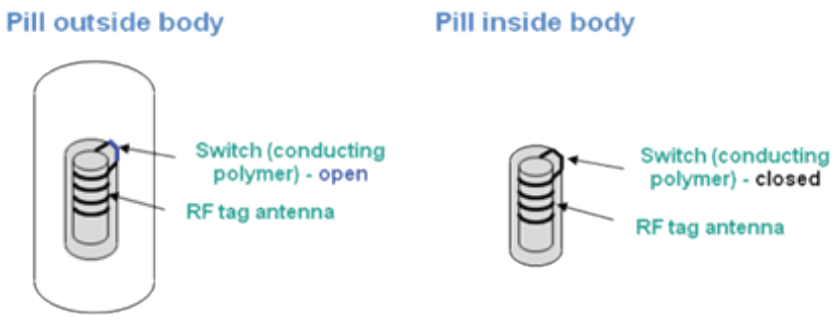

Figure 1.2: pill with RFID tag inside

rates nanobattery, extended maximum detection distance between tag and the reader can be provided, as well as reduced size of the reader antenna for the fixed detection distance. However, in our case addition of battery will increase the volume of tag, the cost of the system, and what's more important could be critical for health of patient and disposal of the tag. Hence passive tag without battery is preferrable here.

To enable detection of the antenna in the body, tag's antenna has to be active only when it is inside the body, while outside the body it should be inactive. To achieve this goal, conducting polymer will be included in electrical circuit of antenna. On the small part of the surface of capsule, a conductive polymer will be deposited that will be in part of electrical circuit of tag's antenna. Conductive polymer will be the only part of the tag electrical circuit that will be exposed to the body. As illustrated in Fig. 1.2, the polymer would be conductive only in the body when a certain level of pH value, characteristic for the body fluids, is detected and that would be the only time when tag antenna could transmit the signal to the reader. In the case that multiple capsules with RFID tags are present in the body, the system would still be able to distinguish them based on their unique identification stored in tag.

We also need to pay attention to how to disposal of tag from the body after the detection of the pill. The capsule that contains the tag needs to be small enough to easily pass through

GI tract. Small tag can then be discharged from the body, without any additional harmful effects, as well as the case of accumulation in the body a few tags over a course of couple of days. The potential accumulation of capsules in the digestive tract over a period of several days should not pose a threat to the health of the patient.

Reader:

The reader has to be able to detect tag in the body and store the identification information on the ingested pill, together with time stamp, time at which the pill was taken. The stored information in the reader will be readout after certain time, and presented to the doctor at the time of patients visit. This device must be fashioned in some way that makes it easy for the patient to wear on the body. Possible ideas include a necklace/pendant or a device that can be clipped to the belt or a waistband. In this way, the patient would only have to wear this device when they are taking their medication, and could leave it elsewhere for the rest of the day. This transmitter will only be activated at time when it is used by the patient. Once activated, this reader will "search" for the tag's transmitter. When the pill is detected, this device will store that information. This device could also beep in order to notify patient that it has successfully detected ingestion of the pill and that the patient can now safely remove the device. Once the information has been stored, this device will turn off. If the pill is not detected for a certain amount of time after reader has been activated, the device will turn off to save power, as it will be battery operated. Since a bottle of pills can last patients over a month, the reader will have to last the same amount of time.

Proposed Monitoring System Operation

From previous description, it's not hard to locate two main factors that form the challenges to the design of the drug monitoring system: the size restriction and safety issue. Size restriction comes from the restricted physical size of tag antenna defined by pill, as

well as the size of reader antenna which need to be fashioned in a way that makes it easy for the patient to take and use during daily life. Also under such conditions, the maximum achievable distance at which the reader can detect the presence of tag has to extend beyond the distance between RFID tag inside the body and external reader. Small size of antennas and relatively long reading distance dramatically weaken the coupling degree between reader and tag. What is even worse, human body as the medium between tag and reader further attenuate or detune the EM field. Moreover for passive tags will be served in our drug monitoring system due to the safety reasons stated above, the power needed for wakening up the tag and sending back tag information to external reader, comes all the way from EM field generated by the antenna. Strict size constriction on antenna sizes make the design of efficient wireless power link very critical.

The second factor is the safety issue. Not only attenuate and thus weaken the coupling between reader and tag, human body also brings up another challenge to the design of the system. Human safety and health issue is a big concern during designing a system relating exposure of human body to EM field. Restrictions on EM fields prevent human beings from excess exposure, but also limit the magnetic field available for tags, thus limit the power that tag circuit can utilize.

All these factors will cause energy starvation on tag circuit. Conventional methods to relieve this problem is, first, to design designed low-power operation circuitry for tag chip function to lower the demand of extractable power; second, to optimize the geometries of both coils to achieve highest possible power transfer efficiency for wireless power transfer link. Reasonable and efficient as these two method are, they may still can not liberate the tag deeply inside the body from such harsh energy scarcity environment. Thus we are thinking about applying a noval communication strategy "dual-phase mode", as we'll explain below, to the system.

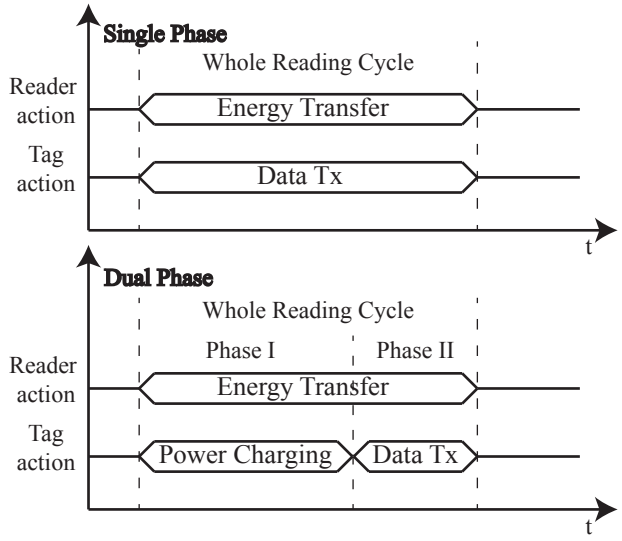

Figure 1.3: "Single phase" and "dual phase" compare

For conventional RFID or most IMD(implanted medical device) involved biomedical system, continuous high rate data communication exists between tag/IMD and external reader, then high efficient power link is needed to provide sustainable power to maintain such continuous data transmission. For those systems, tags or IMDs usually have just one single phase during one complete communicating cycle and realize simultaneous energy transfer and data transmission operations; since they can response the external reader or transmitter almost immediately when they receive the power and command due to high enough extracted power from RF field. But in our system, long reading distance, body attenuation effort and safety issues may make the received power not reaching tag minimum requirement for operation star-up, and also support for continuous large amount data transmission is not very essential in our case; therefore considering these factors, we divide the whole procedure into two phases: power charging phase and response phase, and call it "dual phase operation". See Fig. 1.3 for a comparison of single phase and dual phase operation.

The operation procedure is depicted in Fig. 1.3: tag starts first phase as soon as receiving

the power from external reader through the EM field, power management sector in tag chip keeps on extracting power from the field and stores it in a large capacitor C_{store}; at the same time a power detector monitors voltage level in the capacitor and the rest operation circuit just stands by and consume almost no power during this phase; when enough power is stored, the tag chip will move forward to next response phase, and stored energy is used to send identification data back to reader. This method compensates for deficiency of loosely coupled wireless power link with the small available power received by the tag.

1.1.2 Deep Brain Implanted Device

A highly invasive implantable devices are used for the deep-brain stimulation, a method proven to be the best treatment for tremor type diseases like Parkinson disease and epilepsy. The current devices comprise four closely spaced electrodes located in the deep brain and connected by the wire through the body to the chest implanted device containing the stimulation control circuitry and the rechargable battery as the power source. We propose a design of the deep-brain implantable device as a single integrated device that would harvest power from the external antenna, record the concentration of the neurotransmitter molecules for monitoring and the stimulation controller.

To achieve deep brain implantation, the size of the device is the most stringent constraint due to the limited area available in the local region of the brain. A single IC negates the need for wires that connect the electrodes to the pulse generator within the chest, significantly reducing the risk of infection due to the invasiveness of the surgical procedure. Furthermore, a tiny implant mitigates issues encountered during the implantation process, in addition to providing a more robust and longer *in vivo* monitoring and stimulation capability since the microsystem is less sensitive to body movements.

Due to the increased distance between the external and implanted antennas, the medium between antennas and the sizing constraints of the implantable design, design of the power harvesting system becomes quite challenging. We will demonstrate the feasibility of the power harvesting link and propose techniques for the link optimization.

1.2 Backscatter-based tag-to-tag communication (BBTT) systems

The practical object of 'Internet of Things' (IoT) is to connect all the object into a network under a common framework irrespective of the sizes or values. However, its ubiquitous deployment has been restricted by the power requirement, manufacture cost of each network nodes, and then the scalability of the network. A conventional way is to combining low-power micro-controller/CPU and RF transceivers for nodes in IoT, which, however, is considered power hungry because of the on-board radio transceiver. The commercially available off-the-shelf radio transceivers specially designed for the purpose of embedded RF devices consumes at least at the order of mW even during idle (listening) and tens of mW when actively transmitting or receiving, which is at least two orders of magnitude higher than power consumption of commercially available microcontrollers in equivalent states (CPU idle and CPU active modes). At the same time, use of active radio components leads to higher cost of manufacture and necessitates the use of on-board batteries, which require a significant future management.

Backscatter-based tag-to-tag communication (BBTT) is a innovative communication paradigm wherein radio-less devices communicate with each other purely using passive backscatter modulation. Its concept was first brought up by Nikitin [13] and the com-

munication link was first studied and presented in [14]. This makes for highly inexpensive and low power consumption devices, and thus draws great antention in recent years. By building a network based on BBTT communication, the tags talk to each other by backscattering existent external excitation signal, the source which can be dedicated continuous wave (CW) exciters or ambient EM field sources like WiFi access points [15], TV towers [16], cell phone towers, etc.

The general goal of our work is to extend backscattering to its logical extreme, enabling the tags themselves to read and interpret the backscattered communications from other neighboring tags and backscattering the information back, so that conventional active radio transmitters are no longer required. Starting from this idea, we combine this BBTT communication paradigm and multihop communication, leading to a form of multihop network of tags as shown in Fig. 1.4, which will allow for building low-cost networks with great scalability and flexibility. This type of communication networks is very promising in exploring the vast potential of the Internet of Things. A gateway or sink node can connect this network to an external IP network as needed. The initial feasibility of this type of tag-to-tag communication has been demonstrated by our prior work [17][18][19] as well as by others [16][15]. But these studies fall short of demonstrating a multihop relaying operation. Our BBTT communication network also overcomes a phase cancellation phenomenon that occurs uniquely in all backscattering tag-to-tag links that these prior works did not address.

The dedicated CW exciters in our network provide power and backscattering media for tags in BBTT network. Here the exciters only provides RF fields nad has no intelligence, unlike conventional RFID readers. Thus, the number of exciter deployed and manufacture cost can be greatly reduced, and they can be easily integrated into the infrastructure of future as a standard practice.

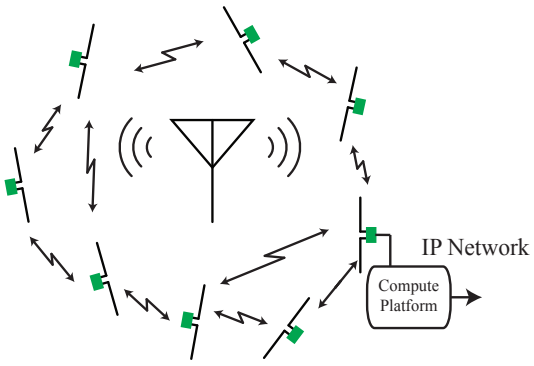

Figure 1.4: BBTT multihop network

1.3 Organization

The whole dissertation is organized as follows. In Chapter 2, we focus on the WPT link design between deeply implanted medical devices and external transmitter and propose techniques for improving the power efficiency and the maximum power delivery. After briefly introducing two kinds of analysis method - quasi-static analysis and full-wave analysis - for WPT link and related design issue, we investigate the optimum frequency and positioning of the transmitting coil to maximize the available power for deeply implanted devices. Then we investigate the an adaptive transmitter coil array and evaluate the performance of the WPT link to see the link performance change with the modification of the coil structure and how the adaptive phase difference will mitigate the SAR issue and misalignment between the transmitting and receiving coil.

Then in Chapter 3, we brief introduce the BBTT communication system and compare it with conventional RFID system. After comparing basic block module for the tag design in the two systems, we focus on analog front end (AFE) and backscatter modulator (BM) design which are critical to build up a reliable and long-range communication link. We will establish the analytical equations for phase cancellation problem happened in general BBTT

system and propose multi-phase backscattering as the solution. Then we will illustrate the co-design of power harvester part and detector part to co-optimize the power efficiency and detection sensitivity. In the last part of Chapter 3, the prototype of the BBTT tag and experiment result will be demonstrated.

Finally, conclusion and future work will be shown in Chapter 4.

Chapter 2

Wireless Power Link Design for Implantable Medical Devices

2.1 Introduction

The idea of using wireless power transmission(WPT) through biological tissue as a power supply for implantable device in biomedical engineering was brought up decades ago, and now became an important technique for biomedical engineering. Studies in early years, until several years ago, mainly focused on WPT operating at low frequencies usually less than 10 or 20MHz [10–12, 20–22], since it was widely believed that electromagnetic(EM) field tend to attenuate more through biological tissue at high frequencies than low frequencies. Corresponding research techniques based on quasi-static analysis and non-ideal transformer models representing coils pair were used as the mainstream methods. But when low-frequency operation applied to implantable devices with small sizes and relatively long transmission distance, the power link performance between the external transmitter and internal receiver was very poor. Recently, A. Poon et al. pointed out the limitation of quasi-static analysis

when dealing with WPT through biological tissue, re-examined the whole issue using full-wave analysis method over broad frequency range and stated that optimal frequency exists for WPT efficiency through biological tissue as medium and can be in the GHz-range for mm-size implantable devices [23, 24]. This led more researchers to examine WPT link at high frequencies and design the link with full-wave simulator [25–27].

In this chapter, we will shortly discuss these two different analysis methods - the quasi-static analysis and full-wave analysis - in the study of WPT problem, as well as the dielectric model for biological tissue, and then some important design considerations will be addressed, including WPT link efficiency, safety issues regarding EM field exposure, maximum available power for implantable devices and misalignment situation between the two coils. After the brief introduction of WPT link analysis method and related design consideration, we are going to combine these two methods together to seek a way to deliver maximum power to IMDs without violating the regulation of the maximum tissue exposure to the electromagnetic (EM) field radiation by adjusting the coil parameters and the position of the external coil. The adaptive transmitting coil array is investigated for reducing specific absorption rate (SAR) generated by the coils on the tissue and mitigate Rx coil misalignment problem. In the last part, different types of rectifier for power harvesting through EM field for IMDs will be talked about and evaluated.

2.2 EM model for wireless link of implantable devices

Before we start designing wireless link for implantable devices, we will discuss a little bit of EM properties of biological tissue, which will affect the whole model building, wireless link performance and design.

It's very easy to derive the relationship between electric field and magnetic field from

Maxwell's equations (the details of derivation is shown in Appendix A):

$$\nabla \times \mathbf{H} = j\omega\epsilon_0 \left(\epsilon' - j\epsilon'' - j\frac{\sigma}{\omega\epsilon_0}\right)\mathbf{E}, \tag{2.1}$$

the relationship between E and H is influence by total complex relative permittivity ϵ_{tot} of the medium:

$$\epsilon_{tot} = \epsilon' - j\left(\epsilon'' + \frac{\sigma}{\omega\epsilon_0}\right). \tag{2.2}$$

Then biological tissue can be treated as linear, isotropic and dispersive lossy dielectric.

Tissue dielectric property is modeled to the summation of five Debye relaxations for different frequencies, and its total relative permittivity is given in [28]:

$$\epsilon_{tot}(\omega) = \epsilon_\infty + \sum_{n=1}^{5} \frac{\Delta\epsilon_n}{1 + j\omega\tau_n} + \frac{\sigma}{j\omega\epsilon_0} \tag{2.3}$$

where ϵ_∞ is the permittivity at frequency $\omega\tau >> 1$. $\Delta\epsilon = \epsilon_s - \epsilon_\infty$ represents Debye dispersion magnitude at different frequency region. But the multiple Debye relaxation model cannot precisely describe dielectric characteristic of tissue; then by broadening each dispersion region, a modification of (2.3), known as Cole-Cole equation, is also given in [28]:

$$\epsilon_{tot}(\omega) = \epsilon_\infty + \sum_{n=1}^{5} \frac{\Delta\epsilon_n}{1 + (j\omega\tau_n)^{1-\alpha_n}} + \frac{\sigma}{j\omega\epsilon_0} \tag{2.4}$$

where α_n is the distribution parameter for every dispersion region.

2.2.1 Quasi-static Analysis

Solving a complete set of Maxwell's equations can be quite difficult and sometimes unnecessary. Like many engineering problems, some approximations methods can be applied to

simplify the equation sets and solving procedures when certain conditions are satisfied. One type of approximations for Maxwell's equations is quasi-static approximation, which includes magnetic quasi-static (MQS) and electric quasi-static (EQS) [29]. One thing that complicates the equation sets is the double coupling between the electric field and magnetic field in the curl equations. As a transition region between dynamic field and static field, quasi-static approximation allows us to keep one coupling form between electric field and magnetic field while neglecting another one. For coil carrying low frequency alternating current, if the coil size is considered as electrically small (less than tenth of the wavelength by rule of thumb), then the current distributed along the coil will be viewed as constant every moment, as well as the magnetic field generated by this "quasi-static" current. Such situation satisfies MQS condition, then the time-dependent component $j\omega\mathbf{D}$ in Maxwell-Ampere's law is neglected, simplifying (A.1b) to:

$$\nabla \times \mathbf{H} = \mathbf{J}, \tag{2.5}$$

which is actually the static form of Ampere's law. However, Faraday's law (A.1a) still keeps the same to maintain the coupling between E-field and H-field here, that is why it is called magnetic quasi-static approximation.

Another reason supporting use of MQS for low frequencies is that, under frequency below 20MHz, the interaction between EM field and biologic material is not so obvious, thus the effect of tissue on WPT link is trivial. Considering all these factors, one single coil can be viewed as a non-ideal inductor, and the pair of coils can be modeled as a non-ideal transformer, the coupling between which is purely inductive, and lumped element circuit model for transformer is applied.

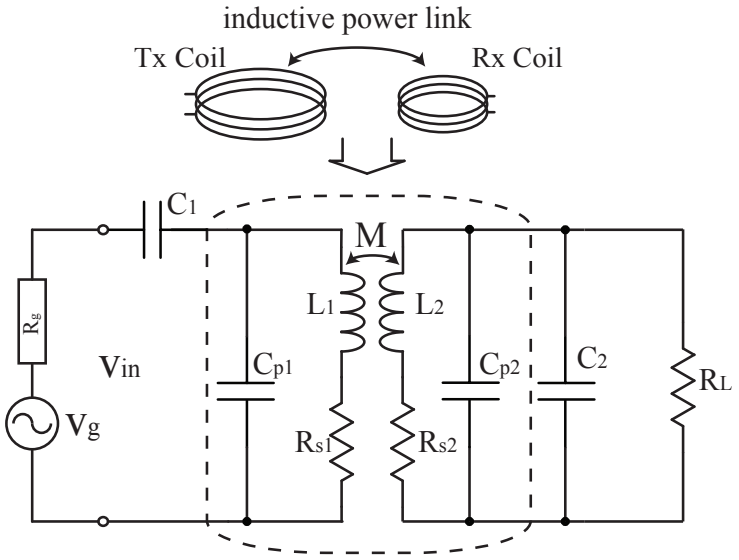

Figure 2.1: Simplified RLC lumped element model of inductive two-coil link.

Non-ideal transformer model of inductive link

As stated above, pair of coils used in the wireless power link can be viewed as a non-ideal transformer with the RLC lumped models for the transformer elements. The most commonly used RLC model for the coil is represented with an inductor L in series connection with the parasitic series resistor R_s, modeling the wire resistance loss, and additional parallel shunt capacitor C_p modeling the all parasitic capacitances associated with the coil. Fig.2.1 shows a WPT system with both coils represented using this RLC model. Coupling link between inductor L_1 and L_2 is considered as purely inductive. The V-I relation for a non-ideal transformer is illustrated in Fig.2.2 and expressed by following equations in the phasor form:

$$V_1 = j\omega L_1 I_1 + j\omega M I_2 \tag{2.6a}$$

$$V_2 = j\omega M I_1 + j\omega L_2 I_2 \tag{2.6b}$$

where M is the mutual inductance between the coils, namely L_1 and L_2. Due the symmetry of these two equations and the isomorphous relationship between the equation elements and the normal inductance, T-network circuit model with only ordinary inductors with inductance values shown in Fig.2.2 can be used as another way to represent the transformer [30].

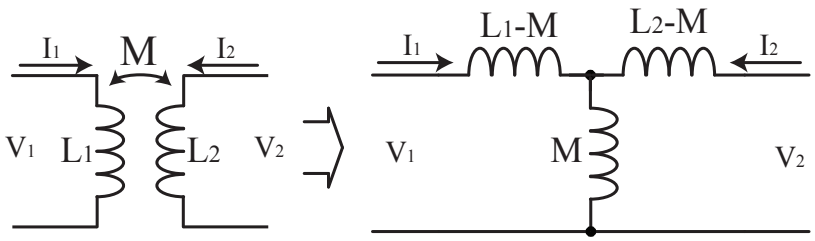

Figure 2.2: Lossless non-ideal transformer model and its T-version

Besides using mutual inductance M to describe the coupling situation, a new term *coupling coefficient* k is defined for describing the coupling degree between the coils and expressed as

$$k = \frac{M}{\sqrt{L_1 L2}}. \tag{2.7}$$

The magnitude of k varies between 1 and 0: "1" stands for the ideal situation when two inductors are completely coupled without any leakage, while "0" represents the worst situation that no coupling exists at all. This term is very important and used a lot in quantitative analysis procedure.

With lumped element model of the coils, it is easy to solve circuit shown in Fig. 2.1, and the whole solving procedure is very straight, fast-solving and space-saving, thus suitable for iterative calculation. In our work, we will use quasi-static analysis to help us gain an intuitive understanding of working theory of power transmission through coil pair.

2.2.2 Full-wave Analysis

Though calculations based on the quasi-static analysis are easy, quick and demonstrate excellent accordance with the experimental results for the low transmission frequency, the approximations become less accurate at the higher frequencies. With the term $j\omega\mathbf{D}$ being dismissed under quasi-static analysis, tissue-absorption effect is barely taken into account. Although some new models have been established to solve this problem by introducing tissue as a dielectric material layer [31], this modeling still has the limitations at the higher frequencies.

The full-wave analysis method is considering the coil pair as a general 2-port microwave network, it solves the whole set of Maxwell's equations over the whole structure by numerical method and extracts the network model from the result. Microwave network theory extended from conventional circuit concept can be used to deal with transcutaneous WPT link design. The model can be obtained by the full-wave EM solvers. Compared with quasi-static analysis, the full-wave analysis consumes more time and memory space in order to solve the Maxwell's equations; however, it provides more accurate simulation results, moreover it includes tissue influence on the power link and is suited for the broad band analysis. In our work, a commercial FEM (finite element method)-based full-wave electromagnetic field solver HFSS (high frequency structural simulator) is used to simulate and extract the network parameters - like Z-parameters and S-parameter - of the designed inductive links.

Besides, another advantage of full-wave analysis is able to calculate EM field at every point in the space under study, including complicated near-field and mid-field region. This analysis provides us with a good insight investigation of EM field pattern, which is quite essential for optimization of the coil structure for higher magnetic fields without violating constraints on human body exposed EM field.

Nowadays many EM solvers have parametric analysis and optimization module built-in to aid and greatly quicken design procedure; script language is also a powerful tool to control the solvers and facilitate procedure. In this project we use a FEM(finite element method)-based full-wave electromagnetic field commercial solver Ansoft HFSS (high frequency structural simulator) to simulate the coil pairs under investigation.

2.3 Design Consideration

2.3.1 Link efficiency and matching techniques

The overall power transfer efficiency ($\eta_{sys,ov}$) of the IMD system, which includes the external transmitter and the internal implantable receiver, is the product of the efficiency of the transmitter η_T, the power transfer efficiency η_C from transmitter(Tx) coil to receiver(Rx) coil and receiver efficiency η_R as shown in Fig 2.3:

$$\eta_{sys,ov} = \eta_T \eta_C \eta_R \tag{2.8}$$

where η_T is determined by the power amplifier efficiency and η_R is mostly determined by the

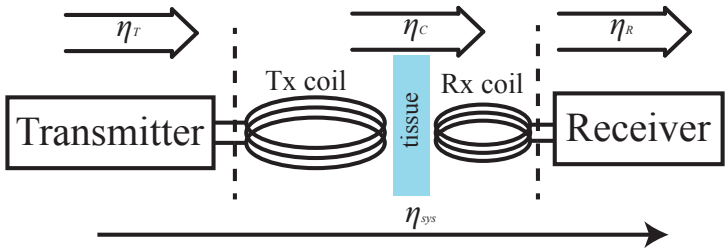

Figure 2.3: Power transfer efficiency for whole IMD system

on-chip rectifier conversion efficiency, described in Chapter 5. To simplify the estimation of

the overall efficiency of the link, the circuits on the side of the receiver coil starting with the conversion rectifier are modeled as an complex passive load Z_L reducing the total efficiency to:

$$\eta_{sys} = \eta_T \eta_C. \tag{2.9}$$

In our design our attention will be focused on the efficiency η_C. We will investigate how shape and geometry of the coils as well as the reading distance between the coils affect the η_C and design the optimal WPT link for deeply implanted miniature size medical devices. In the following analysis, we will asume that the distance between coils is 5 cm and the size of the receiver coil is limited to 3mm $\times$ 3mm.

Before analysis of of the optimum frequency for coils of different sizes and separating distances, a brief introduction of commonly used matching techniques used to maximize the coil power transfer efficiency will be described first.

Resonant matching

The first classic inductive coupling matching technique, under the RLC lumped model of the coils, is resonant matching. Commonly, the series resonant capacitor is applied on the transmitter side to maximize the driving current in Tx coil, while parallel resonant capacitance is used on the receiver side to maximize the induced voltage on the equivalent load. The maximum power transfer efficiency in this case is [12] :

$$\eta_{c,res} = \frac{k^2 Q_T Q_R}{\left[1 + (1 + k^2 Q_T Q_R)^{1/2}\right]^2} \tag{2.10}$$

when equivalent load R_L is equal to:

$$R_{L,opt} = \frac{Q_R^2 R_{s2}}{\sqrt{1 + k^2 Q_T Q_R}} \tag{2.11}$$

where Q_T and Q_R represent quality factors for transmitter coil and receiver coil respectively, R_{s2} is the parasitic resistor in R-L model of the receiver coil, while k is the coupling coefficient between the two coils. Resonant matching often comes with quasi-static analysis, and is very classic and popular for low frequency wireless link design.

Simultaneously conjugate matching

Resonant matching technique works quite well for WPT where tissue effect on WPT link can be negligible. However, the simultaneously conjugate matching, expressed in terms of the S-parameters, would be more suitable for general passive, linear and unconditionally stable network [24]. Conjugate matching of both source and load to the network guarantees the maximum power available from the source [32]. Then for general two-port network, the maximum coil power transfer efficiency, or transducer power gain as noted in [32], defined as the ratio of the power received at the load to power available from the source, can be expressed as

$$\eta_{c,conj} = G_T = K - \sqrt{K^2 - 1}, \tag{2.12}$$

where

$$K = \frac{1 - |S_{11}|^2 - |S_{22}|^2 + |\Delta|^2}{2\,|S_{12}^2|}, \tag{2.13}$$

and

$$|\Delta| = \left| S_{11} S_{22} - S_{12}^2 \right|. \tag{2.14}$$

The expression for the efficiency is valid when the network is unconditionally stable. The stability condition can be expressed as $K > 1$ and $\Delta < 1$.

Maximum efficiency matching technique

Simultaneous conjugate matching ensures the maximum power from the source, but the whole system efficiency η_{sys} is bound at 50% since conjugate matching on the source terminal makes only half the power generated by the source delivered to the rest of the circuit [32]. The achievable maximum WPT efficiency for the whole power transfer system under the optimal load value can be expressed in terms of Z-parameters modeling the link [27]. The maximum transfer efficiency is given by

$$\eta_{sys} = \eta_T \eta_C = \eta_T \times \frac{\chi}{\left(1 + \sqrt{1+\chi}\right)^2} \tag{2.15}$$

where

$$\chi = \frac{|Z_{12}|^2}{\mathrm{re}(Z_{11})\mathrm{re}(Z_{22}) - \mathrm{re}^2(Z_{12})}. \tag{2.16}$$

The optimum value of load Z_{Lopt} is given by the following equations:

$$\mathrm{re}(Z_{Lopt}) = \frac{\sqrt{\left[\mathrm{re}(Z_{11})\mathrm{re}(Z_{22}) + \mathrm{im}^2(Z_{12})\right]\left[\mathrm{re}(Z_{11})\mathrm{re}(Z_{22}) - \mathrm{re}^2(Z_{12})\right]}}{\mathrm{re}(Z_{11})} \tag{2.17a}$$

$$\mathrm{im}(Z_{Lopt}) = \frac{\mathrm{im}(Z_{12})\mathrm{re}(Z_{12})}{\mathrm{re}(Z_{11})} - \mathrm{im}(Z_{22}.) \tag{2.17b}$$

Power amplifier used at the transmitter side, which determins η_T, can achieve high power efficiency (theoretically 100% for ideal device) when using transistor as a switch. The maximum power transfer efficiency (2.15) is the same as the optimum power efficiency under resonant matching when only purely inductive coupling exists between the coils; and is the

same to the efficiency derived for the simultaneous conjugate matching when the impedance of the whole network is matched to the source resistor [27].

All these three matching techniques require matching networks for transformation of the load impedance to achieve the optimum efficiency, with a slight power efficiency loss. We also found that these three matching techniques lead to similar solutions in the links we investigated, since the optimum load value is primarily determined by the properties of the receiver coil due to the extremely loose coupling condition in the WPT system.

2.3.2 Safety Issues Regarding EM field Exposure

How to protect human beings against the adverse health effects of exposure to EM field is a very important topic. By now, established biological effects of the EM exposure mainly come from internal electric field inside the body, and no adverse health effects directly related to magnetic fields have been reported so far [33]. For low frequencies, the effect appears as the electrostimulation on muscles and nerves caused by electric current or field; while for higher frequencies, heating of tissue caused by internal electric field become predominant and electrostimulation effort diminishes [34, 35]. Thermal effect on the tissue is expressed in the term of specific absorption rate (SAR), which describe the EM power absorption rate by biological tissue. Generally SAR, unit of which is watts per kilogram, can be expressed by physical properties of the tissue and the internal electric field:

$$SAR = \frac{\sigma \left|\mathbf{E}\right|^2}{\rho} \tag{2.18}$$

where σ and ρ represent conductivity and mass density of the exposed tissue, E is electric field strength in the tissue.

Based on existing studies on interaction between EM field and biological tissue, many sci-

entific committees, like the International Commission on Non-Ionizing Radiation Protection (ICNIRP), the Standards Coordinating Committee of IEEE and etc. have published safety guidelines limiting the strength of EM field. Those guidelines define basic restrictions(BRs) on current density or electric field strength for frequencies below 10MHz (5MHz for IEEE standards), and thermal absorption rate SAR for frequencies above 100kHz; for frequencies in transition region, both standards need to be considered. As we will discuss later, our system is expected to operate at frequencies above 10MHz, and we will just consider using SAR as the safety standard throughout this work. ICNIRP guidelines [36], the reference the European Union uses as to set the regulator, and IEEE guidelines issued in 2005 [37], set averaged SAR limits for general public under localized exposure 4 W/kg over 10 g tissue of extremities and pinnae, 2 W/kg over 10 g of any other tissue. In the United States, Federal Communications Commission (FCC) built a national exposure regulations from the guidelines issued by the National Council on Radiation Protection (NCRP) in 1986 [38] and ANSI/IEEE in 1992 [39]; and FCC guidelines restrict localized exposure SAR for general public at 4 W/kg over 1 g tissue for extremities and 1.6 W/kg over 1 g tissue for other parts of body.

Besides the BRs, maximum permissible exposure values(MPEs) derived from the BRs as restrictions over external fields are also provided by these guidelines or standard, due to the difficulty and impractical of measuring directly within biology tissue the internal field, on which BRs place the limit. However, though MPEs on external incident fields is much easier to evaluate and control, Christ et al. [35] point out that because of the special types of EM fields generated by wireless power transfer system, which is strong magnetic near fields, fully application of satisfying MPEs results in the results far below the safety standards, and evaluation of safety situation should be based on the BRs. In this work, we will utilize computational full-wave analysis to evaluate the exposure under this situation; and SAR

limit set by the FCC, which is to 1.6W/kg averaged over 1 g of tissue is applied in this work unless noted otherwise.

2.3.3 Discussion on maximum receiving power

In the previous chapter, we discussed the design procedures for the WPT link based on the optimization of the power transmission efficiency. To obtain the optimum efficiency, impedance transformation is required to change the terminal impedance to the optimum value. In the design of the practical systems, as the one presented in the introduction with the two phase operation, the equivalent DC impedance of the storage capacitor seen at the load terminals keeps changing during the procedure of charging, which means that the transformed impedance meets the requirement of the optimum impedance only during short period of time. That means that WPT network can't always keep at the optimum transmission efficiency during the charging procedure if we use matching technique to achieve high efficiency transmission. Also high efficiency cannot guarantee high voltage at tag terminal. Even though impedance transform technique can also be utilized here to acquire high voltage with reactive components, practically due to the non-idealistic of these components, the transform network may also consume some power and thus decrease the overall not-so-high power efficiency.

Although the transmission efficiency is important parameter in the design of the wireless link, it does not guarantee that the maximum possible power is delivered to the implant or that we can achieve the highest possible voltage at the load terminals, which is important for certain applications. In this chapter, we will target directly the maximum achievable power at the implant and the highest possible voltage at the receiver terminals as the design goals. To optimize the terminal voltage of Rx coil, we can start from a closed-form formula

for induced coil voltage at coil terminal in terms of geometry of the coil as well as the change rate of H-field that the coil is exposed to. The induced voltage generated at the terminal of Rx antenna given by [40]:

$$V_{Rx,in} = \mu_0 A_{\mathtt{Rx}} N_{\mathtt{Rx}} \omega H_{eff} \tag{2.19}$$

where A_{Rx} and N_{Rx} are the area and turn number of Rx coil respectively. This equation may not be quite precise for specific cases, but it will give us a heuristic qualitative inspiration about what need to be optimized. Since the implant coil under study here is fixed at 3mm $\times$ 3mm, not much improvement can be done with modifications of the Rx coil, and more optimization freedom will be left on the field improvement on the side of the external Tx coil.

Though the previous simulation results show that the optimum frequency for 10cm $\times$ 10cm Tx coil is at 10MHz, we will consider higher frequency in our design. One reason is that, according to eq.(2.19), higher frequencies will lead to the higher open voltage at coil terminal; also by applying frequency higher than 10MHz, we avoid placing WPT link design under another restriction of in body current density for preventing DC electrostimulation. But from the other perspective, EM field at higher frequencies tend to generate higher E-field than EM field at lower frequencies, which may limit the transmission power in Tx coil, and possibly the available power to the implant [41]. Considering all these trade-offs and also the limits rendered by the Industrial Scientific Medical (ISM) band, we used 40.68 MHz as the operating frequency in the design of the system in the following analysis, and we will optimize *in vivo* H-field at this frequency.

2.3.4 Misalignment situation

In the study of power inductive link, assuming transmitting coil and receiving coil is perfectly aligned is a very commonly used hypothesis to simplify analysis. But in the real world, for most of the time, there often exist certain kinds of misalignments between the two coils, including rotational misalignment when the angle between the two coil axes is not zero, positional misalignment when the center of receiving coil is moving away from the axis of the transmitting coil, or the combination of both as shown in Fig. 2.4. This leads to the attenuation of power efficiency and receiving power. In the worst scenario when receiving coil axis is perpendicular to the magnetic field vector, the two coils are decoupled from each. Thus, the misalignment situation is an important factor in the design of wireless link and this applies to low frequency links with frequency range from 10 MHz to 100 MHz.

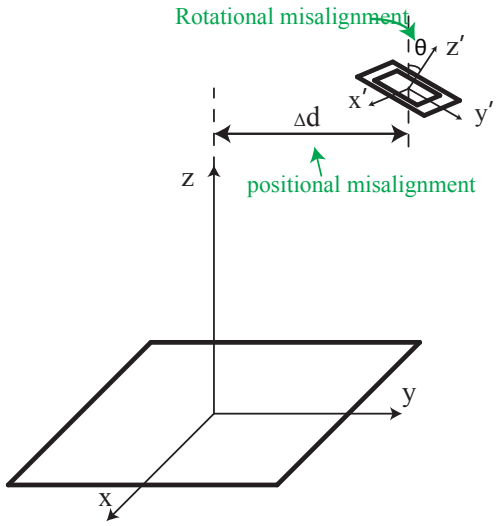

Figure 2.4: Misalignment between the two coils

2.4 Lumped model of the printed spiral coil and field calculation

When we apply quasi-static analysis and resonant matching technique at low frequencies, no extensive numerical simulation is required to extract the lumped-element circuit model. The model characteristics can be expressed using few closed-form equations [20]. This section will give a brief description of commonly used closed-form equations for coil model characteristics extraction, and introduce a computational method based on finite sets of analytical expressions for inductive link calculation for general cases. We are going to apply these method on link analysis on Chapter **??**.

2.4.1 Closed-form equations for printed spiral coil

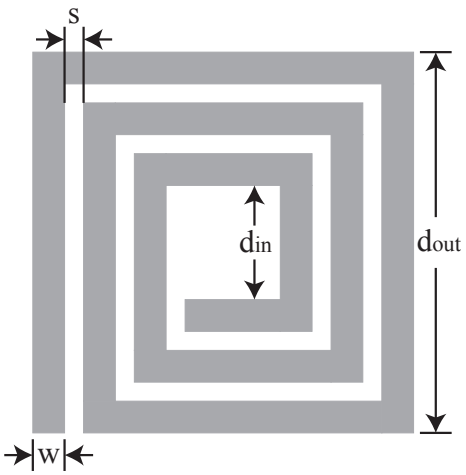

Figure 2.5: Printed spiral coil

The design of the printed square spiral coil is illustrated in Fig. 2.5. The main geometrical parameters of a square coil are its outer side length d_{out}, turn number n, wire width w and the spacing between adjacent wires s. The inductance of the square coil can be estimated

as [30]

$$L \approx \frac{1.27\mu_0 n^2 d_{avg}}{2}\left[\ln\left(\frac{2.07}{\chi}\right) + 0.18\chi + 0.13\chi^2\right], \tag{2.20}$$

where d_{avg} is the arithmetic mean of the outer side d_{out} and inner side d_{in}, χ is the fill factor given by

$$\chi = \frac{d_{out} - d_{in}}{d_{out} + d_{in}}. \tag{2.21}$$

Then parasitic capacitance of the coil is calculated using the following semi-empirical design formula [20]

$$C_p \approx (\alpha\epsilon_{r,coat} + \beta\epsilon_{r,sub})\,\epsilon_0 \frac{t_w}{s} l_s, \tag{2.22}$$

where $\epsilon_{r,coat}$ and $\epsilon_{r,sub}$ are the relative permittivity of coating and substrate respectively, values of each are 1 and 4.4 for air and FR4 in our case; α and β are corresponding empirical constants equal to 0.9 and 0.1. t_w represent thickness of wire, which is $38\mu m$ for 1oz copper, l_s is the length of the wire spacing and can be calculated as

$$l_s = 4\,(n-1)\,(d_{out} - nw) - 4ns\,(n+1)\,. \tag{2.23}$$

To calculate the coil's AC parasitic resistance, the DC resistance should be calculated first. Knowing the resistivity of the coil wire ρ_w, we obtain the DC resistance of the coil

$$R_{dc} = \rho_w \frac{l_w}{w t_w}, \tag{2.24}$$

where l_w represent the total length of the conductor expressed as

$$l_w = 4nd_{out} - 4nw - (2n+1)^2\,(s+w)\,. \tag{2.25}$$

When alternating current flows in the conductor wire, the current density distribution concentrates near the surface of the conductor, resulting in increase of the wire AC resistance. The skin depth of a conductor operating under frequency f is

$$\delta = \sqrt{\frac{\rho_w}{\pi \mu_{r,w} \mu_0 f}}, \tag{2.26}$$

and the AC resistance is calculated as

$$R_s = R_{dc} \frac{t_w}{\delta \left(1 - e^{-t_w/\delta}\right)}. \tag{2.27}$$

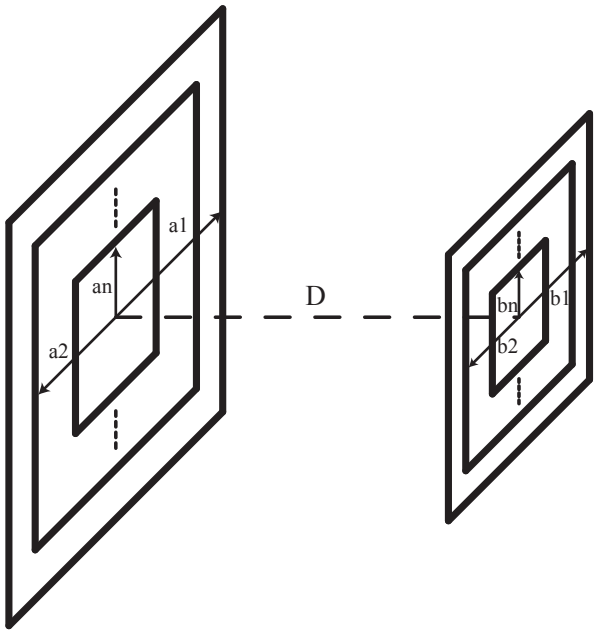

Figure 2.6: Illustration of the geometric approximation for perfectly aligned square spiral coils

Next is to calculate the mutual inductance between two coils. To simplify the problem, we assume that the axes of the two coils under study are perfectly aligned. To calculate the

mutual inductance between two perfectly aligned square spiral coils, we first approximate each coil as a combination of N concentric rectangular loops with descending sides, as shown in Fig. 2.6; radius of each loop is denoted by a_i or b_j. Mutual inductance of two loops in each coil can be calculated by a closed-form formula [42]

$$M_{ij} = \frac{2.2\mu}{\kappa}\sqrt{a_i b_j}\left[\left(1-\frac{\kappa^2}{2}\right)K(\kappa) - E(\kappa)\right] \tag{2.28}$$

$$\kappa = 2\sqrt{\frac{a_i b_j}{(a_i+b_j)^2 + D^2}}, \tag{2.29}$$

where D is the distance between the coils, $K(\kappa)$ and $E(\kappa)$ are the complete elliptic integrals of the first and second kind. Then the total mutual inductance between the two coil is the summation of all the mutual inductance between each small loop pair:

$$M_{tot} = \sum\sum M_{ij}(a_i, b_j). \tag{2.30}$$

2.4.2 Computational method with analytical expressions

[20] does provide very specific closed-form equations for RLC coil, however, these equations - especially formulas for self-inductance and mutual-inductance calculation - are only suitable for cases with square coils and when the coils are strictly aligned with each other, which most of the real world cases may not satisfy. More specific analytical methods are needed to handle more general cases like inductance of coil shape other than square and link analysis between coils with relative lateral offset position or angular rotation as stated in 2.3.4. Thus calculation method based on partial inductances, which analyze the total system inductance based on that of each conductor segment, is more suitable here. The concept of partial inductance theory was first brought up and developed by Rosa in 1908 [43], and

further illustrated comprehensively by Grover in his book[44] which was first published in 1946. But no specific mathematical analysis was given yet. Ground on this theory, Greenhouse presents sets of analytical equations to calculate the inductance of planar rectangular inductor [45]. In 1972, Ruehli applied this method to parasitic inductance calculation in general microcircuit modeling and provide specific mathematical analysis in [46]. Here the derivative and analytical formulas are based on the material aforementioned.

The partial inductance theory

To start with, we assume that the circuits in the system are closed filament loop. The inductance between circuit i, j can be represented as the magnetic flux $\Phi_{f_{ij}}$ generated by current I_{f_j} in loop j divided by current I_{f_j}; and Φ_{ij} is the integrals of magnetic flux density $\mathbf{B}_{f_j}$ over the vector surface defined by loop i:

$$M_{f_{ij}} = \frac{\Phi_{f_{ij}}}{I_{f_j}} = \frac{\int \mathbf{B}_{f_j} \cdot d\mathbf{S}_{f_i}}{I_{f_j}}, \tag{2.31}$$

where the letter f on the subscript indicate filament circuit. By applying the equation $\mathbf{B} = \nabla \times \mathbf{A}$, $\Phi_{f_{ij}}$ can be expressed by the magnetic vector potential $\mathbf{A}$ and further developed using Stokes' theorem as:

$$\Phi_{f_{ij}} = \int \left(\nabla \times \mathbf{A}_{f_j}\right) \cdot d\mathbf{S}_{f_i} = \oint \mathbf{A}_{f_j} \cdot d\mathbf{l}_{f_i}, \tag{2.32}$$

where $\mathbf{A}_{f_j}$ generated by current I_{f_j} in filament loop j is

$$\mathbf{A}_{f_j} = \frac{\mu}{4\pi} \oint \frac{I_{f_j} d\mathbf{l}_{f_j}}{r_{f_{ij}}} = \frac{\mu I_{f_j}}{4\pi} \oint \frac{d\mathbf{l}_{f_j}}{r_{f_{ij}}}, \tag{2.33}$$

where $I_{f_j} d\mathbf{l}_{f_j}$ is the differential current element in loop j and $r_{f_{ij}}$ is the corresponding distance between the element and observation point. Then the inductance $L_{f_{ij}}$ between two filament coils is expressed in term of $\mathbf{A}_{f_j}$ as

$$M_{f_{ij}} = \frac{\mu}{4\pi} \oint \oint \frac{d\mathbf{l}_{f_j} \cdot d\mathbf{l}_{f_i}}{r_{f_{ij}}}. \tag{2.34}$$

When considering the real coil loop, it can be viewed as composed of bunch of filament coil;

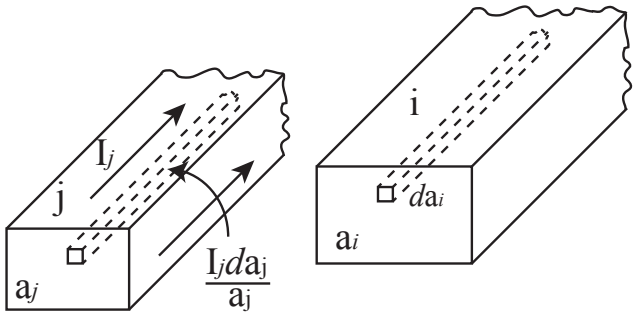

Figure 2.7: Filament conductor can be seen as differential element in real conductor

then as shown in Fig. 2.7 I_{f_j} is the differential current in the conductor expressed by total current in conductor I_j and cross section perpendicular to the current flow a_j:

$$I_{f_j} = \frac{I_j da_j}{a_j}. \tag{2.35}$$

After integration over the area a_j, the magnetic vector potential A_j generated by the total current in the whole coil is:

$$\mathbf{A}_j = \frac{\mu I_j}{4\pi a_j} \int \oint \frac{d\mathbf{l}_{f_j} da_j}{r_{f_{ij}}}. \tag{2.36}$$

Similarly, the magnetic in circuit i is the magnetic flux Φ_{ij} averaging over the filaments:

$$\Phi_{ij} = \frac{1}{a_i} \int \oint \mathbf{A}_{f_j} \cdot d\mathbf{l}_{f_i} da_i. \tag{2.37}$$

Then the inductance between two real circuits is:

$$M_{ij} = \frac{1}{a_i a_j} \frac{\mu}{4\pi} \int \oint \int \oint \frac{d\mathbf{l}_{f_j} \cdot d\mathbf{l}_{f_i} da_j da_i}{r_{f_{ij}}}, \tag{2.38}$$

which can also be represented by filament inductance $L_{f_{ij}}$ in Eq. (2.34):

$$M_{ij} = \frac{1}{a_i a_j} \int \int L_{f_{ij}} da_j da_i. \tag{2.39}$$

The above derivative of inductance is for closed-loop circuit since the magnetic flux is induced in a close-loop circuit. However, the formation of Eq. (2.38) suggests rewriting of the integrations over the loops as the summations over divided straight segments and each segment is allowed to have its own cross section a_k and length l_{p_k}, where k indicates the segment number of the divided part. And Eq. (2.38) is rewritten as:

$$M_{ij} = \sum_{m=1}^{M} \sum_{n=1}^{N} \frac{1}{a_m a_n} \frac{\mu}{4\pi} \int \int \int_{b_m}^{e_m} \int_{b_n}^{e_n} \frac{d\mathbf{l}_{f_n} \cdot d\mathbf{l}_{f_m} da_n da_m}{r_{f_{mn}}}, \tag{2.40}$$

where M is the divided segments number of loop i, N is the divided segments number of loop j, b_m, b_n and e_m, e_n indicate the corresponding beginning and ending points for the segments. Then partial inductances are defined as the arguments in the summation as:

$$M_{p_{ij}} = \frac{1}{a_m a_n} \frac{\mu}{4\pi} \int \int \int_{b_m}^{e_m} \int_{b_n}^{e_n} \frac{d\mathbf{l}_{f_n} \cdot d\mathbf{l}_{f_m} da_n da_m}{r_{f_{mn}}}; \tag{2.41}$$

and the total inductance can be written in terms of partial inductance as

$$M_{ij} = \sum_{m=1}^{M} \sum_{n=1}^{N} M_{p_{ij}}. \tag{2.42}$$

Then the inductance of open and quasi-closed loop can be obtained in accordance with the concept of partial inductance, that the inductance is the summation of the partial inductance between each segment pair. Eq. (2.42) can also be used to calculate the self-inductance of loop and open-loop circuit, and the result fits the formula given in [45] that the total inductance of a coil or a open loop circuit is the sum of self-inductance over all the segments plus the mutual inductance between them. To differentiate, we will use L to represent the self-inductance of the segment or coil, M to represent the mutual inductance in the following part.

The analytical equations for self-inductance and mutual inductance will be given in the next section. The sign of $M_{p_{ij}}$ is determined by the sign of the scalar product between differential vector $d\mathbf{l}_{f_n} \cdot d\mathbf{l}_{f_m}$, the direction of which are determined by current flow direction in them. For the special case of orthogonal currents, the value of $M_{p_{ij}}$ is zero.

Partial inductance formula

The following formulas given in this section is based on the collections of answers given in [44] and [45]. The self-inductance for a conductor with l length, and rectangular cross section can be expressed by:

$$L_l = \frac{\mu l}{2\pi} \left[\ln\left(\frac{2l}{w+t}\right) + 0.50049 + \frac{w+t}{3l} \right] \tag{2.43}$$

where w and t represent conductor width and thickness correspondingly, and $w >> t$. For mutual inductance calculation between two parallel conductor can be facilitated by filament approximations. It's very convenient to calculate the basic mutual inductance between two identical filaments with only prallel distance, as shown in, by equation:

$$M_l = \frac{\mu l}{2\pi}\left[\ln\left(\frac{l}{d}+\sqrt{1+(\frac{l}{d})^2}\right)-\sqrt{1+(\frac{d}{l})^2}+\frac{d}{l}\right], \tag{2.44}$$

where l is the length of the filaments and d is the distance between them.

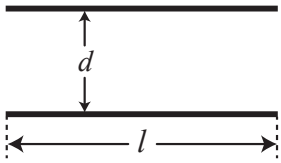

Figure 2.8: Mutual inductance between two parallel filaments

When the size of the cross section of the conductors is much smaller than the distance between them, the conductors can be represented by the filaments locate at the center of their axes. When the cross section of traces is too large to simplify the conductors to filaments, *geometric mean distance* (GMD) approximation can be used for calculations, which is using the formula for the GMD provided by [44] and [45] to represent the conductor distance:

$$GMD = \frac{d_C}{\exp\left[\frac{1}{12}\left(\frac{d_C}{w}\right)^2+\frac{1}{60}\left(\frac{d_C}{w}\right)^4+\frac{1}{68}\left(\frac{d_C}{w}\right)^6+\frac{1}{360}\left(\frac{d_C}{w}\right)^8+\frac{1}{660}\left(\frac{d_C}{w}\right)^{10}.....\right]}, \tag{2.45}$$

where d_C is the distance between the center of the two conductors, w is the conductor width. Replacing d in Eq. (2.44) with GMD, we can get the mutual inductance between two identical parallel conductors of general cases.

Starting from this, mutual inductance for different cases of parallel conductors will be

given as following in term of M_l, the subscript of which will denote the various conductor size and their combination as will be demonstrated in corresponding figures. Here some common cases of conductors and their mutual inductance, which will be use in Ch. **??** will be shown and given as below. For the convenience, GMD will also been used in the following formulas to represent the parallel distance between two conductors.

- Offset parallel filaments in different straight line

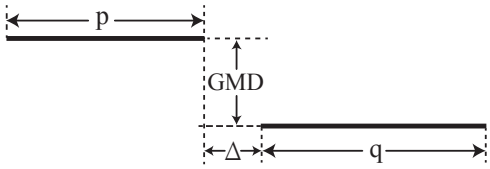

Figure 2.9: Offset parallel filaments on different straight line

$$M = \frac{1}{2}\left(M_{p+q+\Delta} + M_{\Delta}\right) - \frac{1}{2}\left(M_{p+\Delta} + M_{q+\Delta}\right) \tag{2.46}$$

- Overlapping parallel filaments in different straight line

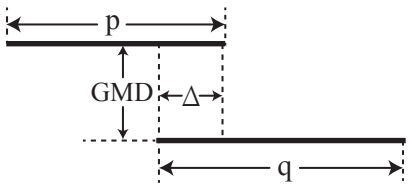

Figure 2.10: Overlapping parallel filaments on different straight line

$$M = \frac{1}{2}\left(M_{p+q-\Delta} + M_{\Delta}\right) - \frac{1}{2}\left(M_{p-\Delta} + M_{q-\Delta}\right) \tag{2.47}$$

- Complete overlapping of parallel filaments in different straight line

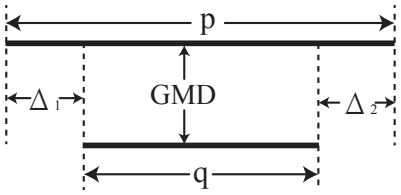

Figure 2.11: Complete overlapping parallel filaments on different straight line

$$M = \frac{1}{2}\left(M_{q+\Delta_1} + M_{q+\Delta_2}\right) - \frac{1}{2}\left(M_p + M_q\right) \tag{2.48}$$

- Common-ended parallel filaments at the same side in different straight line

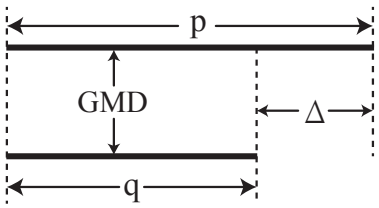

Figure 2.12: Common-ended parallel filaments at the same side on different straight line

$$M = \frac{1}{2}\left(M_p + M_q\right) - \frac{1}{2}M_\Delta \tag{2.49}$$

- Common-ended parallel filaments at the opposite side in different straight line

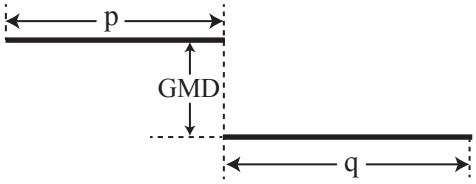

Figure 2.13: Common-ended parallel filaments at the opposite side on different straight line

$$M = \frac{1}{2}M_{p+q} - \frac{1}{2}\left(M_p + M_q\right) \tag{2.50}$$

- Offset parallel filaments in the same line

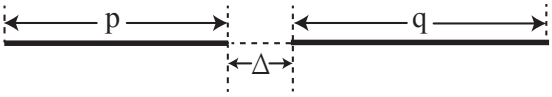

Figure 2.14: Offset parallel filaments in the same line

$$M = \frac{\mu l}{4\pi}\big[(p+q+\Delta)\ln(p+q+\Delta) - (p+\Delta)\ln(p+\Delta) \\ - (q+\Delta)\ln(q+\Delta) + \Delta\ln\Delta\big], \tag{2.51}$$

For the special case when the ends of the conductors connect together, the mutual inductance is calculated by:

$$M = \frac{\mu l}{4\pi}\left[p\ln\left(\frac{p+q}{p}\right) - q\ln\left(\frac{p+q}{q}\right)\right], \tag{2.52}$$

2.4.3 Magnetic Field Generated by the Printed Spiral Coil

We can calculate the magnetic field generated by the single turn rectangular coil with size $a \times b$ along its axis as [47]

$$H = \frac{I_{Tx}ab}{4\pi\sqrt{\left(\frac{a}{2}\right)^2 + \left(\frac{b}{2}\right)^2 + D^2}}\left[\frac{1}{\left(\frac{a}{2}\right)^2 + D^2} + \frac{1}{\left(\frac{b}{2}\right)^2 + D^2}\right], \tag{2.53}$$

where D denotes the distance away from the coil. For the special case of the rectangular coil - square coil with side length a, the formula is simplified to

$$H = \frac{I_{Tx}a^2}{2\pi\sqrt{\frac{a^2}{2} + D^2}\left(\frac{a^2}{4} + D^2\right)}. \tag{2.54}$$

Fig. 2.15 plots the magnetic field along coil axis for square coils of different sizes under same driving current. It shows that the small-size coil has very steep magnetic field plot, with the high field value in the vicinity of the coil and low field after an abrupt drop; while the large-size coil tends to generate much smoother shape of the field plot, with the magnetic field not very high near the coil, but not very low at the increase distance from the coil, even much higher than the counterpart small coil. Thus there must be a optimum size of antenna to achieve maximum magnetic field for a given distance. At the specific distance the magnetic field will be maximized with a coil size

$$a = 2.54D \tag{2.55}$$

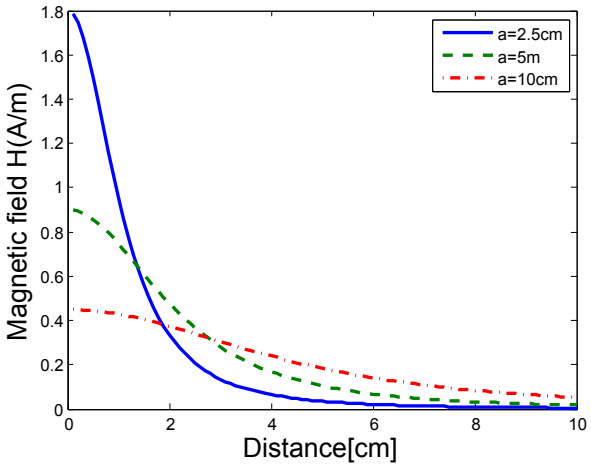

Figure 2.15: Magnetic field along the axis of a printed spiral coil.

For n-turn square spiral coil, the antenna can be approximated as a group of concentric loops of different sizes. Since it is too complicated and not very necessary to solve derivative of summation of (2.54), (2.55) can be used as a rule of thumb.

2.5 Wireless inductive link design with quasi-static analysis

2.5.1 Model Verification with Demo Coil

Based on the equation (2.10), we can conclude that to obtain high η_c, a high k and high Q of the antennas are needed. Based on the closed-form formulas aforementioned, two PCB square coils with the large number of turns were designed and fabricated. Though their geometries are only suitable for low-frequency operation - as increasing proximity effect may downgrade the quality factor of antennas at high frequencies - they can still be used to verify our calculation and simulation results.

Measurement of the coupling coefficient k

S-parameters of a two-port network composing two coils can be directly measured using VNA. But in order to get the power efficiency through equation (2.10), we have to transfer the S-parameters to the variables used in the analysis of the inductive link, quality factor of each coil and coupling coefficient k. The quality factor of the coil can be approximated by using the fraction of the image part of the coil's Z-parameter, which can be easily converted from S-parameter by VNA itself, over the real part. To measure accurately the weak coupling coefficient k between two coils, we designed a matching networks between the VNA and the coil pair. Without the matching networks,the large power reflection is possible. The k can also be expressed in terms of Z-parameters.

Fig. 2.16 shows the equivalent circuit for the measurement setup, parts in the dotted square boxes denote the matching circuits which ensure that the impedances of the two coils are transformed to 50 Ω, the port impedance of the VNA.

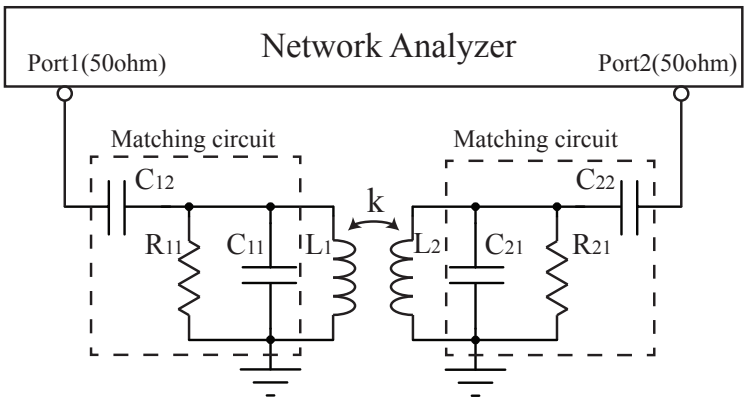

Figure 2.16: Equivalent circuit for measurement setup of k

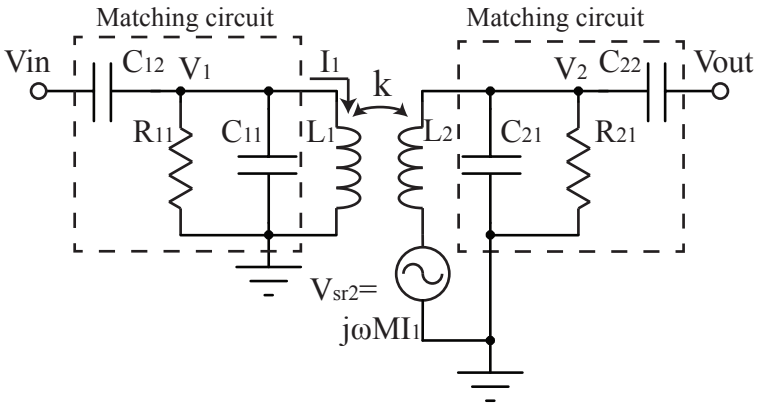

Figure 2.17: Illustrate relation between S-parameter and k

To make derivation reasonable simple, we assume that $k << 1$, which means that the mutual inductance effect on L_1 can be negligible as well as the reflective impedance. Since the reader coil 1 is matched to the characteristic impedance of port1 (R_1=R_{port}=50 Ω), no reflection happens at port 1, and all the incident power at port1 is delivered to the following circuit, leading to $P_{in} = P_{R_{11}}$, expressed it in terms of voltages:

$$\frac{V_{in}^2}{2R_1} = \frac{V_1^2}{2} R_{11}. \tag{2.56}$$

Then the voltage and current on the Tx coil will be

$$V_1 = V_{in}\sqrt{\frac{R_{11}}{R_1}} = V_{in}\sqrt{\frac{R_{11}}{R_{port}}}, \tag{2.57}$$

and

$$I_1 = \frac{V_1}{j\omega L_1}. \tag{2.58}$$

So I_1 in Tx coil generates induced voltage V_{sr2} at Rx coil as

$$V_{sr2} = j\omega M I_1 = j\omega k\sqrt{L_1 L_2} I_1 = kV_{in}\sqrt{\frac{R_{11}L_2}{R_{port}L_1}}. \tag{2.59}$$

By solving the right part of the circuit, we can get the output voltage at port 2:

$$V_{out} = V_{sr2}\frac{Z_c}{j\omega L_2 + Z_c}\frac{R_{port}}{R_{port} + 1/j\omega C_{22}}, \tag{2.60}$$

where Z_c is

$$Z_c = \frac{1}{1/R_{21} + j\omega C_{21} + 1/\left(R_{port} + 1/j\omega C_{22}\right)}. \tag{2.61}$$

Matching on both ports will also render the relation between S_{21} and the voltages as

$$S_{21} = \frac{V_2^-}{V_1^+} = \frac{V_{out}}{V_{in}}. \tag{2.62}$$

Substituting eq. (2.59) and (2.60) into this equation leads to the relation between S_{21} and k:

$$S_{21} = k\sqrt{\frac{R_{11}L_2}{R_{port}L_1}}\frac{Z_c}{j\omega L_2 + Z_c}\frac{R_{port}}{R_{port} + 1/j\omega C_{22}}. \tag{2.63}$$

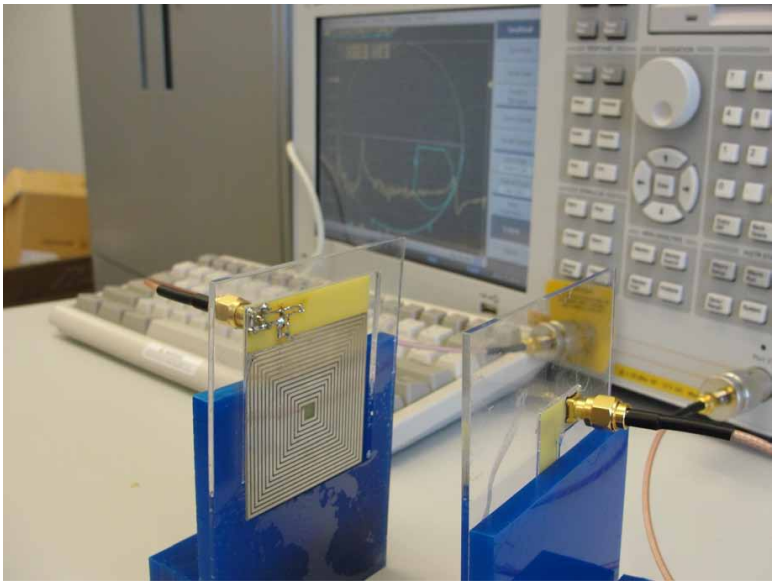

Figure 2.18: Experimental setup for measurement of the coupling coefficient k

Fig. 2.18 shows the picture of the experimental setup. We enter the k calculated from eq. (2.63) to (2.10) to get the optimum efficiency, and then compare the results with calculation and simulation results in Fig. 2.19. These plots show that the experimental results are in good agreement with the calculation and simulation results, proving the viability of the model and simulation method. We also simulated in HFSS the same coil-pair with muscle as the media between the coils and the results show that at low frequencies, the tissue effect does not have much influence on the wireless link. But due to the limitation of quasi-static

analysis method at the higher transmission frequencies and the complexity of tissue model, we will use the full-wave analysis based on Ansoft HFSS as the main research tool.

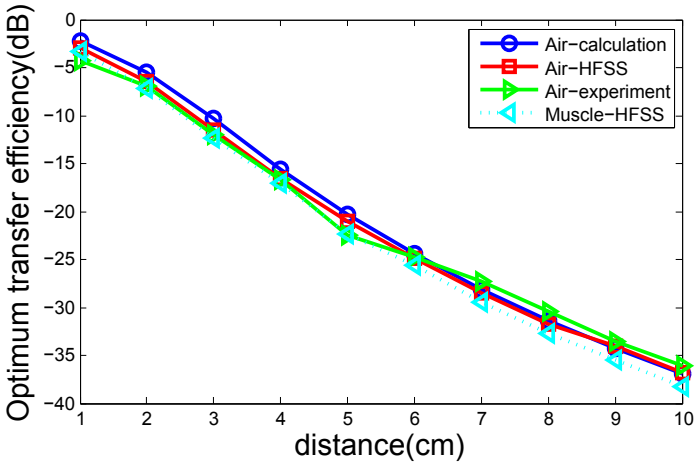

Figure 2.19: Calculated and measure transfer efficiency

2.6 Investigation on optimum frequency and Tx coil position

In chapter 1.1.1 and 1.1.2, we illustrated two application examples of deeply implanted miniature medical devices: drug intake monitoring system and deep brain implanted devices. The quasi- EM field changes rapidly in the near field region, especially when it interacts with dispersive dielectric material around, which may affect not only the field itself but also the transfer efficiency. As we stated in the introduction, for our first proposed application, the tag size is limited at 3mm $\times$ 3mm with implant depth set as 5cm. With this size constraint, we can increase the turn number in Rx coil in order to increase the open voltage at the coil terminals, but there are not many choices left due to the extreme size limit, so we will pay more attention on the parameters of the external Tx coil, including the geometry and

position of the Tx coil as shown in Fig. 2.20. We also add a medical-grade silicone layer on the surface of the coils. Silicone layer can be used as coating for implant devices and it also reduces the parasitic parameters of the coil increasing the quality factor as well as the transfer efficiency [31]. Here we fix the thickness of silicone coating at $300\mu m$. Since too many parameters are adjustable in the coil model, we will constrain our parameter space and study some typical parameters and examples in order to obtain a qualitative trend of link performance.

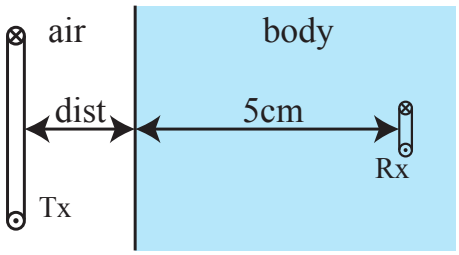

Figure 2.20: Demonstration of Tx and Rx coils' position

2.6.1 Investigation on operating frequency and coil geometries

We first want to see the influence of different WPT environments and matching techniques on the efficiencies. With the distance between coils set at 1 cm and Rx coil set to 3-turn 3 mm $\times$ 3 mm coil, 2-turn Tx coils with variant sizes are simulated when material is either muscle or air, and transmission efficiency under different matching techniques is calculated. The results are shown in Fig. 2.21. From the figure we can see that the effect of the muscle becomes pronounced for frequencies above 20MHz. Inclusion of the tissue also decreases the optimum frequency of transmission and corresponding maximum efficiency. Due to the weak coupling between the coils, the type of matching technique used doesn't affect results considerably, so unless noted otherwise, we assume that either of these three matching techniques would

lead to the similar results in the following links. Comparing the efficiencies for Tx coils of different size, size increase does decrease the optimum frequency, but the efficiencies don't improve so much because of the short distance.

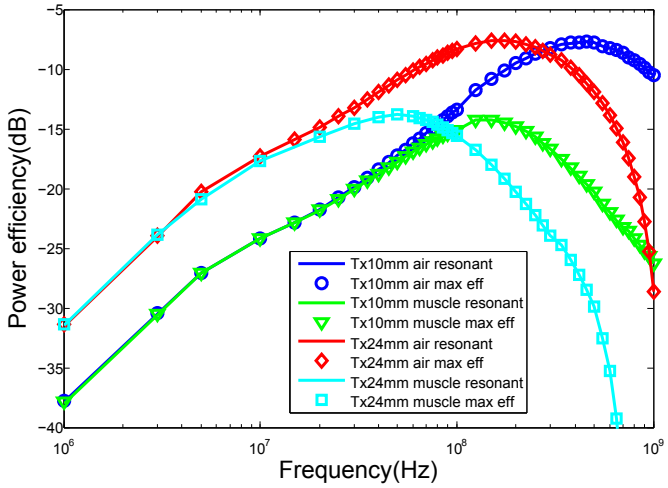

Figure 2.21: Power efficiency of the wireless link for Tx coil of different sizes in different environments when reading distance between the two coils is 1 cm.

Then we change the reading distance from 1 cm to 5 cm, increase Tx coil size from 2.4 cm to 10 cm gradually, and we also change wire width and spacing parameter as listed in table 2.1, and Rx coil turns. Fig. 2.22 focuses on how the size and parameters of Tx coil affect the efficiency, and shows that the optimum operating frequency is primarily affected by the size of coil, with little influence from the adjustment of wire parameters. If we compare the efficiencies for 24 mm Tx coil in Fig. 2.21 and Fig. 2.22, we can conclude that the increasing reading distance has a little effect on the optimum frequency but decreases significantly the transmission efficiency as expected.

It has been discussed in 2.3.2 that for RF operation below 10 MHz, RF exposure safety issue need to consider both current density and SAR. Considering this fact, operating frequency above 10 MHz is preferred to reduce design complexity and unwanted restriction.

Table 2.1: Width - space parameters

	Tx		Rx	
	width (mm)	space (mm)	width (mm)	space (mm)
parameter1	1.2	0.8	0.16	0.16
parameter2	4	2.5	0.16	0.16
parameter3	8	5	0.16	0.16
parameter4	8	5	0.3	0.16

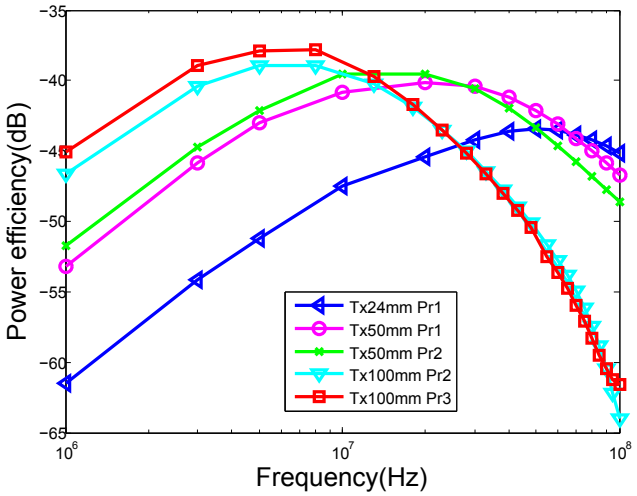

Figure 2.22: Power efficiency for 2-turn Tx coils of different size and parameters and 3-turn Rx coil when reading distance between the two coils is 5 cm.

Comparing power efficiencies for Tx coils with different sizes, it's not hard to tell that 10 cm Tx coil has maximum power efficiency among three different coil pairs. But since it locates below 10 MHz, and performance of 10 cm coil is not as good as 5 cm coil above 20 MHz, 5 cm coil has been chosen for our project and the frequencies 40 MHz and 100 MHz will be studied.

For further investigation of the optimal Tx coil parameters, we also plot the power efficiency for the 10 cm Tx coil with different number of turns in Fig. 2.24. We can see that the additional turns slightly increase the efficiency and that for the Tx coil with side length of 10 cm, the optimum frequency is around 10 MHz.

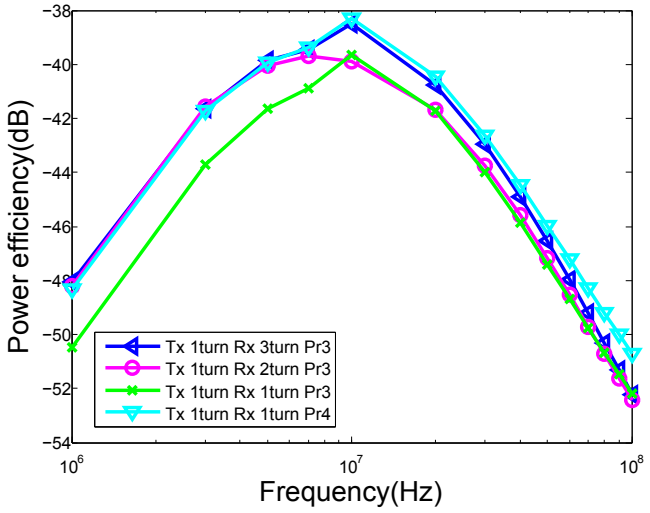

Figure 2.23: Power efficiency for Rx coils of different turn numbers and parameters in different environments when reading distance between the two coils is 5 cm and Tx coil parameters are fixed.

After that we change the number of turns for Tx coil from 2 to 1, and focus on how properties of Rx coil, including the number of turns and parameters which are listed in table 2.1, affect the efficiency. Results shown in Fig. 2.23, demonstrate that the change of Rx coil parameters, even the number of turns, doesn't affect the efficiency considerably. However, increase of turn number, and the increase of the wire width which decreases the

parasitic resistance of the coil, can improves the efficiency by 5/ 6 dB. Since achieving relatively high output voltage at Rx side is still desirable in our cases, Rx coil with higher turns is preferred.

In the next section we will discuss increasing the gap between Tx coil and tissue to decrease the SAR value, thus allowing more transmission power and possibly more available energy for receiver inside the body. Here we will simulate this setup first and see the influence of increasing gap on the efficiency. We select a practical value of 1 cm as separating gap between tissue and coil, and obtain the power efficiency as the function of transmission frequency. As Fig. 2.25 shows, the efficiency η_Cs doesn't drop so much even as the total distance is increasing; in fact, since the separation decouples the interaction between E-field and the tissue, causing the drop of real part of the coil impedance, related thermal loss decreases, and the efficiency performance is improved above 20 MHz.

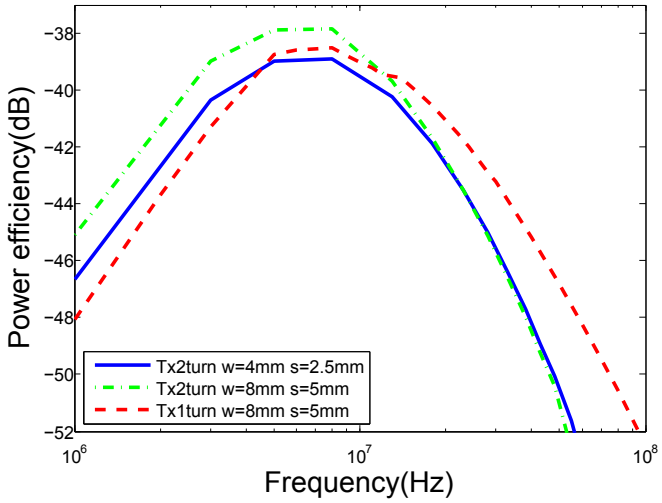

Figure 2.24: η_C when Tx coil is 1 mm away from the tissue.

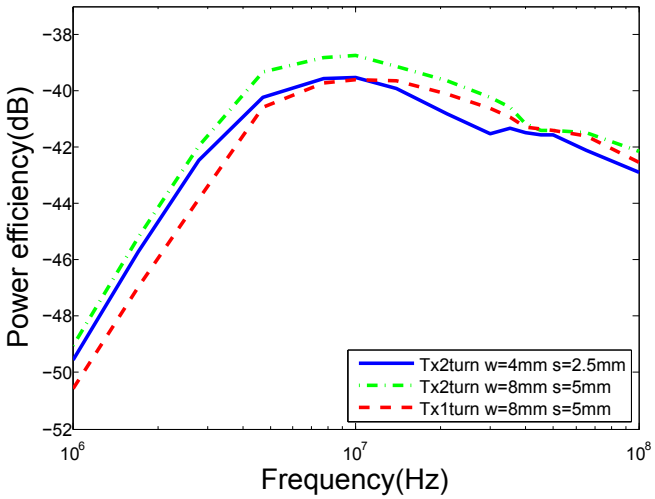

Figure 2.25: η_C when Tx coil is 1 cm away from the tissue.

2.6.2 Investigation on the optimal positioning of the Tx coil

In section 2.3.2, we discussed the safety issues related to the radiating EM field and concluded that the SAR limitation is the main restriction on the strength of EM field when human body is exposed to frequencies above 10MHz. To maximize the amount of the energy that receiver coil inside the body can gather, as much as possible energy should be delivered to Tx coil without violating the BRs set by guidelines. In other words, if we can reduce the maximum SAR generated at the surface of the skin, we can deliver more power to Tx coil and increase the H field at the receiver coil. From the definition eq. (2.18) for SAR, it means that to reduce SAR we need to decrease the E-field around the tissue.

For the electrically small coil, to which quasi-static situation applies, the feeding current of the transmitter coil can be viewed as uniformly spread along the wire and the electric field is uniformly distributed along the coil trace, leading to the uniformly distributed SAR. However, when we simulate one turn Tx square coil and evaluate the SAR pattern caused by it, we notice that there is an SAR "hot spot" around the feed point of the coil, like what

was shown in Fig. 2.24. Fig. 2.26(a) illustrates the layout of the single square coil under examination.

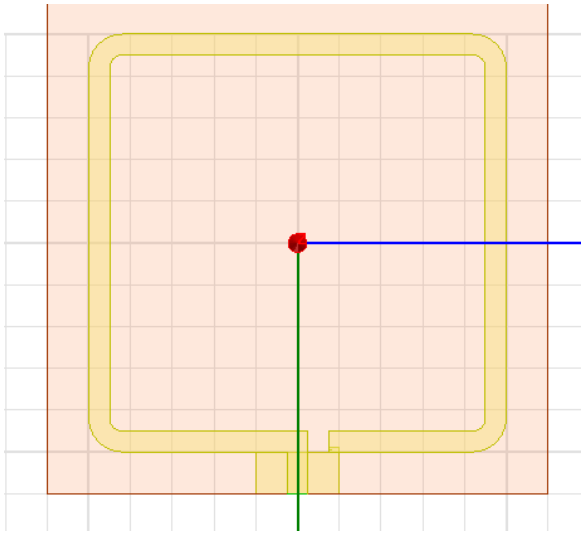

(a) Single Coil Structure

Figure 2.26: The layout of the single coil structure.

To investigate this issue, we can view the total electric field (E_{tot}) generated by the transmitter coil is the combination of conservative dielectric electric field (E_c), which is gradient of scalar electric potential (φ) of the coil, and nonconservative magnetically induced electric field (E_i) [48]:

$$E_{tot} = E_c + E_i = -\nabla\varphi - \frac{\partial A}{\partial t} \tag{2.64}$$

where A is vector magnetic potential. E_i is generated by and proportional to alternating magnetic field, which is unavoidable and uniform following the trace of the coil; E_c, the main contributor to localized intense heating ("hot spot"), is the main factor we want to reduce in order to decrease the SAR, which is suggested by the asymmetric distribution pattern of SAR.

Compare with E_i, the dielectric electric field E_c drops off dramatically in the vicinity of the coil. Thus one method to reduce SAR and maximize the available power for IMDs is

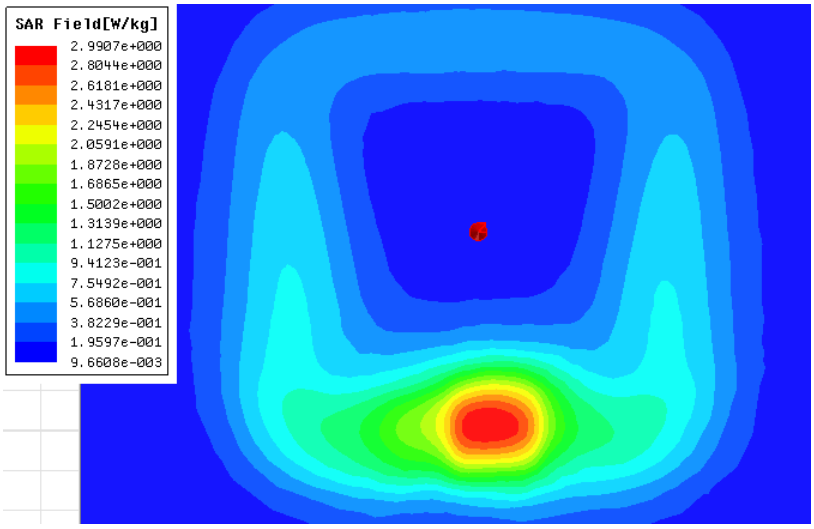

(b) SAR distribution when coil is 1mm away from tissue

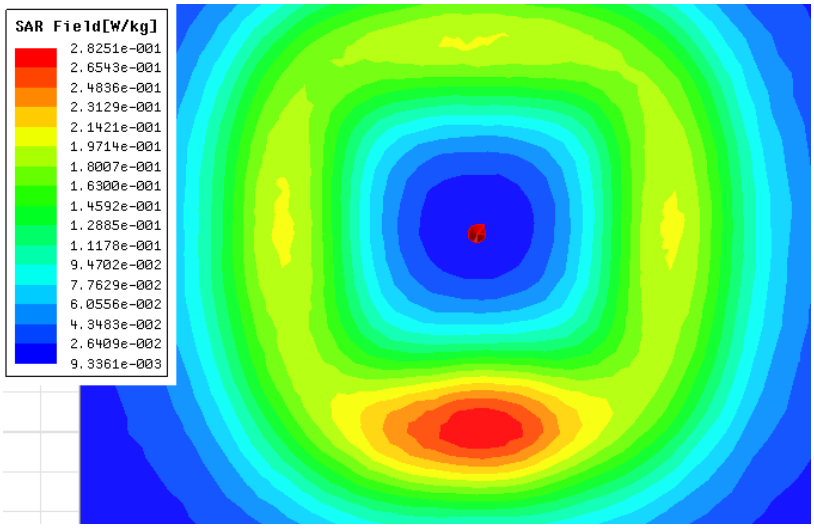

(c) SAR distribution when coil is 10mm away from tissue

Figure 2.26: SAR distributions for different separation distance at 400 mA driving current.

to move Tx coil away from the tissue. Even when the coil is moving away from the skin, the SAR value is the highest close to the feed point, although the difference to the rest of the coil trace is not that significantly higher as it's illustrated in Fig. 2.26. Fig. (b) and (c) each shows the SAR pattern when coil is 1 mm and 10 mm away from the tissue; these pictures show again how SAR drops quickly as coil moving away. Since increase of the separation between the coil and tissue allows for larger amount of power or current in Tx coil, and thus higher magnetic field for Rx coil. There should be an optimum value for the separation to achieve the highest available energy delivered to the receiver. Fig. 2.27 shows how the normalized magnetic fields - that is when maximum SAR (the SAR hot spot as explained later) equals to 1.6W/kg - at depth of 5cm change as the function of the distance between Tx coil and tissue. The figure also shows the Tx coil current needed to generate the corresponding field. It verifies our hypothesis about the relation between the normalized magnetic field and distance, with the increase in the Tx current.

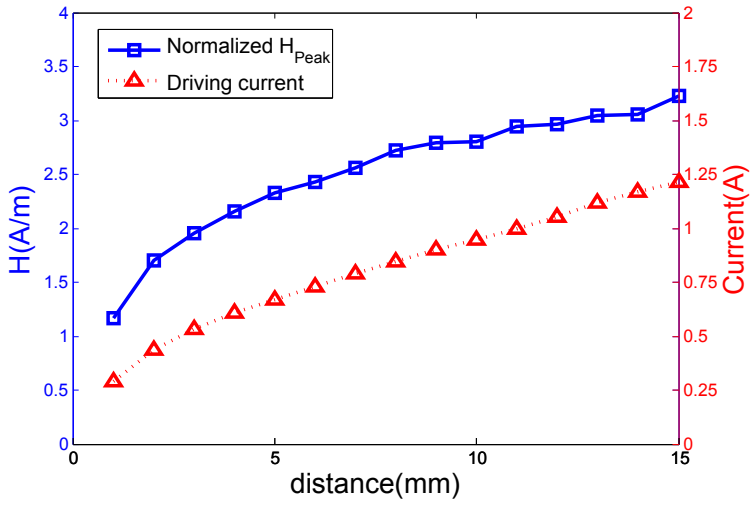

Figure 2.27: Magnetic field and current as a function of the distance between coil and tissue.

2.7 Adaptive transmitter array design

2.7.1 Comparison of SAR for single and dual transmitter coil

As previous section states, one way to decrease SAR generated by the coil is moving coil away from the body. There is another method to decrease it by modify the coil structure for transmitter. In [49], an approximate estimation of magnitude of E_c is given by

$$|E_c| \cong \frac{|V_{diff}|}{l_{gap}} = \frac{|Z_{coil}|\, I_{coil}}{l_{gap}}, \tag{2.65}$$

where I_{coil} is driving current in the coil, Z_{coil} is coil impedance, and l_{gap} is gap length. Even this equation is not very precise, and also when frequency goes high, EM near field comes more complicated to estimate, it still provides a qualitative idea which factor will affect the magnitude of E_c. So this case, either reducing I_{coil} and Z_{coil} or increasing l_{gap} can decrease SAR. We don't want to reduce the driving current, since by doing so output power will also be decreased, which is undesirable, and adjust the gap length also has its physical limitation; the only parameters left here is the coil impedance. So here we propose using dual-coil structure, replacing one single coil with two smaller coil whose the total area equals to the original one. By reducing the size of each coil, the impedance of each coil is also decreasing, which leads to mitigation on SAR hot spot. When driven by currents with the same direction, the total magnetic field has little difference from its counterpart generated by the original coil.

We propose a new structure of the transmitter coil for reduction of the SAR value in the vicinity of the coil. The Tx coil is implemented as dual coils both with same current direction as illustrated in Fig. 2.28. The whole Tx antenna is composed of two rectangular $5cm \times 10cm$ coils, that is to say the area of the new structure antenna is almost the same

as the original square coil. The proposed structure should help in spreading out the the electric field and cancel the opposite one at internal edges. Also, we assume that the electric field generated by the two virtual wires at the each feed point will diminish each other, thus decreasing the SAR as well.

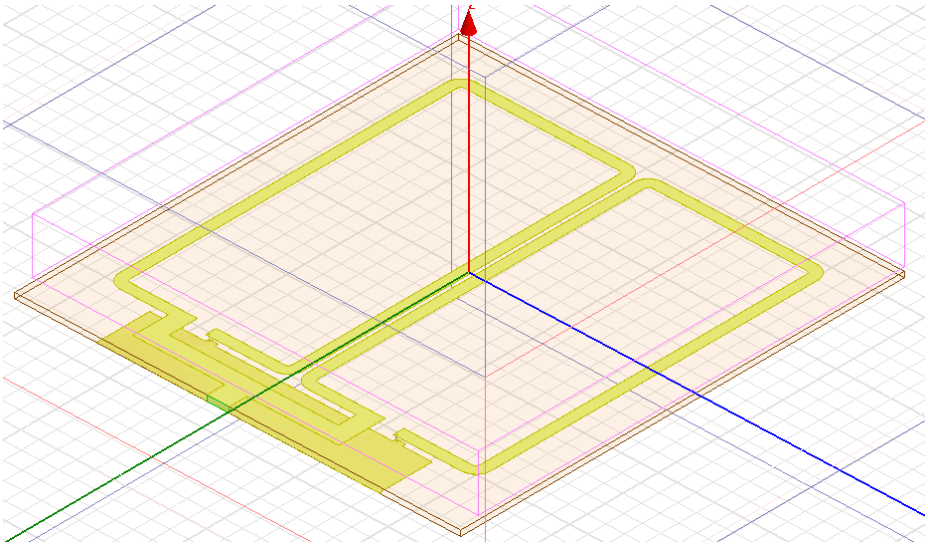

Figure 2.28: Structure of dual-coil with same current direction

We simulate a single-coil antenna and dual-coil antenna both driven by the current source with 400mA amplitude and then scale the maximum SAR point on the surface of the skin to FCC standard $1.6W/kg$, and compare the magnetic field at 5cm depth plane in the tissue. For comparison, we also simulate dual-coil with opposite current direction as an object of reference. The antennas of different structures are simulated, and trends of the field value, including magnetic field inside the body and peak SAR value, as the antennas are moving away from the tissue, are plotted. Besides these, we also simulate single-coil antennas with different trace widths to investigate how trace width will affect the fields value including maximum SAR, magnetic fields, etc.

Fig. 2.29 shows how the magnetic field and peak SAR change with the increase of gap

between antenna and tissue when excitations for all the antennas are fixed at 400mA. From these two plot, we can see that when driving currents are the same, single coils with different trace widths generate the magnetic field and SAR slightly different, but the differences diminish when the magnetic fields are normalized as shown in Fig. 2.30(a). Thus trace width will not have significant effect the normalized magnetic field and for the dual-coil antenna we fix the trace width to 3mm. It is obvious that the dual-coil antenna leads to the lower fields value than single-coil; this can be explained by the shunt of current in dual-coil structure. Dual coils with opposite currents generate opposite-direction magnetic field at tag plane but same-direction electric field at internal traces for both coils, leading to higher SAR and lower magnetic field than antenna with same current directions. Reinforcement effort of electric field at internal traces for dual-coil antenna with opposite current is evidently shown in Fig. 2.31.

Though dual-coil antenna has lower field value than single-coil antenna, after we scale their magnetic fields to normalized value dictated by the peak SAR value, the dual-coil antenna generates higher magnetic field at tag plane as illustrated in Fig. 2.30(a). However it is important to note, comparing the two plots in Fig. 2.30, that the increase of the magnetic field comes with the extra cost in the transmission power and lower efficiency. OD antenna has lower normalized magnetic field even it needs higher driving current, mostly due to the reinforcement effort of electric field and cancellation effort of magnetic filed.

Fig. 2.31 and fig. 2.32 compare the SAR distribution and magnetic field pattern for these three antenna structure, and this further verifies the SAR spread effort of DCSD antenna.

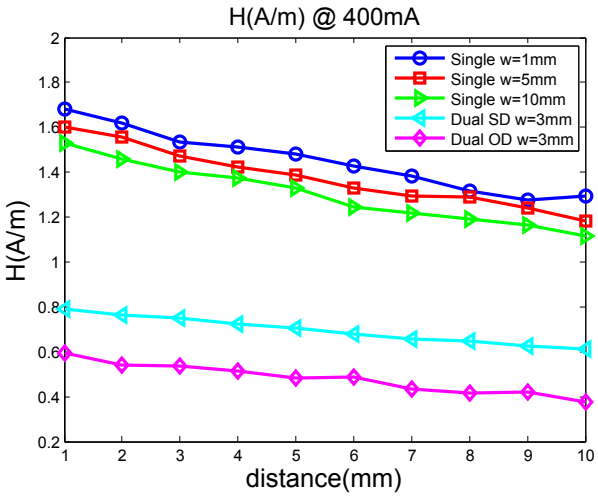

(a)

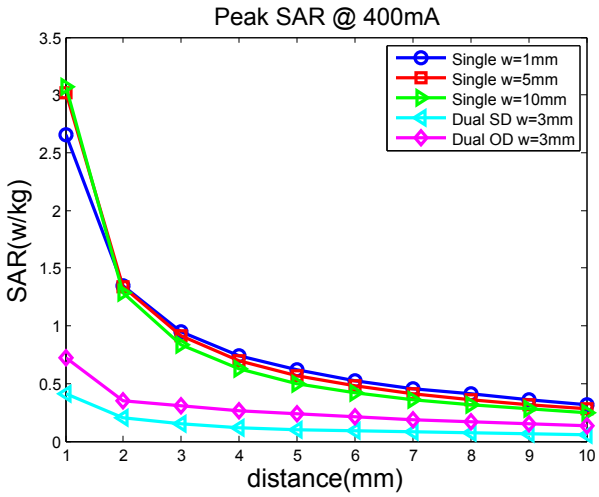

(b)

Figure 2.29: Magnetic field at the center of 5cm-depth plane and maximum SAR on tissue surface when driving current is 400mA

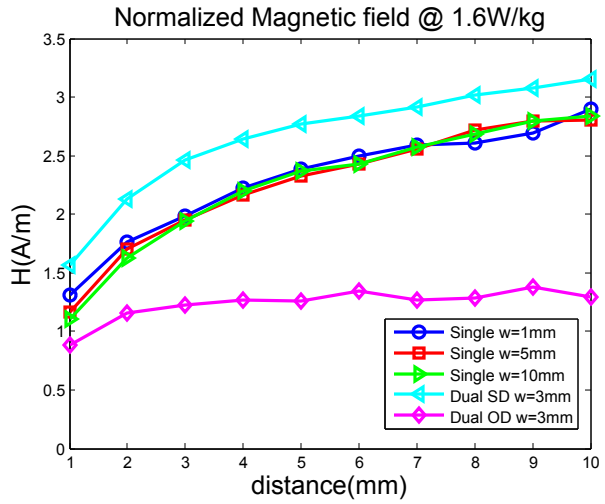

(a)

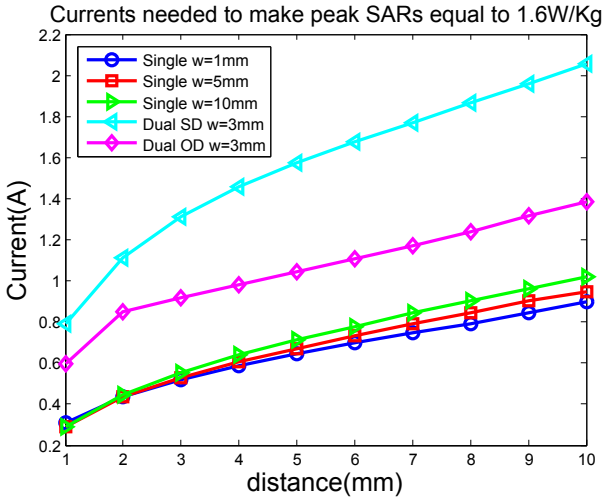

(b)

Figure 2.30: Normalized magnetic field at the center of 5cm-depth plane and corresponding driving current

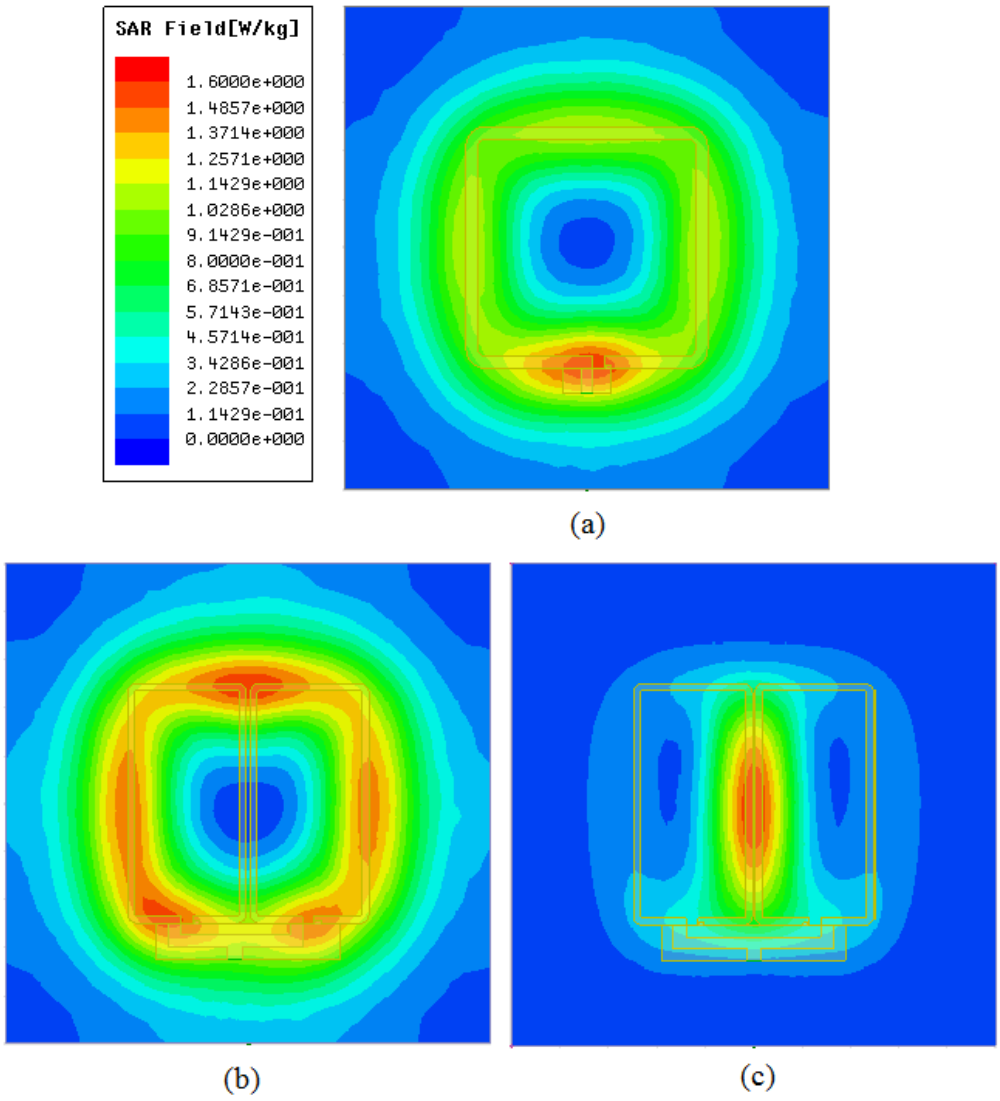

Figure 2.31: SAR pattern compare: (a) - SC antenna, (b) - DCSD antenna, (c) - DCOD antenna

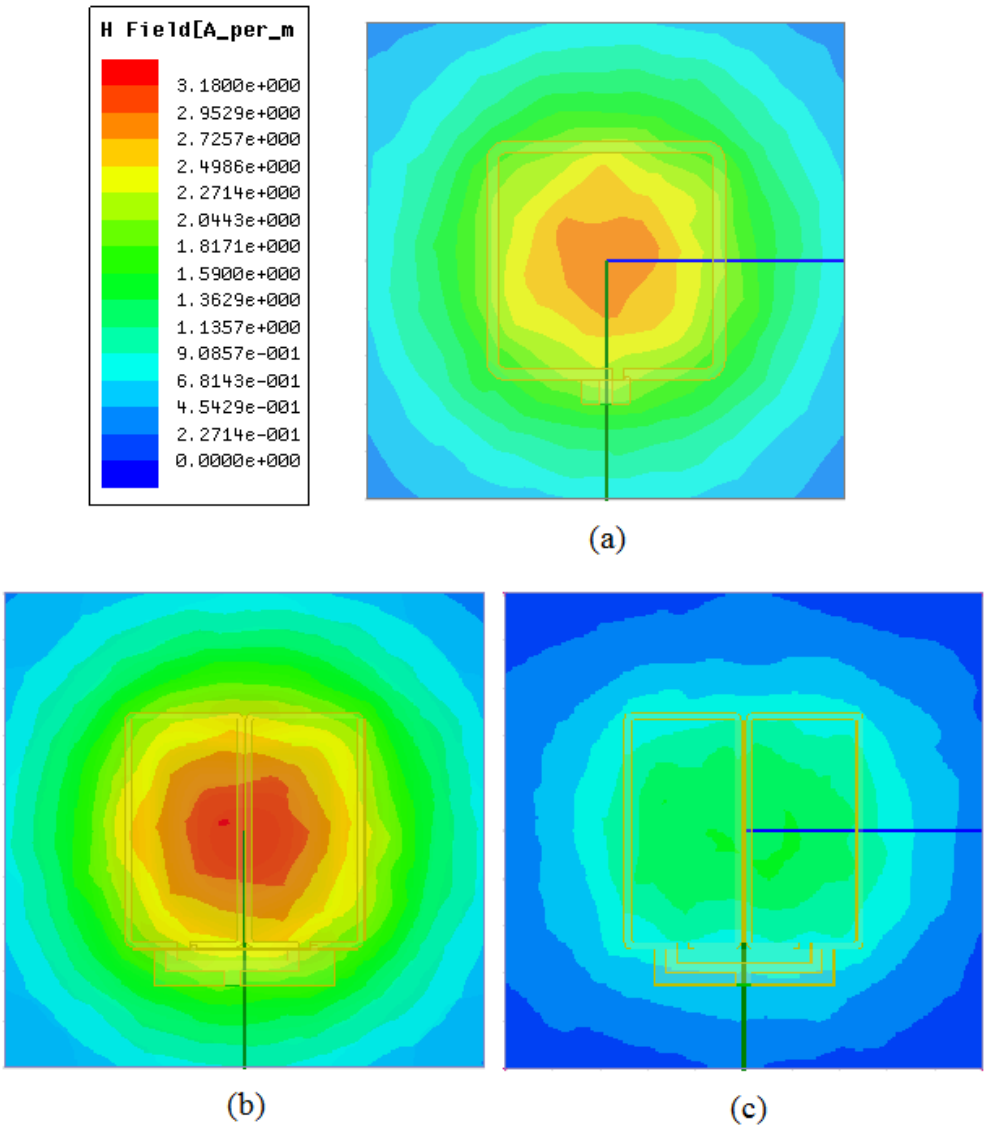

Figure 2.32: Magnetic field pattern compare: (a) - SC antenna, (b) - DCSD antenna, (c) - DCOD antenna

2.7.2 Misalignment between Tx and Rx coils

Another advantage of the dual transmitting coil is mitigating the misalignment effect. When angle between the two coil is exactly 90^o and the receiving coil is located at the axis of the transmitting coil, none of the magnetic field flux passes through the receiving coil and the two coils are completely decoupled. However, if the opposite currents drive the two transmitting coils, there will be magnetic field through the receiving coil. That is, by controlling the phase of the currents driving the dual coil, we can control the direction and amplitude of spacial magnetic field and thus mitigate the energy scarcity for millimeter size deep implanted device. The demonstration of combination of magnetic fields from two coils is shown in Fig. 2.33.

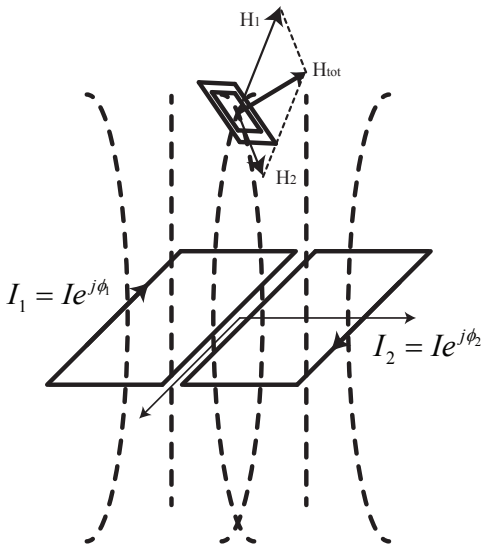

Figure 2.33: Combination of magnetic fields generated by two coils

We also investigate the performance of the link when the dual coils are separated. When distance between the two coils increase, instead of gathering around the center axis, the magnetic field spread out so that even the coil is not positioned at the center axis of the coil,

it can still extract fair amount of energy from the field.

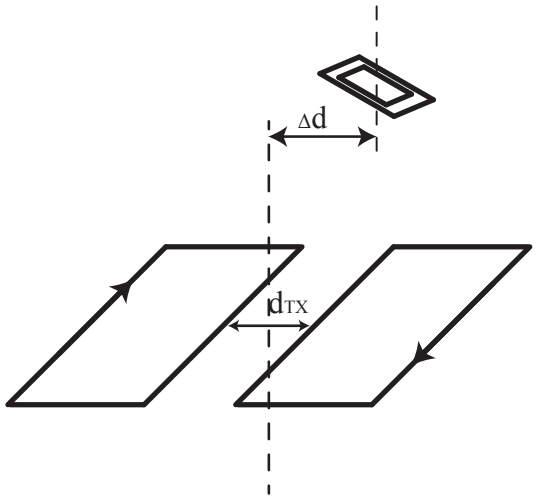

Figure 2.34: Separation of two coils can spread the field distribution

To investigate the performance of the dual coil with the different phase of the driving current under different misalignment conditions, we extract the 3-port network parameters of the three coil systems using HFSS simulator. The relation between voltages and driving current in three coils can be expressed by their Z-parameters as:

$$\begin{bmatrix} V_1 \\ V_2 \\ V_3 \end{bmatrix} = \begin{bmatrix} Z_{11} & Z_{12} & Z_{13} \\ Z_{21} & Z_{22} & Z_{23} \\ Z_{31} & Z_{32} & Z_{33} \end{bmatrix} \begin{bmatrix} I_1 \\ I_2 \\ I_3 \end{bmatrix}, \tag{2.66}$$

where V_i and I_i ($i = 1, 2, 3$) are the Root mean square (RMS) voltages and currents of the coils in the system, which was shown in Fig. 2.35. Then we can apply Thévenin equivalent circuits to the receiving coil. When two transmitting coils are driven by current I_1 and I_2,

the open-circuit voltage at the terminal of receiving coil is:

$$V_{open} = Z_{31}I_1 + Z_{32}I_2, \tag{2.67}$$

which is the generation voltage of the equivalent circuit; and Z_{33}, the impedance of the receiving coil, is the source impedance. Then the optimum load for maximum transmission efficiency can be calculated by Eq. (2.17a) and (2.17b). But since the coupling between the transmitting and receiving coils is too small, which is negligible during the calculation, basically we can assume that the optimum load is the conjugate of Z_{33}, and the optimum output power is:

$$P_{rx} = \frac{|V_{open}|^2}{4Re\{Z_{33}\}}. \tag{2.68}$$

Similarly, The total input power for the transmitting coil is:

$$P_{tx} = Re\{V_1 I_1^*\} + Re\{V_2 I_2^*\}, \tag{2.69}$$

where

$$V_1 = Z_{11}I_1 + Z_{12}I_2, V_2 = Z_{21}I_1 + Z_{22}I_2. \tag{2.70}$$

Then the transmission efficiency is:

$$\eta_C = \frac{P_{rx}}{P_{tx}}. \tag{2.71}$$

Fig. 2.36 shows the power efficiency of the inductive link as a function of the driving current phase difference φ and positional misalignment Δd for 4 typical rotational misalignment angle θ when the transmitting coils start to move away from each other. The rotational angle

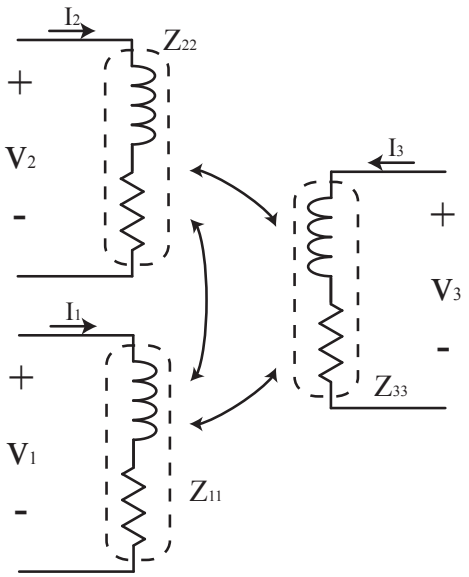

Figure 2.35: Illustration of voltage and current in three coil system

misalignment, We can observe that for the lower rotational misalignment the same currents in the dual coil outperform the driving currents with the different phase. However, with the increase in the rotational misalignment, the increased phase difference leads to the increase in the power efficiency. We also investigate the efficiency of the link when the dual coils are separated. Fig. 2.36, at the same time, demonstrate the benefits of separating the two transmitting coils. The power efficiencies with the same positional misalignment and the rotational misalignment of higher value, θ =60° and 90° in the plot, change but with the varying distance between the dual coils. As expected, by increasing the distance between the coils, the power efficiency for severe misalignment is increased.

Beside that, separating the transmitting coils can also decrease the SAR generated by them, thus allows more power deliver to the receiving coil. Fig 2.37 shows SAR value as the function of current phase difference φ for various coil separating distance d_{Tx}. As expected, for each d_{Tx}, SAR reaches its maximum value when the currents in two coils are

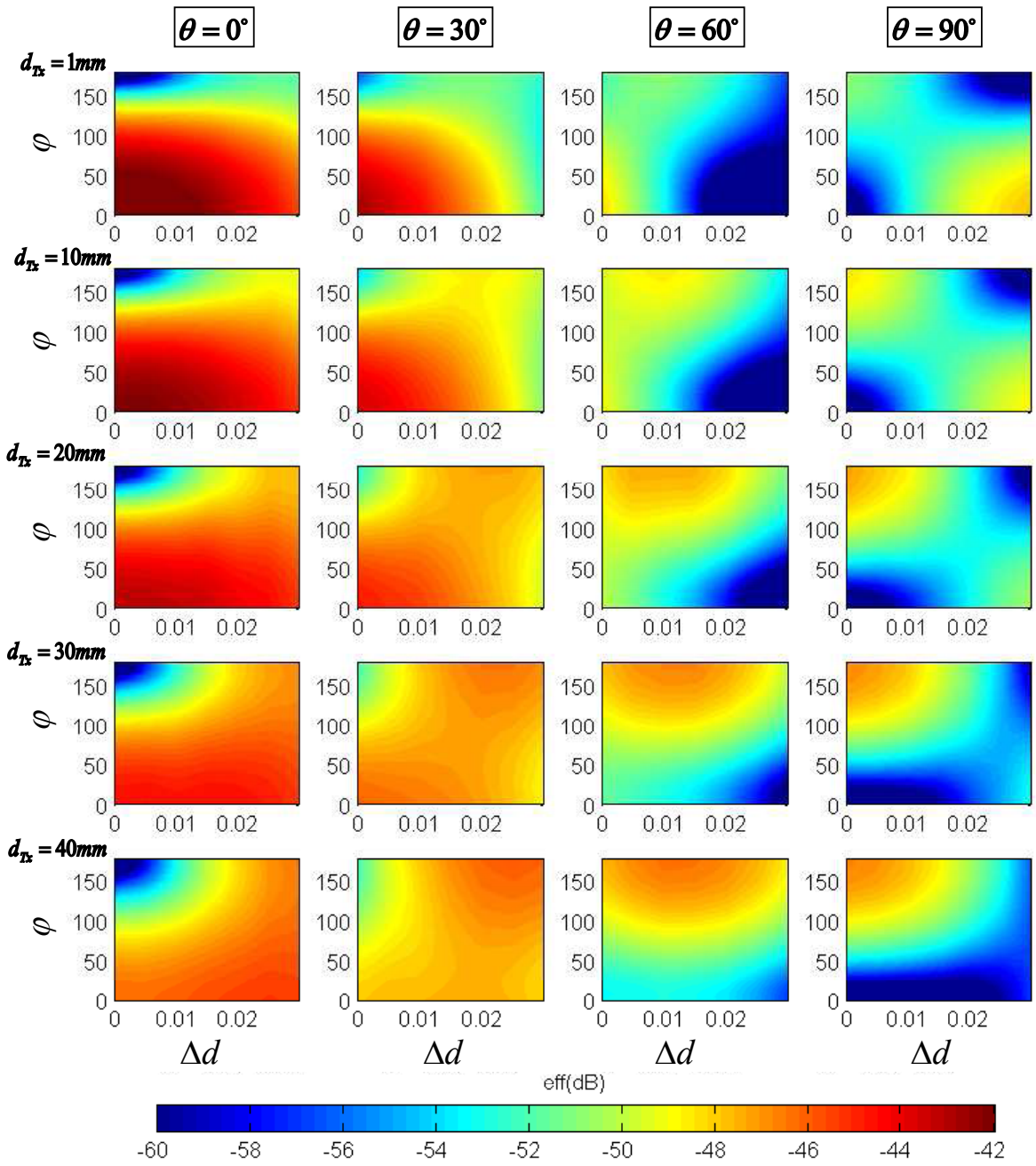

Figure 2.36: Investigation of η_C for different positional misalignment Δd and rotational misalignment θ when separation distance d_{Tx} and current phase difference φ between Tx and Rx coils are different

totally out of phase. Thus we use the maximum SAR as the standard to set up the limit on current amplitude for each transmitting coil pair. Fig. 2.38 shows the highest available power for different situations. From the plots, it's very obvious that with the decreasing SAR, the available power for the receiving coil increase a lot, especially for the one with severe positional misalignment and rotational misalignment.

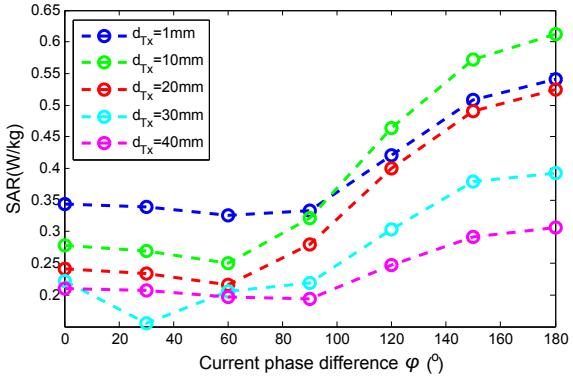

Figure 2.37: SAR plot for various current difference φ when driving current amplitude in each coil is 1 A

2.8 Rectifier design for implantable devices

One of the most critical component of the implanted device circuitry is the rectifier. As the interface between the external EM field and the internal power supply of the whole completely passive device, rectifier plays an important part in IMD system. The performance of the rectifier directly affects the behavior of the entire system. In this chapter we investigate several popular rectifier structures used in WPT system, discuss each characteristics and suitable situation, then choose the four-cell cross-connected rectifier considering low receiving signal property of deeply implanted device system. We also analyze how the rectifier works in the subthreshold region. Simulation results of the rectifier in 0.5m CMOS technology with

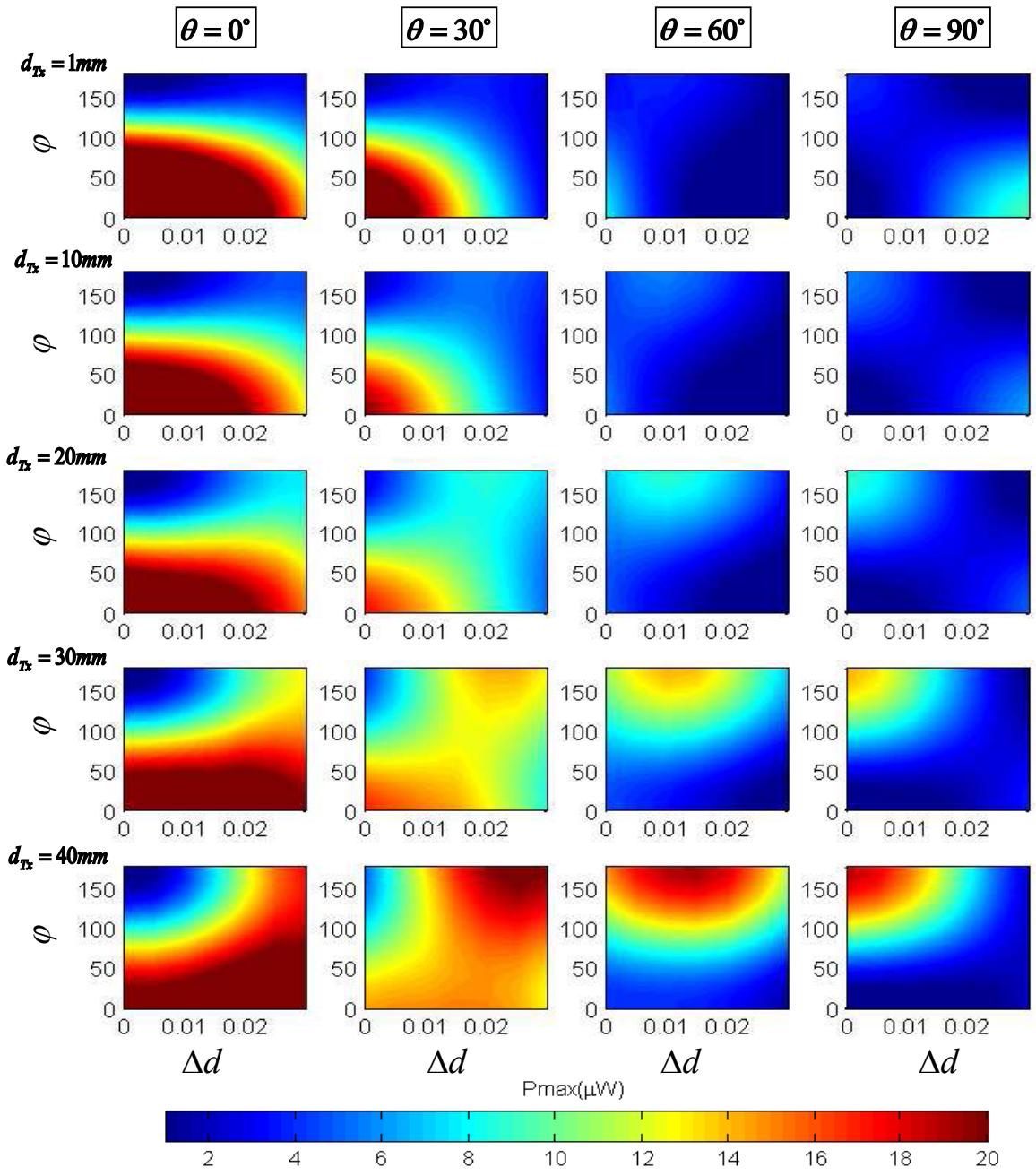

Figure 2.38: Investigation of P_{max} for different positional misalignment Δd and rotational misalignment θ when separation distance d_{Tx} and current phase difference φ between Tx and Rx coils are different

1V input at frequency 40MHz and rectifier with input 0.5V at 1kHz are presented.

2.8.1 Rectifiers Comparison

There are various rectifiers for different applications and working environment; each type of rectifier has its own properties and suitable working condition. This section will go over the structures that are commonly used in wireless power transfer system and find the proper one for our energy starvation environment.

Diode Connected full-wave Rectifier

Full-wave bridge rectifier is a conventional way to convert RF signal into DC power. It fully utilizes the RF input and generates a low ripple output voltage. The output voltage of the rectifier equals to amplitude of the input signal minus forward drop voltage of the diode. Standard CMOS process use diode-connected MOS transistor instead of Shottky diode for price consideration. However, high forward drop voltage make it only applicable in high-voltage applications, for instance, systems of which the reading distances are relatively small with respect to their antenna sizes. Some paper use cross-connected transistors instead of two diode-connected transistors in the rectifier to decrease voltage drop [50, 51], as you can see in Fig. 2.39. Then the output voltage for the rectifier is

$$V_{out} = V_{dd} - V_{ss} = V_{rf} - V_{drop}, \tag{2.72}$$

where V_{rf} is the amplitude of the incoming RF voltage, V_{drop} is the voltage drop on one diode-connected transistor, of which the value is

$$V_{drop} = V_{th} + \sqrt{\frac{2I_D}{\mu C_{ox}(W/L)}}, \tag{2.73}$$

where V_{th} is the threshold voltage for the transistor, μC_{ox} is the MOS transistor transconductance parameter, and W and L are width and length of the transistor respectively. However for most low power WPT system especially for those without low-threshold technology, that is still not enough.

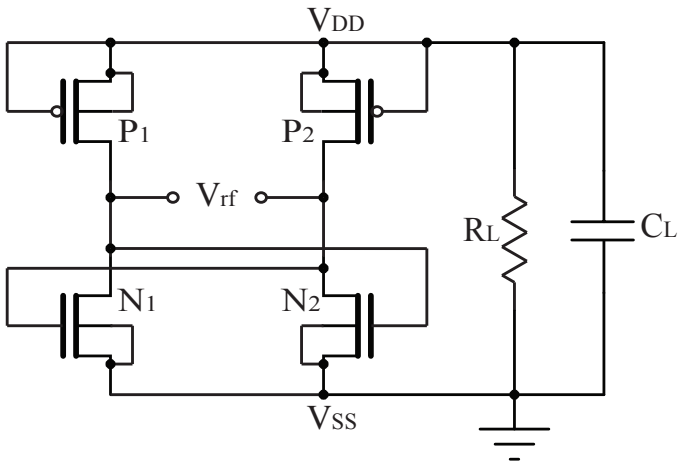

Figure 2.39: full-wave rectifier schematic

Voltage multiplier

When operating voltage in IMD is higher than input voltage V_{rf} at terminal of Rx coil, voltage multiplier is another popular choice to extract EM power to generate voltage much higher than the amplitude of input voltage. We can see in schematic of CMOS voltage multiplier in Fig. 2.40. Voltage increment for one stage is $\Delta V = V_{rf} - V_{drop}$, then the voltage for the whole multiplier with n stages is $V_{out} = n(V_{rf} - V_{drop})$. And to decrease body-effect on the output when the number of stages is large, PMOS is preferred during the implementation[52]. However, similar with full-wave rectifier, high forward drop voltage on the diode is still a big issue if Schottky diode or low V_{th} technology is not available. We also need to be aware of the total power consumption of voltage multiplier when large number

of stages is needed to achieve high output voltage.

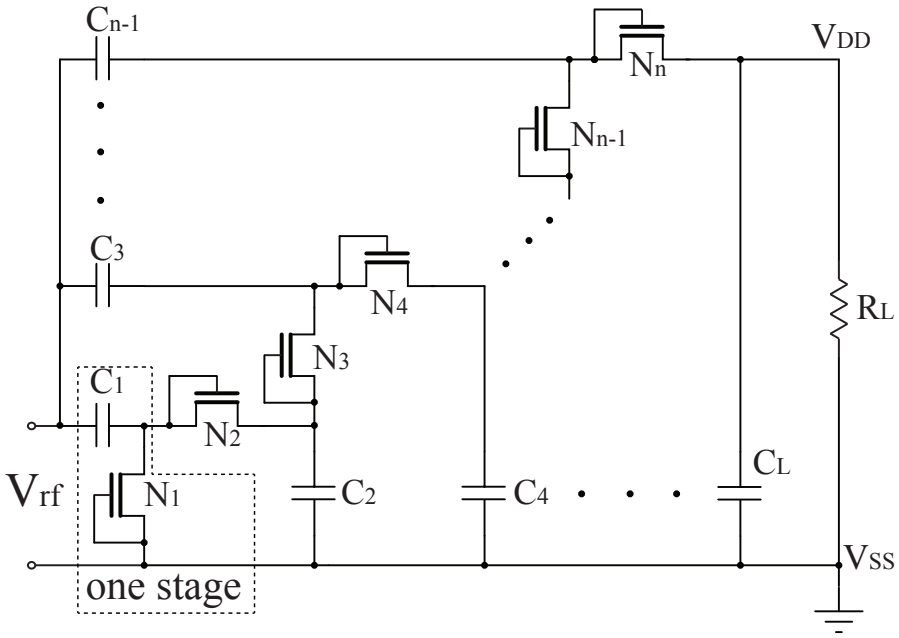

Figure 2.40: Voltage Multiplier schematic

Cross-connected bridge Rectifier

Cross-connected bridge rectifier(Fig. 2.41) is a good choice for those whose input signal is comparable with the threshold voltage of the transistor. Different from diode-connected rectifier whose drain-source voltage of the transistor should be as large as the turn-on voltage, the transistor in cross-connected rectifier can work in triode region; then the voltage drop across the transistor can be relatively small, which greatly improve the output voltage and PCE of the rectifier for small input. Thus our attention will be focused on this type of rectifier according to the characteristic of our system. Next section will render a detail analysis of it.

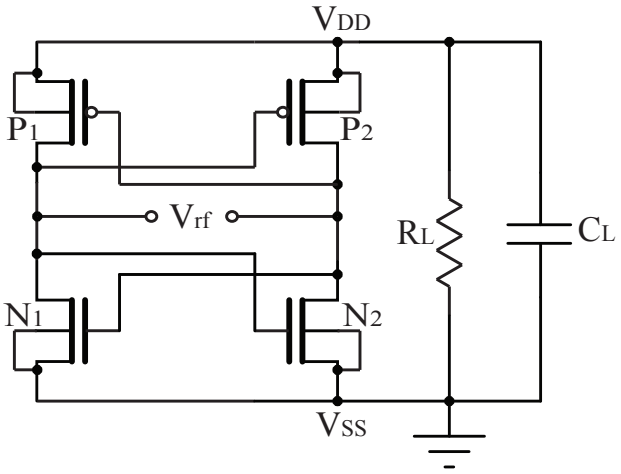

Figure 2.41: full-wave rectifier schematic

2.8.2 Cross-connected Rectifier Analysis

Basic Principle

As we can see in Fig. 2.41, four transistors work as switches. $P1$-$N2$ pair and $P2$-$N1$ pair are turned on alternatively. As you can see in Fig. 2.42a. During each half switching period, current from RF source runs through either PMOS-NMOS pairs to charge the load capacitance on the same direction. V_{drop} in this structure is twice of the voltage drop over the linear resistance of the transistor. So transistor with larger size will have lower on-resistance, and thus lower V_{drop} and higher V_{out}. We should also notice that during each half of switching cycle, there is a certain period when input voltage is smaller than output voltage and also the transistor is turned on; then the roles of transistor source and drain are exchanged (Fig. 2.42b), the current, which is called backward current, will flow out of the capacitance, causing the load capacitor being discharged. Backward current will reduce the PCE of the rectifier, and it is also proportional with the size of the transistor. Thus there

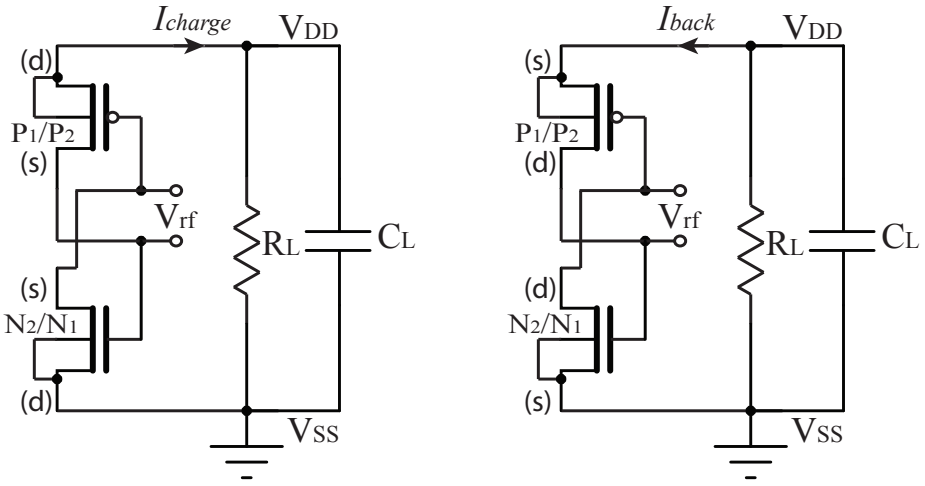

(a) Charging (b) discharge

Figure 2.42: Equivalent circuit of cross-connected bridge rectifier in (a) charging and (b) discharging phases of operation.

must be an optimum value for the size of the transistors to achieve best PCE.

Design Consideration

There is two design purpose for the rectifier, the output voltage and the PEC of the rectifier. For arbitrary input signal and load resistor, we can achieve a certain output voltage by adjusting the size of transistors. According to steady state analysis, the charging current will be balanced with the current dissipated on load and the backward current. For transistor working under linear region, the drain current is proportional with V_{DS} and (W/L). When transistor width is very large, small V_{DS} of MOSFET is just enough to generate drain current that is needed to balance the dissipating current. So theoretically, even for small load resistance, that is to say high load current, we can still get desire voltage by properly sizing the transistors. We use matlab and cadence to simulate this, and we can see the result in Fig. 2.43. Both results are compatible with this statement; some difference between the

calculation and simulation results may be come from parasitic parameter of the transistor when transistor size is too large. Note that we already make the width ratio of PMOS and NMOS at $(W/L)_p/(W/L)_n = (\mu_n C_{ox})/(\mu_n C_{ox})$ in order to make analysis more easier.

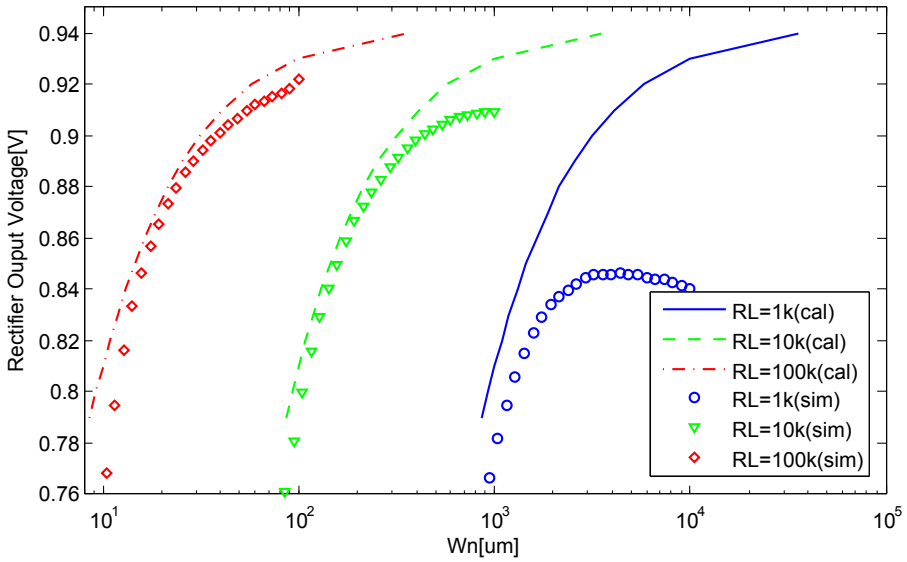

Figure 2.43: V_{OUT} from Calculation and Simulation for different loads ($V_{rf} = 1V$)

But talking about the PCE of the rectifier, the situation is a little different. It is known that PCE will decrease when input signal is larger than a certain value due to the increase of the backward current [53]. Even for a given input signal, conversion efficiency will decrease as you can see because of the same reason. This is some disagreement between the calculation result and simulation result, because for one thing we neglect substrate loss in Matlab calculation, for another thing the.

When high voltage is required, rectifiers can be cascaded in series to generate high output voltage

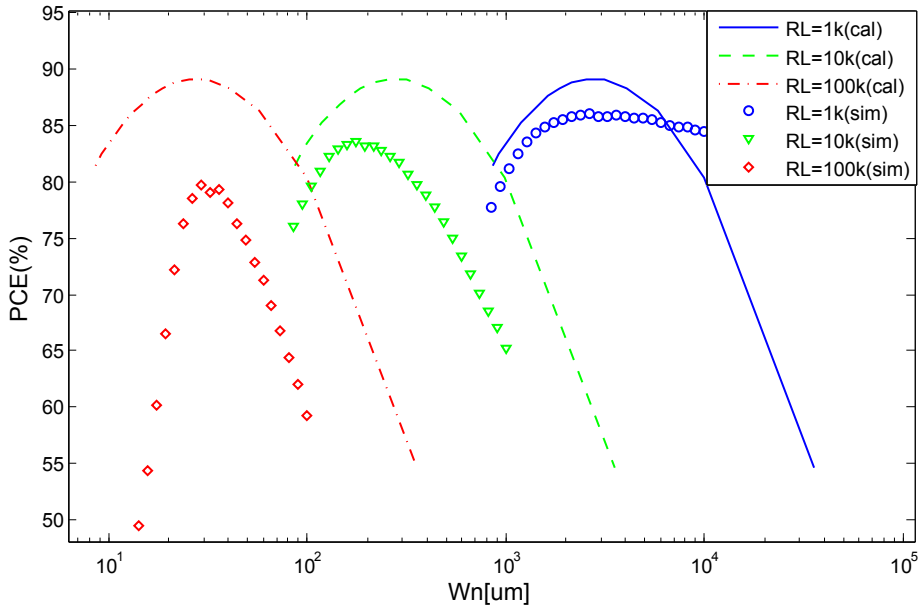

Figure 2.44: PCE from Calculation and Simulation for different loads ($V_{rf} = 1V$)

2.8.3 Cross-connected Rectifier with Extremely Small Input

In our project, there is even a possibility that the input voltage may be still lower than transistor threshold voltage, because of the small size and relatively long reading distance of the whole system, as well as the 0.5um technology we use for cost consideration. Then the rectifier will probably work under subthreshold region.

But in system operating in dual-mode, the receiver doesn't need to convert and provide power to function circuitry simultaneously; so when designing rectifier in this system, compare to the PCE of the rectifier we need to pay more attention on how large the output voltage we can achieve.

Cause the transistors are working in subthreshold when input is very small, it is more convenient to use EKV model to give drain current:

$$I_D = 2n\mu C_{ox} {U_T}^2 \frac{W}{L} \left[exp\left(\frac{V_P - V_S}{U_T}\right) - exp\left(\frac{V_P - V_D}{U_T}\right)\right] \tag{2.74}$$

Where U_T is the thermal voltage, V_P is the the pinch-off voltage given by

$$V_P = \frac{V_G - V_{T0}}{n} \tag{2.75}$$

And the expression for slope factor n is:

$$\frac{1}{n} = 1 - \frac{\gamma}{2\sqrt{V_G - V_{T0} + \left(\frac{\gamma}{2} + \sqrt{\phi}\right)^2}} \tag{2.76}$$

Here we need to notice that under subthreshold, there is not a threhold voltage V_T below which the transistor is turning off; when $V_{GS} > 0$ for NMOS or $V_{GS} < 0$ for PMOS, transistor conduct either forward charging current or backward current. Fig. 2.45 shows this situation. Also, in real world, even chip is in stand-by mode, there is still some leakage current, the size of the transistors should be large enough to make sure that drain current is much higher than I_{leak}; otherwise the C_L cannot be charged up. Also, subthreshold operation is preferable for low frequency circuit, cause the reduced channel conductance. The rectifier working in subthreshold will generate harmonic distortion current at frequency above 1MHz. Then initially we will investigate how rectifier works at low frequency, like 10kHz.

We extract EKV parameters from BSIM3V3 model[54]; and the analyze method is similar with that in previous section. Fig. 2.46 shows V_{OUT} of rectifier v.s. transistor size at $Vrf = 0.5V$, $I_{leak} = 1nA$ and $f = 10kHz$; and compare the simulation result with calculation result. We can see that calculation result is not far away from simulation result, it is really good for our design procedure since just using Cadence simulation will be very time-consuming.

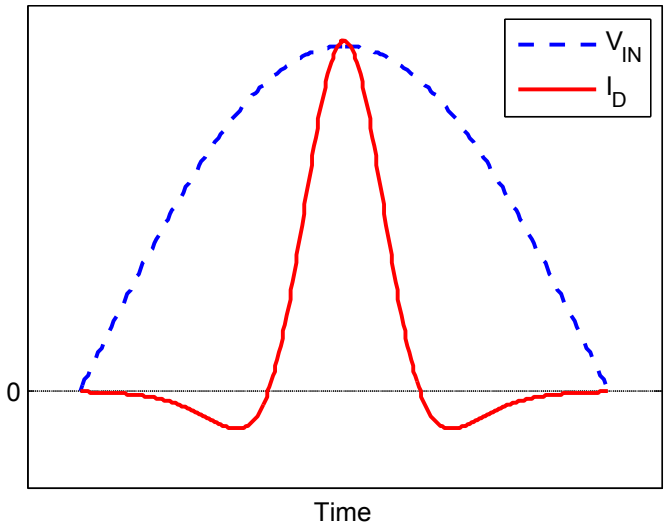

Figure 2.45: Input voltage and transistor current

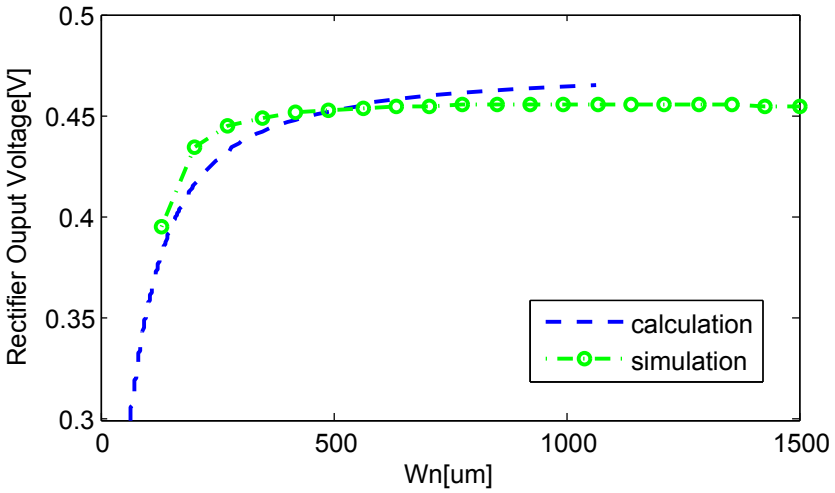

Figure 2.46: V_{OUT} vs wn for small input ($V_{rf} = 0.5V$, $I_{leak} = 1nA$)

2.9 Conclusion

In this chapters, analytical analysis with the close-form equations based on quasi-static EM approximation and numerical simulation for full-wave analysis is combined together for analysis of the EM performance in the whole system: the former method helps us acquire a basic knowledge of the working principles of the wireless power transfer through coils and gain a intuitive viewpoint over the link design, while the full-wave analysis provided by the EM solver, serves as our main research tool in design of EM link. Based on that, the optimum frequency and optimum positioning of Tx coil to delivering maximum power to 3 mm $\times$ 3 mm receiving coil with 5 cm deep implanted depth is investigated. Last, we propose adaptive transmitting coil array to further improve the robustness and flexibility of the system.

Chapter 3

Hardware optimization for Backscatter-based tag-to-tag communication

3.1 Introduction

Backscatter-based tag-to-tag communication (BBTT) is a innovative communication paradigm wherein radio-less devices communicate with each other purely using passive backscatter modulation. Its concept was first brought up by Nikitin [13] and the communication link was first studied and presented in [14]. This makes for highly inexpensive and low power consumption devices, and thus draws great antention in recent years. By building a network based on BBTT communication, the tags talk to each other by backscattering existent external excitation signal, the source which can be dedicated continuous wave (CW) exciters or ambient EM field sources like WiFi access points, TV towers, cell phone towers, etc. Combination of this paradigm and multihop communication will allow for building low-

cost networks with great scalability and flexibility. This type of communication networks is very promising in exploring the vast potential of the IoT.

There are two main components in the tags that determine the range and robustness of a passive tag-to-tag link, the analog front end (AFE) and the backscatter modulator (BM). Conventional backscattering devices like RFID tags are mainly designed to communicate with an active reader leading to a centralized framework centered on the reader. The literature on design of the AFE and BM of traditional passive tags optimized to communicate with active readers is rich [47][55]. However, the difference of the communication scenario result in the differences of design pattern and strategy. In this chapter, we focus on the design constraints, optimization goals and tradeoffs involved in the design of the AFE and BM for BBTT tags. The BBTT link will be characterized by mathematical equations and then verified with simulations our attempts of determine the optimal parameters of the AFE and BM circuits.

In this chapter, we are going to first give a brief introduction of BBTT communication system and compare it with conventional RFID system; basic block module for the tags in the two systems will also be talked . Then based on the unique communication characteristic of BBTT system, AFE and BM design for BBTT tags will be illustrated, especially for issues of solving phase cancellation problem and mitigate low modulation depth problem for passive detection. At last, the prototype of the BBTT tag and experiment result will be demonstrated.

3.2 Brief introduction of BBTT communication system

A conventional RFID system usually include a reader and a bunch of tags, in which the reader uses an active transmitter to generate continuous waves (CW) and send query signals to the tags, and a homodyne receiver to receive backscattering signal from RFID tags, while the tags response to the reader by modulating the reflection cross section (RCS) of the tag antennas. This communication paradigm establish a centralized telecommunication model as demonstrated in Fig. 3.2, where in stead of autonomously "talking" to each other, all the tags can only communicate with the RFID reader. This scheme greatly restrict the capabilities, scalability and flexibility of IoT.

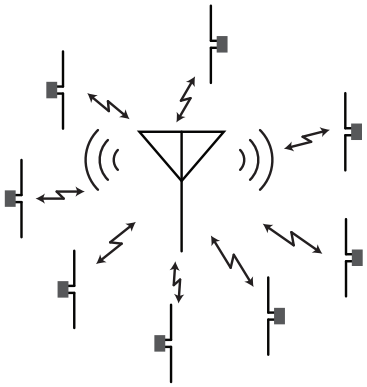

Figure 3.1: Communication paradigm of conventional RFID system

Backscatter based tag-to-tag (BBTT) system, which allow the tagged objects wherein to communicate with each other independently, can overcome the aforementioned limitations of RFID system and help achieve the vision of IoT. In this system it also has a reader-alike device, but instead of serving as communication headquarter, it just provides CW field as communication media through which tags can send messages by modulating it without using

active radio component. To differentiate this device from the reader in RFID system, we will call it CW generator or CW exciter in the following part. The concept of BBTT system has been shown in Fig.3.2.This innovative BBT communication paradigm draw a lot of research interest in recent years. P. Nikitin has demonstrated the passive communication between two RFID tags at a short distance in [13]; and G. Marrocco developed a eletromagnetic model for this communication system. A radio-less EPC Gen 2 compliant device (named sensatag), which can communicate with Gen 2 RFID reader as well as listening to nearby Gen 2 tags, has been developed [18] and applied for precise indoor localization and tracking in passive RFID systems [17]. Besides EM field generated by a CW exciter, some researchers also utilize ambient EM signal generated by existing wireless infrastructure, like TV signals [16] and WiFi signal [15], as a backscatter source to enable tag-to-tag communication.

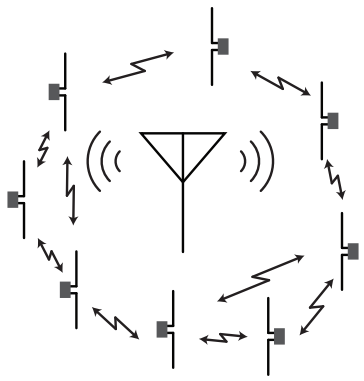

Figure 3.2: Communication paradigm of backscatter-based tag-to-tag system

The communication scenario of these two system is different, which will lead to the differences on corresponding tag design strategies and optimization standard also. In this section, we review the basic blocks that BBTT tag circuit needs to function passive communication without active transmitter on board, and their difference from conventional RFID tag.

As shown in Fig. 3.3, both a basic BBTT tag and a conventional RFID tag should

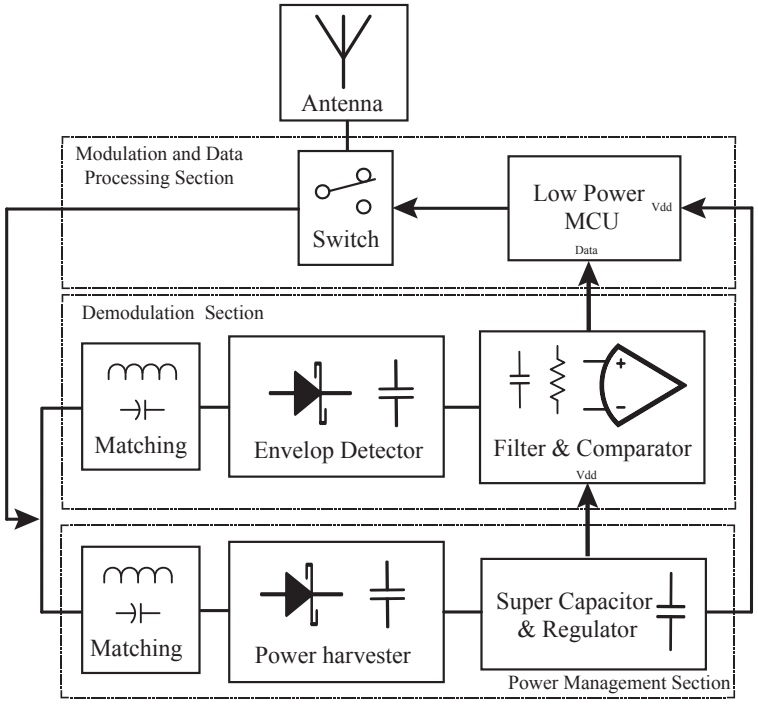

Figure 3.3: Basic circuit block diagram of BBTT tag

contain an antenna, demodulation section, data processing & modulation section and power management section. To achieve isotropic communication on horizontal plane, a dipole-style antenna with its donut-shape radiation pattern is a good choice for BBTT tag, and a lumped LC balun is deployed between the antenna and SMA connector for good radiation performance. The demodulation section circuitry, shown in Fig. 3.4, commonly comprises a voltage multiplier as envelop detector with impedance matching circuit in front and low pass filters (LPF) followed to extracts the baseband signal from the carrier. The task of the LPFs following the envelope detector is to cut off unwanted frequency components and distinguish the different voltage levels in the baseband signal that correspond to different values of the input power at the antenna output. The common implementation of this circuit using discrete components is the generation of an average signal that is compared to the baseband signal.

The demodulated digital signal will be processed by a low power microcontroller (MCU). To transmit data to another BBTT tag, MCU can control the switch, acting as modulator or a passive transmitter to backscatter the CW signal or environmental EM field by changing the load impedance Z_L of the antenna as well as the differential radar cross section RCS. The differential RCS equation is provided by [56]:

$$\Delta\sigma = \frac{\lambda^2 {G_A}^2}{4\pi}|\Gamma^*_{L,1} - \Gamma^*_{L,2}|^2, \tag{3.1}$$

where λ is the wavelength of CW, G_A is the antenna gain, and $\Gamma^*_{L,i}$ is the conjugate antenna reflection coefficient at different modulation states, which can be expressed by:

$$\Gamma^*_{L,i} = \frac{Z^*_A - Z_{L,i}}{Z_{L,i} + Z_A}, i = 1, 2. \tag{3.2}$$

Modulator is usually fulfilled by a switch with different load type depending on the employed digital modulation method. These demodulation section and modulation section are usually critical part for a robust and reliable communication link.

The power harvesting circuit, shown in Fig. 3.5, is built up from a voltage multiplier that transforms a low input voltage into a voltage that matches the supply voltage of the demodulation and decoding circuits. An impedance matching circuit is added in front of the voltage multiplier to maximize the power transfer from the antenna and minimize the reflection of the power. As the impedance of the voltage multiplier depends on the input power due to the nonlinearity of diodes, the input impedance of the power harvesting circuit can only be power matched to the antenna for a single input power. To optimize the the power harvesting circuit performance at low power circumstances, the impedance is exactly matched at the minimum expected operating power for the tag is expected to operate. For higher input power, due to mismatch in the impedance, power will be reflected at the input of the impedance matching circuit. This leads to an additional constraint on the design of the impedance matching circuit in the case of higher input power than the minimum. The voltage multiplier is followed by a voltage regulator which will provide a regulated supply voltage for the demodulation circuit and the decoding logic.

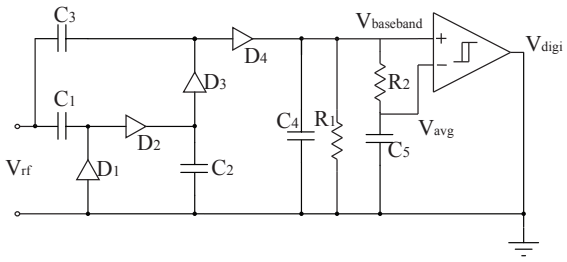

Figure 3.4: Demodulator circuit for a passive tag.

The basic block diagram and fundamental theory for backscattering and passive detection

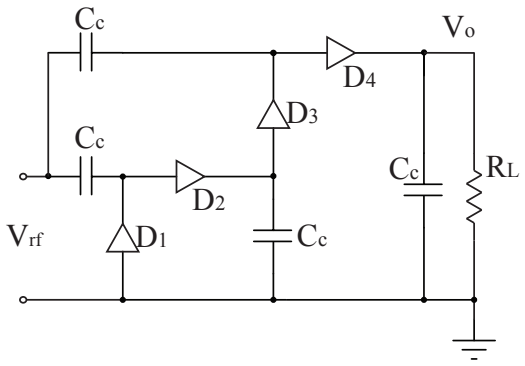

Figure 3.5: Power harvesting circuitry comprising two stages of voltage multiplication.

is very similar between conventional RFID tags and BBTT tags. However there are some issues in BBTT diagram which is not so severe in passive tag communicating with active reader, like phase cancellation and detection of signal with low modulation depth. We'll address those issues specifically with mathematical analysis in the following sections, and propose solution and optimization method for it.

3.3 Backscatter Modulation Design

3.3.1 Backscattered field of tag

In this section, we are going to introduce some antenna fundamental first. Most of the fundamental theory is coming from the antenna book [57]. The far-zone electric field $\mathbf{E}_a$ observed at distance d can be expressed by its driven current I_a and antenna equivalent vector effective length $\mathbf{l}_e$:

$$\mathbf{E}_a = -j\eta\frac{\beta I_a}{4\pi d}\mathbf{l}_e e^{-j\beta d} = -j\mathbf{i}_{\mathbf{l}_e}\frac{\eta I_a}{2\lambda d}\left|\mathbf{l}_e\right| e^{-j\beta d}, \tag{3.3}$$

where $\mathbf{i}_{\mathbf{l}_e}$ is the unit vector of antenna effective length, η is the medium impedance which is 377 Ω for free space and air, β is the propagation constant given by $2\pi/\lambda$, and λ is the wave length. According to [58], $\mathbf{l}_e$ is associated with the antenna gain G and radiation resistance R_A of the antenna, which is the real part of Z_A:

$$|\mathbf{l}_e| = \sqrt{\frac{G\lambda^2 R_A}{\pi\eta}}. \tag{3.4}$$

Effective length $\mathbf{l}_e$ can also be used to derive the induced open-circuit voltage V_{op} when incident electric field for receiving antenna is $\mathbf{E}_{inc}$:

$$V_{op} = \mathbf{E}_{inc} \cdot \mathbf{l}_e. \tag{3.5}$$

The Thévenin equivalent circuits for transmitting antenna and receiving antenna are shown in Fig. 3.6 and Fig. 3.7 respectively. When impedances of transmit and receive antennas are conjugate-matched to transmitter and receiver, it's very easy to derive the power relationship of a general radio link consisting a transmitter and a receiver:

$$P_{\mathrm{r}} = \frac{P_{\mathrm{t}} G_{\mathrm{t}} G_{\mathrm{t}} \lambda^2}{(4\pi d)^2}, \tag{3.6}$$

where P_{t} and P_{r} are the general transmitting and receiving power in the link, G_{t} and G_{r} are corresponding transmitter and receiver antenna gain, d is the communication distance and λ is the wavelength. And this euqation is the famous Friis's formula [57].

Based on antenna scattering theory developed by Hansen [59], the scattered field from an antenna in terms of load at the antenna Z_L as:

$$\mathbf{E}_{scat}(Z_L) = \mathbf{E}_{scat}(Z_A^*) + \Gamma_L^* \frac{\mathbf{E}_a I_m^*}{I_a}. \tag{3.7}$$

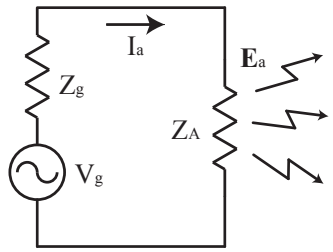

Figure 3.6: Thévenin equivalent circuits for transmitting antenna and radiation field

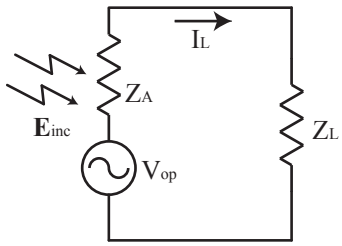

Figure 3.7: Thévenin equivalent circuits for receiving antenna

The first term $\mathbf{E}_{scat}(Z_A^*)$ is the structural scattering field cased by the current I_m^* induced on the antenna surface by incident field when the load of antenna is conjugate matched; it is independent of load impedance Z_L. The second term $\mathbf{E}_a$ is the antenna mode scattering field related with antenna radiation characteristic, in which $\mathbf{E}_a$ is the radiation field when I_a is the driven current, and Γ_L^* is conjugate antenna reflection coefficient given by Eq. (3.2). Eq. (3.7) can be easily transferred into the following form [60]:

$$\mathbf{E}_{scat}(Z_L) = \frac{\mathbf{E}_a I_m^*}{I_a}\left(A + \Gamma_L^*\right), \tag{3.8}$$

then A is expressed as:

$$A = \frac{\mathbf{E}_{scat}(Z_A^*) I_a}{\mathbf{E}_a I_m^*}. \tag{3.9}$$

A is a complex, the induced antenna surface current related coefficient, which is dependent

on antenna geometrical layout and EM properties of the material. For thin layer dipole-like antenna, A can be approximated as 1 [57].

For conjugate matched antenna, the corresponding induced conjugate current I_m^* is

$$I_m^* = \frac{V_{op}}{Z_A + Z_A^*} = \frac{\mathbf{E}_{inc} \cdot \mathbf{l}_e}{2R_A}. \tag{3.10}$$

After substituting I_m^* into Eq. (3.8), and applying the radiation equation Eq. (3.3), the scattered field observed at d distance away from backscattering antenna is

$$\mathbf{E}_{scat}(Z_L) = -j\frac{\eta e^{-j\beta d}}{4\lambda R_A d}\left(\mathbf{E}_{inc} \cdot \mathbf{l}_e\right)\mathbf{l}_e\left(1 + \Gamma_L^*\right) \tag{3.11}$$

$$= -j\mathbf{i}_{\mathbf{l}_e}\sqrt{p_e}\frac{\eta e^{-j(\beta d + \theta_{\mathbf{E}_{inc}})}}{4\lambda R_A d}\left|\mathbf{E}_{inc}\right|\left|\mathbf{l}_e\right|^2\left(1 + \Gamma_L^*\right), \tag{3.12}$$

where $\theta_{\mathbf{E}_{inc}}$ is the phase change introduced by incident field $\mathbf{E}_{inc}$, p_e polarization efficiency:

$$p_e = \frac{\left|\mathbf{E}_{inc} \cdot \mathbf{l}_e\right|^2}{\left|\mathbf{E}_{inc}\right|^2\left|\mathbf{l}_e\right|^2}; \tag{3.13}$$

p_e equals to 1 for polarization match. Relating $\mathbf{l}_e$ with antenna gain G and resistnace Z_A by (3.4), $\mathbf{E}_{scat}(Z_L)$ can be further transferred to

$$\mathbf{E}_{scat}(Z_L) = -j\mathbf{i}_{\mathbf{l}_e}\sqrt{p_e}\frac{G\lambda}{4\pi d}e^{-j(\beta d + \theta_{\mathbf{E}_{inc}})}\left|\mathbf{E}_{inc}\right|\left(1 + \Gamma_L^*\right), \tag{3.14}$$

If we apply the above derived equations into the RCS definition formula:

$$\sigma = \lim_{d\to\infty}\left[4\pi d^2\frac{\left|\mathbf{E}_{scat}\right|^2}{\left|\mathbf{E}_{inc}\right|^2}\right], \tag{3.15}$$

where d is the observation distance, we can get differential RCS as shown in Eq. (3.1).

3.3.2 The phase cancellation problem

Fig. 3.8 shows a BBTT system with one CW exciter and two tags, one is labeled as Tx tag to backscatter the message to the other tag labeled as Rx tag. The respective distances between three devices are shown in the figure. The CW exciter has an antenna with gain G_{CW}, resistance R_{ACW}, the two tags have identical antenna characteristic gain G_{tag} and resistance R_{Atag}. Here we assume that all the antennas in the system have been positioned optimally so that there is no polarization losses, which means the vector effective length of all the antenna have the same direction $\mathbf{i}_{\mathbf{l}_e}$ and $p_e = 1$. By using Eq. (3.3) and (3.4), we can

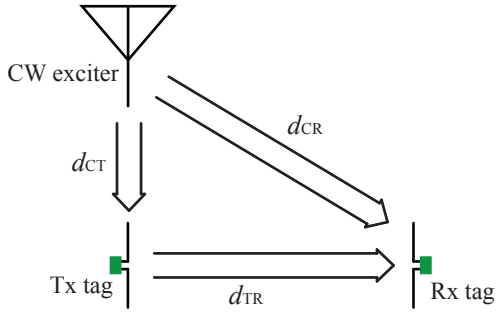

Figure 3.8: A BBTT system with one CW exciter and two tags

get the electrical field received by Tx and Rx tags from exciter as:

$$\mathbf{E}_{\mathrm{tC}} = \mathbf{i}_{\mathbf{l}_e} I_{\mathrm{CW}} \sqrt{\frac{\eta G_{\mathrm{CW}} R_{\mathrm{ACW}}}{4\pi d_{\mathrm{CT}}^2}} e^{-j(\beta d_{\mathrm{CT}} + \frac{\pi}{2})} = \mathbf{i}_{\mathbf{l}_e} A_{\mathrm{tC}} e^{j\theta_{\mathrm{tC}}}, \tag{3.16}$$

$$\mathbf{E}_{\mathrm{rC}} = \mathbf{i}_{\mathbf{l}_e} I_{\mathrm{CW}} \sqrt{\frac{\eta G_{\mathrm{CW}} R_{\mathrm{ACW}}}{4\pi d_{\mathrm{CR}}^2}} e^{-j(\beta d_{\mathrm{CR}} + \frac{\pi}{2})} = \mathbf{i}_{\mathbf{l}_e} A_{\mathrm{rC}} e^{j\theta_{\mathrm{rC}}}, \tag{3.17}$$

where I_{CW} is driving current in the CW exciter. Then from Eq. (3.14), we can get the backscattered signal received by Rx tag from Tx tag at two different modulation states as:

$$\begin{aligned}\mathbf{E}_{\mathrm{rxBck,i}} &= \mathbf{i}_{\mathbf{l}_e} \frac{G_{\mathrm{tag}}\lambda}{4\pi d_{\mathrm{TR}}} e^{-j(\beta d_{\mathrm{TR}}+\frac{\pi}{2})} \mathrm{E}_{\mathrm{tC}} \left(1+\Gamma^*_{\mathrm{L,i}}\right) \\ &= \mathbf{i}_{\mathbf{l}_e} A_{\mathrm{sconj}} e^{j\theta_{\mathrm{sconj}}} \left(1+\rho^*_{\mathrm{L,i}} e^{j\theta^*_{\mathrm{L,i}}}\right), \mathrm{i}=1,2 \end{aligned} \tag{3.18}$$

where

$$A_{\mathrm{sconj}} = \frac{G_{\mathrm{tag}}\lambda}{4\pi d_{\mathrm{TR}}} A_{\mathrm{tC}}, \tag{3.19}$$

$$\theta_{\mathrm{sconj}} = \theta_{\mathrm{tC}} - (\beta d_{\mathrm{TR}} + \frac{\pi}{2}), \tag{3.20}$$

$$\rho^*_{\mathrm{L,i}} = \left|\Gamma^*_{\mathrm{L,i}}\right|, 0 \le \rho^*_{\mathrm{L,i}} \le 1 \tag{3.21}$$

$$\theta^*_{\mathrm{L,i}} = \angle\Gamma^*_{\mathrm{L,i}}. \tag{3.22}$$

So without considering the other multipath and environmental field, the total electric field received by Rx tag is:

$$\mathbf{E}_{\mathrm{rxTot,i}} = \mathbf{i}_{\mathbf{l}_e} \left[A_{\mathrm{rC}} e^{j\theta_{\mathrm{rC}}} + A_{\mathrm{sconj}} e^{j\theta_{\mathrm{sconj}}} + A_{\mathrm{sconj}} \rho^*_{\mathrm{L,i}} e^{j\left(\theta_{\mathrm{sconj}}+\theta^*_{\mathrm{L,i}}\right)}\right] \tag{3.23}$$

$$= \mathbf{i}_{\mathbf{l}_e} \left(E_{\mathrm{CW}} + E_{\mathrm{sconj}} + \Gamma^*_{\mathrm{L,i}} E_{\mathrm{sconj}}\right) \tag{3.24}$$

$$= \mathbf{i}_{\mathbf{l}_e} \left(E_{\mathrm{CW}} + E_{\mathrm{sconj}} + E_{\mathrm{mod,i}}\right) \tag{3.25}$$

$$= \mathbf{i}_{\mathbf{l}_e} A_{\mathrm{rxTot,i}} e^{j\theta_{\mathrm{rxTot,i}}} \mathrm{i}=1,2. \tag{3.26}$$

In Eq. (3.25), the first two terms are CW signal and conjugate-matched structural scattering field, which are stationary fields during two modulation states when all other factors are fixed; the third term is the modulation signal, the change of which will cause the change of

total field at receiver side. The phasor form of signal superposition is shown in Fig. 3.9, the angle shift of smith chart can caused by phase shifting of transmission line and imaginary impedance of antenna. By either modulating the amplitude or phase of conjugate antenna reflection coefficient $\Gamma^*_{L,i}$, we can change the phase and amplitude of total signal seen by the receiver: the first modulation method is ASK modulation, and the second one is called PSK modulation. The envelop detector demodulate the signal by detecting the power difference between the total signal at two states.

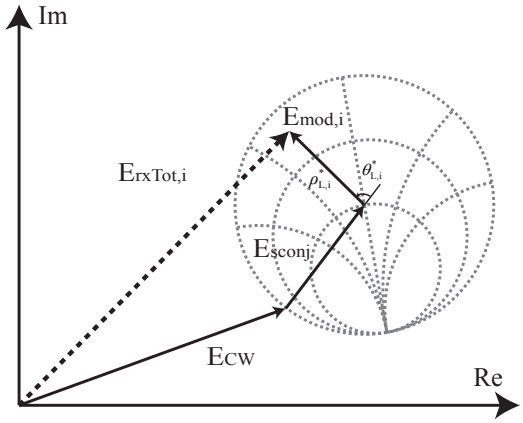

Figure 3.9: Phasor form of total received signal

However, any change on the environmental factors, like the relative positions of the three devices, radiation power of the CW signal and etc, will cause the change of first two "stationary" terms, which may lead the combination of fields to the positions that even $\Gamma^*_{L,i}$ modulates between two states, the amplitudes of total received power still remain constant. Then the envelop detector is not able to detect the difference of the signals. We call this situation as phase cancellation. Fig. 3.10 and 3.11 show the cases ASK modulation without and with the phase cancellation. PSK modulation also has the same problem, and the phasor illustration is shown in Fig. 3.12 and Fig. 3.13.

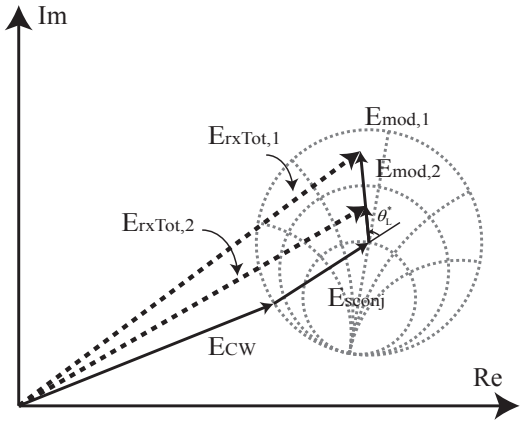

Figure 3.10: A phasor diagram of ASK modulation when there is no phase cancellation

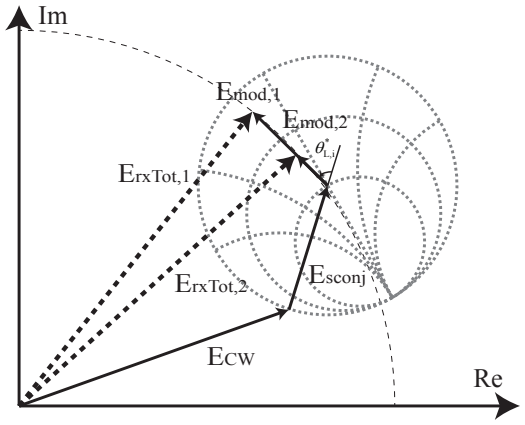

Figure 3.11: A phasor diagram of ASK modulation when there is phase cancellation

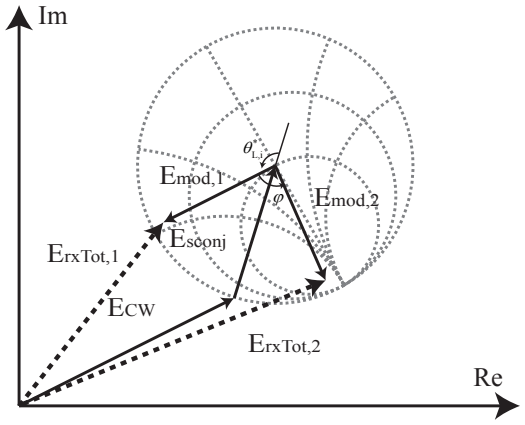

Figure 3.12: A phasor diagram of PSK modulation when there is no phase cancellation

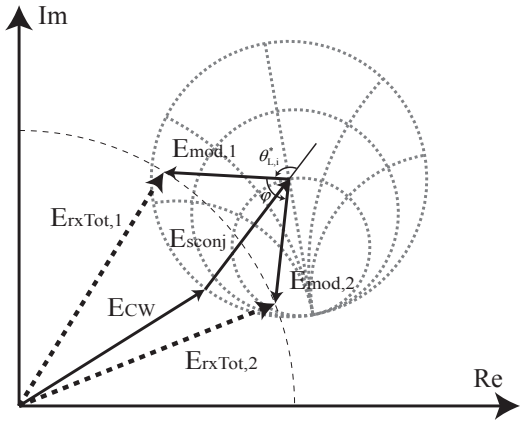

Figure 3.13: A phasor diagram of PSK modulation when there is phase cancellation

3.3.3 Enhanced multi-phase backscatter modulator design

To solve phase cancellation problem, some paper propose applying multiple antennas [15] to extract EM fields at different positions for different phases; the combination of the signal will appear power-difference to the detector. This is an effective method but will make the tag kind of bulky. Also when the CW frequency is low, the distance between the antennas need to be even longer to get enough phase difference. Our proposed solution is applying enhanced backscatter modulator with phase diversity introduced. The tag will backscatter the information through two different phase channel in two successive time slots with a deterministic phase difference θ_n between the two channels; then if there is phase cancellation happen in one channel, the other channel with phase shifting θ_n will avoid it as illustrated in Fig. 3.14.

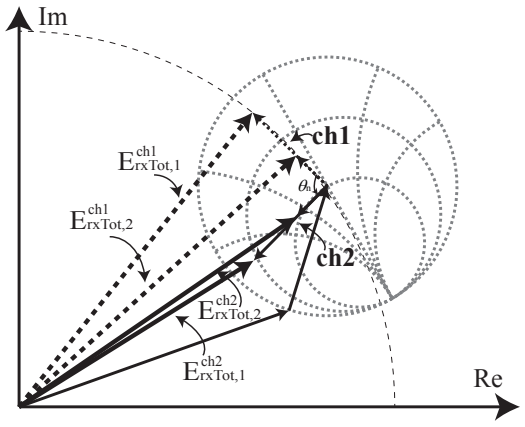

Figure 3.14: Solving phase cancellation problem by backscattering signal through difference phase channel

From Eq.(3.24), the complex differential total electric field on the Rx tag between two modulation states is

$$\Delta E_{\mathrm{rxTot}} = (\Gamma^*_{\mathrm{L},1} - \Gamma^*_{\mathrm{L},2}) E_{\mathrm{sconj}} = \Delta\Gamma^*_{\mathrm{L}} E_{\mathrm{sconj}}, \tag{3.27}$$

which is proportional to the differential conjugate antenna reflection coefficient $\Delta\Gamma_{\mathrm{L}}^{*}$, the phase of which can be determined by properly choosing the antenna load impedance $Z_{\mathrm{L,i}}$ at two states. To make two different phase channel, we just need to make

$$\Delta\Gamma_{\mathrm{L}}^{*\mathrm{ch2}} = \Delta\Gamma_{\mathrm{L}}^{*\mathrm{ch1}} e^{j\theta_n}. \tag{3.28}$$

According to [61], to obtain the largest amplitude differences in one channel when the other has phase cancellation, the best value for θ_n is $\pi/2$. Then we can map Γ_{L}^{*} to Smith Chart to get the modulation scheme needed for the two channel. To make the mapping more convenient, we will use power reflection coefficient γ_L defined by Kurokawa in [62]:

$$\gamma_{\mathrm{L,i}} = \frac{Z_{\mathrm{L,i}} - Z_A^*}{Z_{\mathrm{L,i}} + Z_A}, \mathrm{i} = 1, 2. \tag{3.29}$$

Then $\Gamma_{\mathrm{L}}^{*} = -\gamma_{\mathrm{L}}$, and $\Delta\Gamma_{\mathrm{L}}^{*} = -\Delta\gamma_{\mathrm{L}}$.

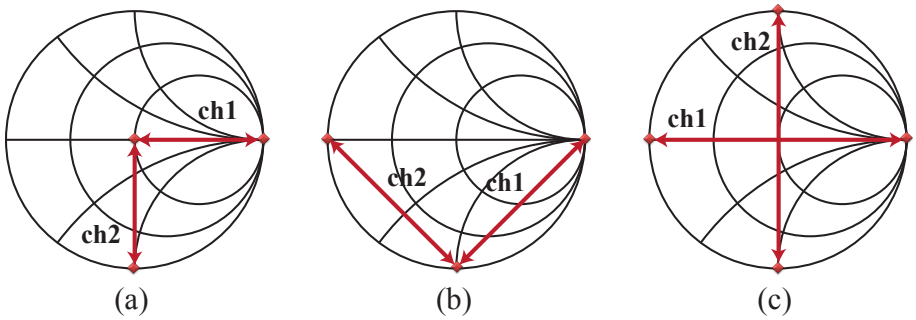

Figure 3.15: Three possible modulation schemes for two phase channels on normalized Smith charts in term of γ_L

Fig. 3.15 shows three possible modulation schemes for two phase channels on normalized Smith charts in term of γ_L. From the figure, it's very obvious that modulation scheme(c) maximize the backscatter signal strength by having the maximum amplitude of differential

Table 3.1: Reflection coefficient for 3 modulation schemes considered

	Channel 1			Channel 2		
	$\Delta\gamma_{\mathrm{L}}$	$\gamma_{\mathrm{L},1}$	$\gamma_{\mathrm{L},2}$	$\Delta\gamma_{\mathrm{L}}$	$\gamma_{\mathrm{L},1}$	$\gamma_{\mathrm{L},2}$
scheme (a)	$1e^{j0}$	0	1	$1e^{-j\frac{\pi}{2}}$	0	-j
scheme (b)	$\sqrt{2}e^{j\frac{\pi}{4}}$	-j	1	$\sqrt{2}e^{j\frac{3\pi}{4}}$	-j	-1
scheme (c)	$2e^{j0}$	-1	1	$2e^{j\frac{\pi}{2}}$	-j	j

power reflection coefficient $\Delta\gamma_L$. Semi-passive tag or passive tag with enough storage power before backscattering can apply scheme(c) to maximize the reading distance. However, for tag implemented on CMOS, it's very hard to yield large value inductors of good quality. In this case, scheme(b) can fulfill $\pi/2$ two phase channel by only requiring RC components. Scheme(c) is good for passive tags need to harvest operating power continuously from incident field. $\Delta\gamma_L$ for three modulation schemes are shown in Table.3.1 as well as corresponding $\gamma_{\mathrm{L,i}}$. After locating Γ^*_{L} or γ_{L}, we can get corresponding impedance by rearranging Eq. (3.2) or (3.29):

$$Z_{\mathrm{L}} = \frac{Z^*_A - Z_A\Gamma^*_{\mathrm{L}}}{1+\Gamma^*_{\mathrm{L}}} = \frac{Z^*_A + Z_A\gamma_{\mathrm{L}}}{1-\gamma_{\mathrm{L}}}. \tag{3.30}$$

Our prototype tag implement scheme(a) for the multiphase backscattering, and the antenna impedance is $Z_A = 50/\Omega$; so corresponding $Z^{\mathrm{ch1}}_{\mathrm{L},2}$ and $Z^{\mathrm{ch2}}_{\mathrm{L},2}$ are ∞ (open circuit) and $-j50$ ($C \approx 3.6$ pF for 915 MHz) respectively, and $Z^{\mathrm{ch1}}_{\mathrm{L},1} = Z^{\mathrm{ch2}}_{\mathrm{L},1} = 50\Omega$, which is realized by matched detector. More detail description about prototype implementing and experiment results will be shown in Ch. 3.5.

3.4 Co-design of detector and power harvesting

The power harvesting and the demodulator circuits are shown in the basic architecture of the BBTT tag in Fig. 1. A co-design of these circuits is very important due to their

interaction. Both the demodulation and the harvesting circuits are getting the power from a single line, and the amount of power each one gets will affect the performance of the other one. So, finding an optimum value for dividing the power ratio between these two circuits is critical in increasing the communication range between two tags.

For the energy harvesting circuit, in addition to selecting the Schottky diode, an important choice in the design for getting higher efficiency is the selection of the optimum number of diode stages. In principle, more stages provide higher voltage. However, in a low power environment, it has been shown that a few stages are more efficient than a larger number of stages [63]. To harvest enough power for the operation of the RF tag without the use of a storage element, it has been shown that the input power has to be around -15 dBm.

3.4.1 Low modulation depth problem

For the design of the demodulator circuit, we have to determine the modulation depth in the BBTT communication. To do that, we perform a link budget analysis. To make the analysis easier, we first assume that the CW signal is ubiquitous and identical all over the experimental environment under investigation, within which the BBTT tags receive the same input power P_{CW} from CW exciter. Also all the tags are located in each other's far field region so that Friis formula can be utilized here. One more hypothesis we are going to make is to neglect the phase cancellation problem and assume that all the backscatter signal received at the Rx tag are in phase with the CW signal. The backscattered power from the transmitter tag at a given modulation state is

$$P_{\mathrm{txBck,i}} = P_{\mathrm{CW}}|1 - \Gamma^{*}_{\mathrm{L,i}}|^2, \mathrm{i} = 1, 2 \tag{3.31}$$

where $\Gamma^*_{\mathrm{L,i}}$ is the aforementioned conjugate antenna reflection coefficient and can be calculated from equ. 3.2. By applying Friis formula the backscatter power arrives at Rx tag is:

$$P_{\mathrm{rxBck,i}} = \frac{P_{\mathrm{txBck,i}} G_{\mathrm{tag}}^2 \lambda^2}{(4\pi d_{\mathrm{TR}})^2}, \mathrm{i} = 1, 2 \tag{3.32}$$

where d_{TR} is the distance between the tags in communication. Superposing the excitation signal P_{CW} with the backscattering signal, the total power received by Rx tag is:

$$\begin{aligned} P_{\mathrm{rxTot,i}}(d_{\mathrm{TR}}) &= (\sqrt{P_{\mathrm{CW}}} + \sqrt{P_{\mathrm{rxBck,i}}})^2 \\ &= k_{\mathrm{i}}(d_{\mathrm{TR}}) P_{\mathrm{CW}}, \mathrm{i} = 1, 2. \end{aligned} \tag{3.33}$$

where

$$k_{\mathrm{i}}(d_{\mathrm{TR}}) = \left(1 + \frac{|1 - \Gamma^*_{\mathrm{L,i}}| G_{\mathrm{tag}} \lambda}{4\pi d_{\mathrm{TR}}}\right)^2, \mathrm{i} = 1, 2. \tag{3.34}$$

So the received baseband data power strength is proportional to P_{CW} the modulation depth m is only dependent of d_{TR}. The modulation depth m is:

$$m = \frac{|P_{\mathrm{rxTot,2}} - P_{\mathrm{rxTot,1}}|}{max\left(P_{\mathrm{rxTot,1}}, P_{\mathrm{rxTot,2}}\right)} \tag{3.35}$$

$$= \frac{|k_2(d_{\mathrm{TR}}) - k_1(d_{\mathrm{TR}})|}{max\left(k_1(d_{\mathrm{TR}}), k_2(d_{\mathrm{TR}})\right)} \tag{3.36}$$

For 915 MHz BBTT system with dipole tag antenna, the modulation depth m v.s the distance is shown in Fig. 3.16 when transmitter tag modulates its antenna load between open and conjugate match impedance, which shows the extremely low m (smaller than 0.1 or even 0.05) would happen to get reasonable communication range. In conventional RFID tag design it's very common to use voltage sensitivity in term of absolute input power difference γ (mV/μW) as the key performance indicator for the design. The diode has a square law

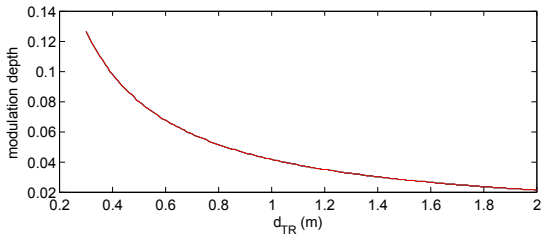

Figure 3.16: Detector schematic

characteristic at low incident power and a linear characteristic at higher incident power, with the intersection point commonly around -20 dBm. This is the reason why the demodulation circuit can perform well at very low power levels, around -30 dBm. However, in tag-to-tag communication scenario or the case when the power is split between the power harvesting circuit and the demodulation circuit, the input power to the demodulator circuit will be low and the diode operates at low power square region, but on the other hand, the difference between the modulated baseband signal power levels will also be lower, which may lead to the low output voltage. So to get rid of the impact of incident power, it's more convenient to define a new sensitivity indicator γ_{dBm} (mV/dBm) in term of power ratio to assess the performance of the demodulator circuit. For a fixed d_{TR}, the difference of power at Rx tag in dBm is:

$$\begin{aligned}\Delta P_{\mathrm{rxTot\_dBm}}(d_{\mathrm{TR}}) &= 10\log\left(\frac{P_{\mathrm{rxTot},1}(d_{\mathrm{TR}})}{1\mathrm{mW}}\right) - 10\log\left(\frac{P_{\mathrm{rxTot},2}(d_{\mathrm{TR}})}{1\mathrm{mW}}\right) \\ &= 10\log\left(\frac{k_1(d_{\mathrm{TR}})P_{\mathrm{CW}}}{1\mathrm{mW}}\right) - 10\log\left(\frac{k_2(d_{\mathrm{TR}})P_{\mathrm{CW}}}{1\mathrm{mW}}\right) \\ &= 10\log\left(\frac{k_1(d_{\mathrm{TR}})}{k_2(d_{\mathrm{TR}})}\right), \end{aligned} \tag{3.37}$$

which is independent of P_{CW}. Then from the transfer curve of a diode plotted at linear-log scale, it's very obvious that detector get better performance at high power level for BBTT

communication. A typical transfer curve of a Schottky diode is plotted in Fig. 3.17. Then we

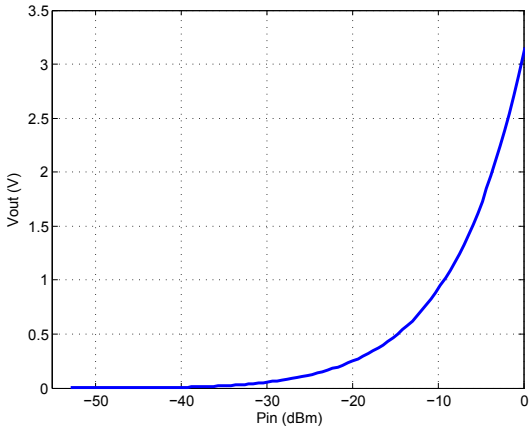

Figure 3.17: Transfer curve of voltage double with Schottky diode HSMS285c (RL = 100 kΩ)

need to find a balance between the power used for power harvesting and that for detector.

The sensitivity of the demodulator circuit depends on the selection of the values of the load capacitance C_L and load resistance R_L. The load capacitance and load resistance set the cutoff frequency of the low pass filter that determines the data rate. The increase of the load resistance will lead to a higher voltage at the output. On the other hand, the resistance of the load will be limited by the thermal noise. The minimum capacitance of the capacitor will be constrained by the ripple voltage.

3.4.2 Simulation result

In this section, we will demonstrate the co-design of the power harvesting and demodulator circuits for the optimal power transfer and the optimal voltage sensitivity of the demodulator circuit. The voltage sensitivity of the demodulator circuit is directly related to the communication range as shown in the previous section.

The energy harvesting and demodulator circuits were simulated using the Agilent Advanced Design System (ADS) software. For the energy harvesting, we used two stages of voltage multipliers because in the applications of BBTT tags the input power levels are low. We also assumed that optimal load was present at the output of the power harvesting circuit (which leads to maximum power efficiency). We examined the performance of the demodulator circuit with one and two stages of voltage multiplication. The matching circuits were employed to divide the incoming power between these two sections while the overall impedance was set at 50 Ω . The matching was achieved for input power of -15 dBm. The ratio of the input power of the demodulator and the power of the harvesting circuit was varied and had values 5%, 10%, 20%, and 50%. As the input power changed, due to mismatch in the impedances and the non-linear behavior of the diodes, the efficiency of the power harvesting and the voltage sensitivity changed. We also wanted to observe this effect for different input powers and the simulations were repeated for input powers of -10 dBm and -5 dBm. It is important to note that at these different input power levels, the ratio of input power of the demodulator and the power of the harvesting circuit would also change. The

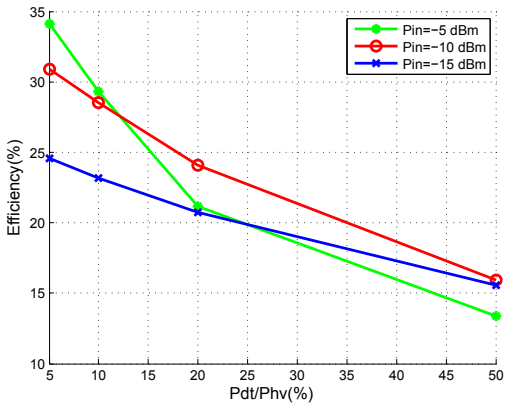

Figure 3.18: Ratio of harvested power over total input power as a function of the fraction of the input power transferred to the demodulator.

efficiency of the power energy harvesting circuit, that is, the ratio of harvested power and total input power, is shown in Fig. 3.18 as a function of the ratio of power division between the demodulator and the power harvesting circuit. The efficiency is also shown for different input power levels. For the optimized low input power of -15 dBm, we can see that the non-linearity of the diodes does not affect the performance, as the efficiency is almost linear with the power that is actually transferred to the power harvesting circuit. For the higher input powers, we can notice that the mismatch in the matching circuit and the non-linearity of the diodes significantly reduce the efficiency. The performance of the demodulator circuit is defined by its voltage sensitivity, i.e., by the voltage difference at the output of the demodulator circuit for a constant power difference at the input. From the simulations we obtained differences in output voltage levels for changes in the total input powers of 1 μW. The output voltage was obtained for different ratios in the power transferred to the demodulator circuit and for different levels of input power of -5 dBm, -10 dBm, and -15 dBm. The results are shown in Fig. 3.19. Fig. 3.20 shows the sensitivity over the power into the detector after splitting; and the sensitivity actually decease with the increasing power percentage, which follows the detection rule of diode that the sensitivity decrease when input power increase.

From these simulation results, we can first observe that the two stages of the voltage multiplication provide higher sensitivity as expected. When the power transferred to the demodulator circuit increases, due to the characteristic of the diode, the sensitivity is actually decreased. This effect is even more pronounced for higher input power levels. In the specific design that we investigated, we can conclude that the power ratio of 10% between the power transferred to the demodulator circuit and the power transferred to the power harvesting circuit is optimal. This ratio provides both high power efficiency and high voltage sensitivity.

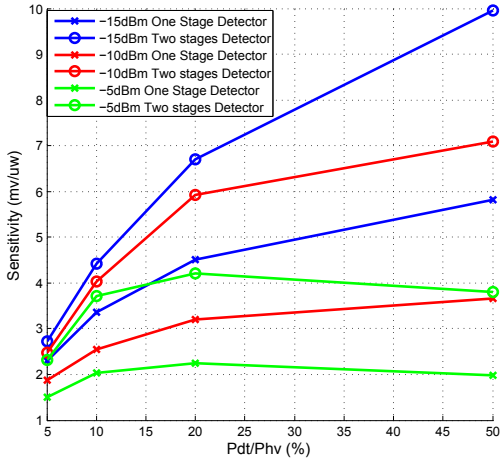

Figure 3.19: Sensitivity in term of total input power as a function of the fraction of the input power transferred to the demodulator.

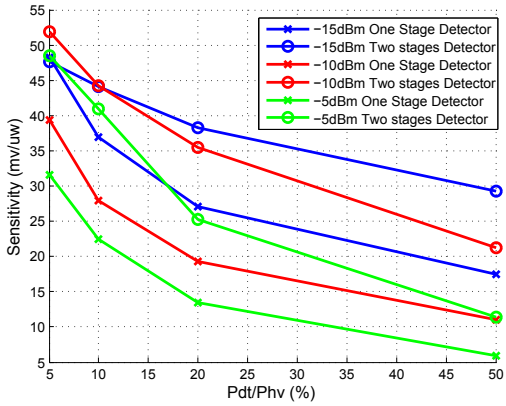

Figure 3.20: Sensitivity in term of detector input power as a function of the fraction of the input power transferred to the demodulator.

3.5 Prototype and experiment

3.5.1 Hardware description

The proof-of-concept BBTT tag is built up from commercially available off-the-shelf devices and composed by dipole antenna, modulator, detector, and a data processor - TI MSP430F2011 microcontroller. Each module is matched to 50 ohm - the common used standardized impedance for many microwave systems, so that optimization or replacement of individual modules can be very convenient. Right now, this BBTT prototype is powered by the a on-board battery, which will be replaced by individual power harvesting module in future version. The picture of prototype tag is shown in Fig. 3.23. Finished sensatag prototype boards successfully communicate with each other up to 1.3 meters at frequency 20 kHz when CW is around -17 dBm. We also give a small description of each module here.

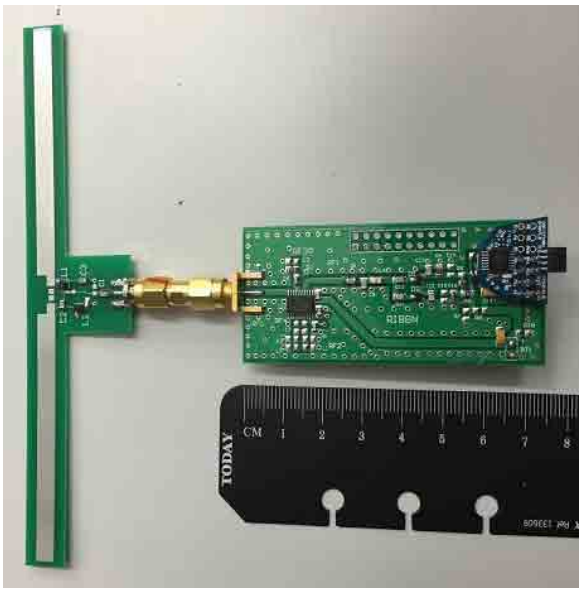

Figure 3.21: Proof-of-concept of BBTT tag

Dipole antenna

In order to communicate equally on every direction on horizontal plane, dipole antenna with its donut-shape radiation pattern is very suitable for our the application. To get its better radiation, a lumped LC balun deploys between the antenna and SMA connector.

Detector

We use voltage multiplier to demodulate ASK signal. The schematic of the detector circuit is as demonstrated in previous section in Fig. 3.4. Polarity of diode restrict the flowing direction of current, and the followed low pass filter (LPF) formed by C_4 and R_1 gets rid of carrier wave leaving only baseband signal. Since backscattering signal is not as strong as its counterpart sending from an active transmitter, 4-stage voltage multiplier applies here to boost up the receiving signal as well as extend the reading distance between the semi-passive tags. At the same time, increment of stage number reduces the input impedance of detector, which make it easier for impedance matching. Zero bias schottky diode HSMS-285x series from Avago Technology is a perfect option for our implementation.

By properly choosing C_4 and R_1 value, we make sure that inverse of their time constant much larger then carrier frequency 915 MHz and also much smaller than baseband frequency 20 kHz. Under this premise, large R_1 can also enlarge the received baseband signal. Second filter with large time constant generates average voltage for reference for the following ADC. Finally, a comparator with internal hysteresis is used as 1-bit ADC to transfer the received analog signal to digital signal to make sure that it can be recognized by MSP430.

In front of the whole detector module, the whole circuit will be matched by a "T"-shape matching network made of three lumped devices. S11 of matched detector is around -16 dBm.

Modulator

Modulator, which can also be viewed as passive transmitter of sensatag, modulates CW by changing the load impedance Z_L of the antenna. ADG 904 - a single pole 4 throw (SP4T) CMOS FET from Analog Devices is used here. One of the input terminals is connected to detector the impedance of which is matched to 50 Ω. As stated in previous section 3.3.3, the matched detector impedance serves as the matched impedance for modulation state 1 for both phase channel 1 and channel 2. One of the terminals is connected to 3.6 pF for $Z_{\mathrm{L},2}^{\mathrm{ch2}}$, then one of the left empty terminals is used as the open circuit for $Z_{\mathrm{L},2}^{\mathrm{ch1}}$.

3.5.2 Simulation and experiment result

Based on previous derived equations, we present a simulation results that demonstrate the phase cancellation phenomenon and how proposed solution affect the communication outcome. Then a similar lab experiment is conducted with BBTT prototype tag described above.

In the simulation, the transmitting power of CW exciter is 13 dBm, G_{CW} and G_{tag} is set at 6 dBi and 2.2 dBi respectively, and for G_{CW} there is also 2 dB power loss on antenna cable. The resistance of CW antenna can be calculated by its VSWR provided by the antenna data sheet. The relative position between the CW exciter and two tags is shown in Fig. 3.22. The position of CW exciter and Rx tag are fixed, while Tx tag is moving away from the Rx tag, then the distances between each other can be calculated from the parameters stated on the figure. By using the equations from previous section, the difference between the power at two modulation states for two phase channel can be calculated. Simulation in section 3.4.2 implies that the detection sensitivity in this situation is between 10 mV/μW to 20 (mV/μW), then we can get the simulated output analog voltage. The result of amplitude

of output voltage difference is shown in Fig. 3.24. The experiment result with similar setup is conducted, the output analog voltage is recorded by ADS8860EVM - a evaluation module for a 16-bit SAR ADC from Texas Instrument. Amplitude as well as polarity of the voltage are recorded. Data at positions as many as possible is recorded, but it's very hard to catch all the null point where phase cancellation happened. So we add zero point in the middle of the positions as interpolation when the polarity of output voltage flipped. The amplitude of measurement result is shown in Fig. 3.25, and the experiment setup is shown in Fig. 3.23.

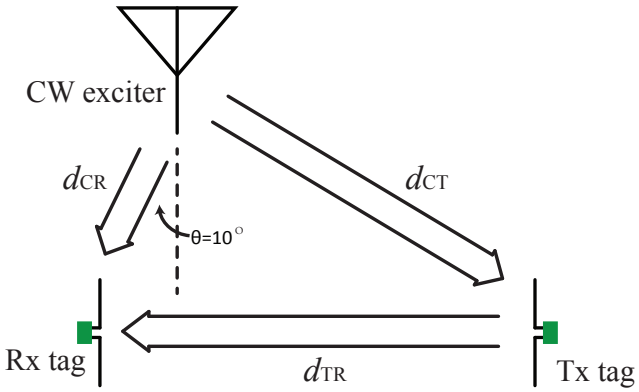

Figure 3.22: Illustration of relative position of CW exciter and two tags in both simulation and experiment

Our attention is mainly placed on the curve of the plot, since the simulation is based on the most ideal scenario, and all the power losses, including insertion loss through switch, matching circuit, polarization loss of the antennas, especially the angle mismatch of the antenna gain, is not considered, the simulation result is much larger than the experiment result. But the curve of the experiment, as well as the distances between the null point and relative position of null point and maximum amplitudes, still agree with the simulation quite well. Both the simulation and experiment result show the phase cancellation problem for BBTT systems and proposed solution for solving it.

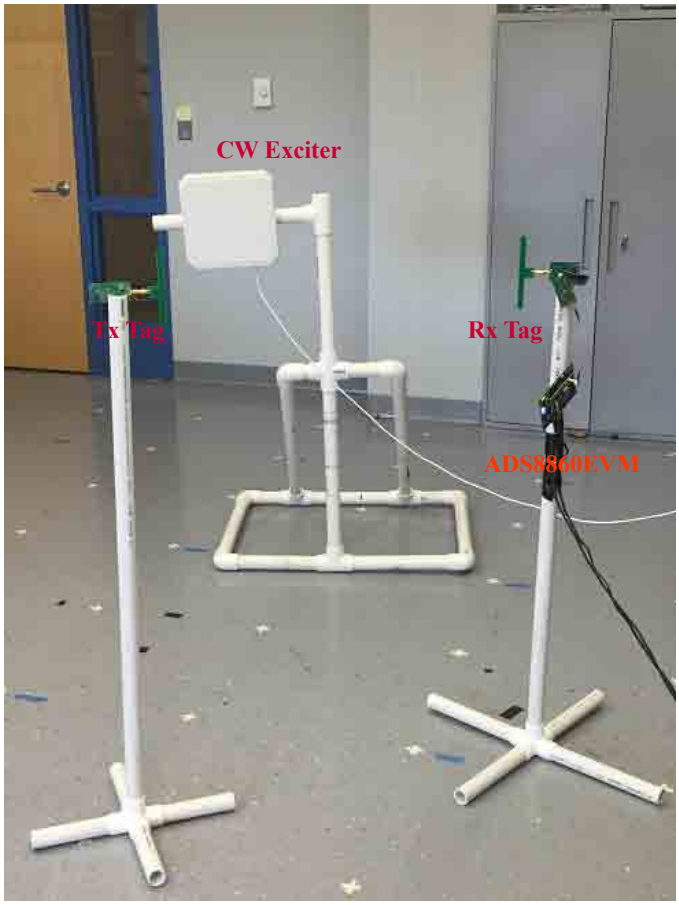

Figure 3.23: Experiment setup for analog output recording of two phase channel

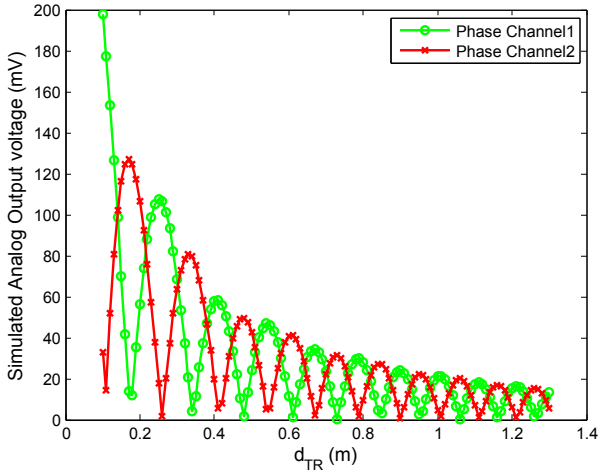

Figure 3.24: Simulated output analog voltage when two phase channel is applied in the BBTT system

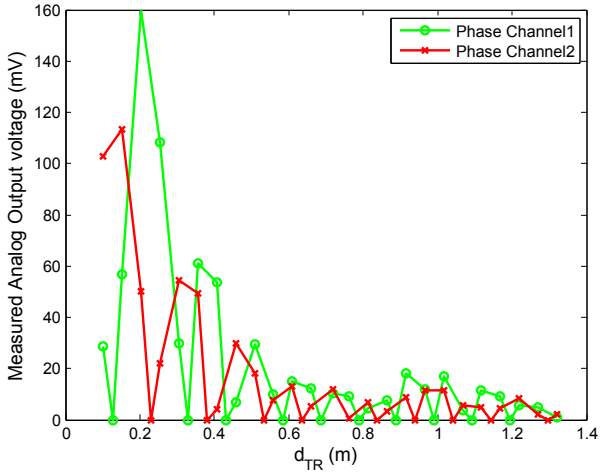

Figure 3.25: Experimental output analog voltage when two phase channel is applied in the BBTT system

3.6 Conclusions

In this chapter we talk about the hardware design and optimization for tags in backscattered-based tag-to-tag communication system. The optimization of the performances of tag architecture modules including analog front end (AFE) and the backscatter modulator (BM) in order to achieve increased communication ranges under scarce energy resources is very critical. The BBTT tag architecture is first being reviewed and compare with the hardware design for RFID tags. Then we analyze mathematically the phase cancellation problem existing exclusively in BBTT system and proposed multiphase backscattering as the solution for this problem. Demonstration of co-design of the power harvesting and demodulator circuit has been shown to enable co-optimization of the power efficiency and the voltage sensitivity of the demodulator that will ultimately extend the communication range for BBTT system. At last, a BBTT tag prototype is illustrated and a conducted experiment about phase cancellation with prototype is shown.

Chapter 4

Conclusion and Future Work

This work has focused on two of the critical subjects in the passive devices technology: wireless power transfer (WPT) and data link, and addressed these two subjects from two distinct applications: design of wireless power transfer for IMDs and hardware design & optimization for backscatter-based tag-to-tag (BBTT) communication system.

Chapter 2 discussed the design of the inductive wireless power link (WPT) for implantable devices with small coil sizes and relatively long reading distances, and optimized both coils to achieve maximum delivered power for IMD under rigorous constraints. First we briefly introduced the fundamentals of the EM propagation, including Maxwell's equations, constitutive relations and EM properties of human tissue, and discussed two major analysis methods used in wireless power link design: quasi-static analysis based on closed-form equations and full-wave analysis based on numerical simulation. Then we address different issues during WPT link design, including two kinds of possible misalignment existing between transmitting coil and receiving coil, the maximum transmitting efficiency, safety issue regarding EM field exposure and the related maximum available power for the implantable devices. After talking about the issues, we combined these two aforementioned analysis

methods together to analyze power link from two different aspects respectively: maximizing power transmission efficiency and maximizing delivered power to IMD. Three matching techniques: resonant matching, simultaneously conjugate matching and maximum efficiency matching, which are three commonly used methods to achieve high transfer efficiency, have been introduced briefly. Closed-form equations for coil model based on quasi-static analysis were also introduced. However due to the restricted suitability of quasi-static analysis at low frequencies, our following analysis mainly relied on the full-wave analysis enabled by the use of the EM simulator Ansoft HFSS.

We investigated the optimum operating frequency for coil pairs with different parameters to achieve optimum efficiency. and found the qualitative relationship between these parameters and optimum efficiency and frequency. Based on these result, our attention was focused on the 5 cm Tx coil and operating frequency of 40.68 MHz. Besides evaluating the optimum frequency for optimum efficiency between the two coils, we proposed delivering maximum possible power to implantable devices by adjusting the position of Tx coil. Then we investigate the an adaptive transmitter coil array and evaluate the performance of the WPT link, from the perspective of both efficiency and maximum deliverable power, to see how the link characteristic changed with the modification of the coil structure and driving sources with various phase. We found that by adjusting the arrangement of the coil array and controlling the phase difference between the current sources, the SAR generated on the tissue and be successfully reduce and both positional and rotational misalignment between the two coils can be mitigated. After that, different types of rectifier for power harvesting through EM field for IMDs was being discussed.

Then in Chapter 3, we talk about a novel, low power and low lost communication system - backscatter-based tag-to-tag (BBTT) communication systems, wherein the tags communicate with each other by backscattering an external environmental EM field, without on-board

active radio device. In this chapter, after brief description of the communication diagram for BBTT system and its promising application in extending scalability and capability of Internet of Thing (IoT) after being combined with multihop communication, we review the basic circuit modules for BBTT tag hardware design, and compare it with conventional RFID tag design. We found that due to the different communication mechanism and objects, the design strategy and standard for general BBTT tags are quite different from RFID tag design, where the communication object for tags are active RFID reader and corresponding framework is centered on reader.

First, we investigate phase cancellation problem, the phenomenon of loss of baseband signal existing uniquely and ubiquitously in general BBTT communication system. To reduce power consumption of circuit and manufacture cost, general BBTT tags utilize passive envelop detector as receiver, which can only receive the signal by detecting power incident power difference. However, there is certain possibility that the combination of CW signal and backscattered signals at different modulation states may appear the same power which is hard to be differentiated under passive detection. To evaluate this problem, instead of viewing it from power perspective, we do the mathematical communication link analysis from EM field perspective. We first review the scattering theory of antenna, and derive the analytical equations for describing the EM fields in the environment under investigation and characterizing the communication link. Then according to the properties of the field performance, we proposed a solution of multiphase backscattering, and brought up three enhanced modulation scheme based on this idea. After that a simulation for a BBTT systems with two tags is carried out.

Second, we also review the analog front end (AFE) in BBTT tags design, which is another critical part in determining the robustness and range of a passive tag-to-tag link. We did the linkbudget analysis for a general BBTT link and evaluate the received signal with low

modulation depth in BBTT system. Then we demonstrate the co-design of the power harvesting and demodulator circuit to enable co-optimization of the harvester power efficiency and the voltage sen- sitivity of the receiver that will ultimately extend the communication range for BBTT system. A RF circuit simulator Advanced Design System (ADS) is used here to facilitate the optimization.

In last part of Chapter 3, a BBTT tag prototype is demonstrated and a conducted experiment about phase cancellation with this prototype is shown. We compare the experiment result with the simulation result based on aforementioned field expression, and both the simulation and experiment result showed the phase cancellation problem for BBTT systems and proved that proposed multiphase backscattering is a good solution for it.

In the future work, for WPT link design, we will try to further optimize the wireless link by utilizing and adjusting the structure of adaptive transmitting coil array. The demo coil array based on that will be fabricated as planar spiral PCB coils and the wireless link will be measured and characterized to demonstrate a working proof-of-concept system. For BBTT tag design, a IoT network based of BBTT system in conjunction with multihoping network will be finished, bit error rate (BER) of passive tag link will be evaluated and demonstrate the reliability of using multiphase backscattering. Then the power harvesting module will be designed and added into the prototype to further consummate its function.

Appendix A

EM wave equations and constitutive relations

This section will outline some basic concepts of EM theory which will be essentially important in understanding of the inductive link modeling and will be used in future illustration and discussion of the differences between quasi-static analysis and full-wave analysis.

For time-harmonic EM field at constant frequency, Maxwell's equations can be expressed in phasor form in frequency domain as:

$$\nabla \times \mathbf{E} = -j\omega\mathbf{B} \tag{A.1a}$$

$$\nabla \times \mathbf{H} = j\omega\mathbf{D} + \mathbf{J} \tag{A.1b}$$

$$\nabla \cdot \mathbf{D} = \rho \tag{A.1c}$$

$$\nabla \cdot \mathbf{B} = 0 \tag{A.1d}$$

where:

E is the electric field (V/m);

H is the magnetic field (A/m);

D is the TEST magnetic field (A/m);

and ω in unit rad/s is the angular frequency of the field.

(A.1a) and (A.1b) are known as Faraday's law and Maxwell - Ampere's law, (A.1c) and (A.1d) are electric and magnetic forms of Gauss's law. These quantities are connected by constitutive relations which describes the properties of the surrounding medium. For isotropic and linear materials, these constitutive relations are:

$$\mathbf{D} = \epsilon_0 \epsilon_r \mathbf{E} = \epsilon \mathbf{E} \tag{A.2a}$$

$$\mathbf{B} = \mu_0 \mu_r \mathbf{H} = \mu \mathbf{H} \tag{A.2b}$$

$$\mathbf{J} = \sigma \mathbf{E} \tag{A.2c}$$

where $\epsilon_0 = 8.854 \times 10^{-12}$ F/m, $\mu_0 = 4\pi \times 10^{-7}$ H/m are the permittivity and permeabililty of free space; and ϵ_r, μ_r and σ are the relative permittivity, relative permeability and conductivity of the material respectively. Being treated as dielectric and nonmagnetic material, relative permeability of biological tissue is approximated as 1, while the relative permittivity of the different tissues has large variations.

For a typical lossy dielectric material, the general form of complex relative permittivity is expressed as:

$$\epsilon_r = \epsilon' - j\epsilon'' \tag{A.3}$$

where the real part of the complex permittivity ϵ' is the relative permittivity of the material, the imaginary part of it, $-\epsilon''$, represent energy dissipation due to the vibration of dipole moments caused by applied electric field **E**. ϵ'' must be positive to ensure energy conservation. Applying (A.2c) and (A.3) into (A.1b), we can make some transformation on Maxwell's curl

equation:

$$\begin{aligned}\nabla \times \mathbf{H} &= j\omega\epsilon_0\epsilon_r\mathbf{E} + \sigma\mathbf{E} \\ &= j\omega\epsilon_0\left(\epsilon' - j\epsilon''\right)\mathbf{E} + \sigma\mathbf{E} \\ &= j\omega\epsilon_0\left(\epsilon' - j\epsilon'' - j\frac{\sigma}{\omega\epsilon_0}\right)\mathbf{E}, \end{aligned} \tag{A.4}$$

Then we can treat

$$\epsilon_{tot} = \epsilon' - j\left(\epsilon'' + \frac{\sigma}{\omega\epsilon_0}\right) \tag{A.5}$$

as the total complex relative permittivity which describes the entire dielectric properties of biological tissue. The term $\sigma_{eff} = \omega\epsilon_0\epsilon'' + \sigma$ can be considered as total effective conductivity of the material.

Appendix B

Network parameters

General behavior of networks can be described by different set of parameters, like Z-parameters, Y-parameters, S-parameter, etc. Here we will just introduce two types of parameters that are closely related to our work: Z-parameters and S-parameters.

The Z-parameters, also named impedance-parameters, describe the network behavior in terms of voltage and current at each port. For a 2-port network shown in Fig.B.1, the V-I characteristics expressed in Z-parameters are:

$$V_1 = Z_{11}I_1 + Z_{12}I_2 \tag{B.1a}$$

$$V_2 = Z_{21}I_1 + Z_{22}I_2 \tag{B.1b}$$

where Z_{ij} is the element in Z-parameters matrix. It is not hard to find that these expressions are very similar with V-I equations for transformer model that we stated above. Actually transformer model presents a special case of a general two-port network, with all impedance elements being purely inductive.

As the voltages and currents are not easy to measure for a microwave circuit operating

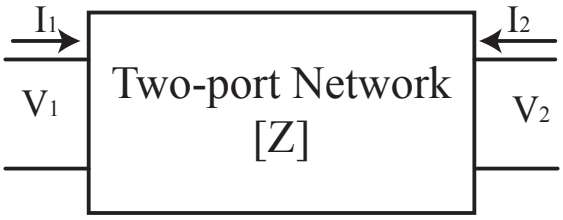

Figure B.1: Two-port network described by Z-parameters

under high frequencies, measuring the impedances of the 2-port network is also challenging. At the range of high frequencies, the concepts of wave traveling or power flow are more practical in the measurements; then the corresponding parameters delineating the power behavior of a network, scattering-parameters (S-parameters), are used.

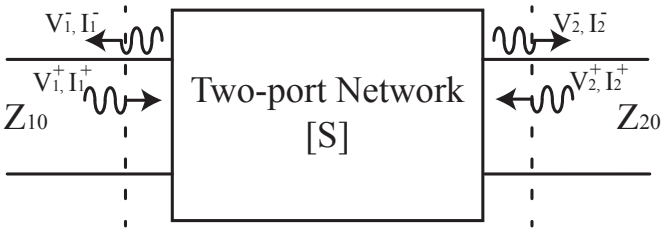

Figure B.2: Two-port network described in S-parameters

For a general microwave network, total voltage and current on an arbitrary port n can be divided into the incident and reflected parts[32]:

$$V_n = V_n^+ + V_n^- \tag{B.2a}$$

$$I_n = \frac{V_n^+ - V_n^-}{Z_{n0}}, \tag{B.2b}$$

where Z_{n0} is the characteristic impedance of the port n; V_n^+ and V_n^- are associated with incident wave and reflected wave at each port. Fig.B.2 shows this concept for a general two-port network. Then S-parameters are defined using these divided components of voltage,

and the expressions for two-port network with S-parameters are

$$V_1^- = S_{11}V_1^+ + S_{12}V_2^+ \tag{B.3a}$$

$$V_2^- = S_{21}V_1^+ + S_{22}V_2^+. \tag{B.3b}$$

S-parameters can be measured directly through a vector network analyzer (VNA) by measuring the transmitted and reflected power directly, thus are very popular in microwave components design. For more information about S-parameters, one can refer to [32][62].

Bibliography

[1] W. Greatbatch and C. Holmes, "History of implantable devices," *Engineering in Medicine and Biology Magazine, IEEE*, vol. 10, no. 3, pp. 38–41, 1991.

[2] J. Olivo, S. Carrara, and G. De Micheli, "Energy harvesting and remote powering for implantable biosensors," *Sensors Journal, IEEE*, vol. 11, no. 7, pp. 1573–1586, 2011.

[3] P. Mitcheson, E. Yeatman, G. Rao, A. Holmes, and T. Green, "Energy harvesting from human and machine motion for wireless electronic devices," *Proceedings of the IEEE*, vol. 96, no. 9, pp. 1457–1486, 2008.

[4] P. Miao, P. D. Mitcheson, A. S. Holmes, E. M. Yeatman, T. C. Green, and B. H. Stark, "Mems inertial power generators for biomedical applications," *Microsyst. Technol.*, vol. 12, no. 10, pp. 1079–1083, Aug. 2006.

[5] M. Strasser, R. Aigner, C. Lauterbach, T. Sturm, M. Franosh, and G. Wachutka, "Micromachined cmos thermoelectric generators as on-chip power supply," in *TRANSDUCERS, Solid-State Sensors, Actuators and Microsystems, 12th International Conference on, 2003*, vol. 1, 2003, pp. 45–48 vol.1.

[6] S. Kerzenmacher, J. Ducre, R. Zengerle, and F. von Stetten, "Energy harvesting by implantable abiotically catalyzed glucose fuel cells," *Journal of Power Sources*, vol. 182, no. 1, pp. 1 – 17, 2008.

[7] N. Tesla, "The transmission of electric energy without wires," *Electrical World and Engineer*, 1904.

[8] J. C. Schuder, H. E. J. Stephenson, and J. F. Townsend, "High-level electromagnetic energy transfer through a closed chest wall," *IRE Intl. Conv. Rec*, vol. 9, pp. 119–126, 1961.

[9] J. Schuder, J. Gold, H. Stoeckle, and J. Holland, "The relationship between the electric field in a semi-infinite conductive region and the power input to a circular coil on or above the surface," *Medical and biological engineering*, vol. 14, no. 2, pp. 227–234, 1976.

[10] F. Flack, E. James, and D. Schlapp, "Mutual inductance of air-cored coils: Effect on design of radio-frequency coupled implants," *Medical and biological engineering*, vol. 9, no. 2, pp. 79–85, 1971.

[11] W. J. Heetderks, "Rf powering of millimeter- and submillimeter-sized neural prosthetic implants," *Biomedical Engineering, IEEE Transactions on*, vol. 35, no. 5, pp. 323–327, 1988.

[12] W. Ko, S. Liang, and C. Fung, "Design of radio-frequency powered coils for implant instruments," *Medical and Biological Engineering and Computing*, vol. 15, no. 6, pp. 634–640, 1977.

[13] P. Nikitin, S. Ramamurthy, R. Martinez, and K. Rao, "Passive tag-to-tag communication," in *RFID (RFID), 2012 IEEE International Conference on*, April 2012, pp. 177–184.

[14] G. Marrocco and S. Caizzone, "Electromagnetic models for passive tag-to-tag communications," *Antennas and Propagation, IEEE Transactions on*, vol. 60, no. 11, pp. 5381–5389, Nov 2012.

[15] B. Kellogg, A. Parks, S. Gollakota, J. R. Smith, and D. Wetherall, "Wi-fi backscatter: Internet connectivity for rf-powered devices," in *Proceedings of the 2014 ACM Conference on SIGCOMM*, ser. SIGCOMM '14. ACM, 2014, pp. 607–618.

[16] V. Liu, A. Parks, V. Talla, S. Gollakota, D. Wetherall, and J. R. Smith, "Ambient backscatter: Wireless communication out of thin air," *SIGCOMM Comput. Commun. Rev.*, vol. 43, no. 4, pp. 39–50, Aug. 2013.

[17] A. Athalye, V. Savic, M. Bolic, and P. Djuric, "Novel semi-passive rfid system for indoor localization," *Sensors Journal, IEEE*, vol. 13, no. 2, pp. 528–537, Feb 2013.

[18] P. Djurić and A. Athalye, "Rfid system and method for localizing and tracking a moving object with an rfid tag," U.S. Patent 7 812 719, Oct 12, 2010. [Online]. Available: http://www.google.com/patents/US7812719

[19] A. Athalye, V. Savic, M. Bolic, and P. Djuric, "A radio frequency identification system for accurate indoor localization," in *Acoustics, Speech and Signal Processing (ICASSP), 2011 IEEE International Conference on*, May 2011, pp. 1777–1780.

[20] U.-M. Jow and M. Ghovanloo, "Design and optimization of printed spiral coils for efficient transcutaneous inductive power transmission," *IEEE Trans. Biomed. Circuits Syst.*, vol. 1, no. 3, pp. 193 –202, Sep. 2007.

[21] R. Harrison, "Designing efficient inductive power links for implantable devices," in *Circuits and Systems, 2007. ISCAS 2007. IEEE International Symposium on*, 2007, pp. 2080–2083.

[22] "An inductive power link for a wireless endoscope," *Biosensors and Bioelectronics*, vol. 22, no. 7, pp. 1390 – 1395, 2007.

[23] A. Poon, S. O'Driscoll, and T. Meng, "Optimal operating frequency in wireless power transmission for implantable devices," in *Engineering in Medicine and Biology Society, 2007. EMBS 2007. 29th Annual International Conference of the IEEE*, 2007, pp. 5673–5678.

[24] ——, "Optimal frequency for wireless power transmission into dispersive tissue," *IEEE Antennas Propag. Mag.*, vol. 58, no. 5, pp. 1739 –1750, May 2010.

[25] M. Mark, T. Bjorninen, Y. Chen, S. Venkatraman, L. Ukkonen, L. Sydanheimo, J. Carmena, and J. Rabaey, "Wireless channel characterization for mm-size neural implants," in *Engineering in Medicine and Biology Society (EMBC), 2010 Annual International Conference of the IEEE*, 2010, pp. 1565–1568.

[26] J. Rabaey, M. Mark, D. Chen, C. Sutardja, C. Tang, S. Gowda, M. Wagner, and D. Werthimer, "Powering and communicating with mm-size implants," in *Design, Automation Test in Europe Conference Exhibition (DATE), 2011*, 2011, pp. 1–6.

[27] M. Zargham and P. Gulak, "Maximum achievable efficiency in near-field coupled power-transfer systems," *Biomedical Circuits and Systems, IEEE Transactions on*, vol. 6, no. 3, pp. 228–245, 2012.

[28] S. Gabriel, R. Lau, and C. Gabriel, "The dielectric properties of biological tissues: Iii. parametric models for the dielectric spectrum of tissues," *Phys. Med. Biol.*, vol. 41, pp. 2271 –2293, 1996.

[29] J. Larsson, "Electromagnetics from a quasistatic perspective," *Am. J. Phys.*, vol. 75, no. 3, pp. 230 –239, Mar. 2007.

[30] T. H. Lee, *The Design of CMOS Radio-Frequency Integrated Circuits*, 2nd ed. Cambridge University Press, 2004.

[31] U.-M. Jow and M. Ghovanloo, "Modeling and optimization of printed spiral coils in air, saline, and muscle tissue environments," *IEEE Trans. Biomed. Circuits Syst.*, vol. 3, no. 5, pp. 339–347, 2009.

[32] D. M. Pozar, *Microwave Engineering*, 3rd ed. John Wiley & Sons, 2005.

[33] B. Lenaerts and R. Puers, *Omnidirectional Inductive Powering for Biomedical Implants*. New York: Springer, 2009.

[34] A. R. A. V. Vorst and Y. Kotsuka, *RF/Microwave Interaction with Biological Tissues*. New Jersey, USA: Wiley-IEEE Press, 2006.

[35] A. Christ, M. Douglas, J. Nadakuduti, and N. Kuster, "Assessing human exposure to electromagnetic fields from wireless power transmission systems," *Proceedings of the IEEE*, vol. 101, no. 6, pp. 1482–1493, 2013.

[36] ICNIRP, "Guidelines for limiting exposure to time0varying electric, magnetic and electromagnetic fields (up to 300ghz)," *Health Phys.*, vol. 74, pp. 494 –522, 1998.

[37] *IEEE Standard for Safety Levels With Respect to Human Exposure to Radio Frequency Electromagnetic Fields, 3 kHz to 300 GHz*, 2006.

[38] N. C. on Radiation Protection (NCRP), "Biological effects and exposure criteria for radiofrequency electromagnetic fields," NCRP, Rep. 086, 1986.

[39] "Ieee standard for safety levels with respect to human exposure to radio frequency electromagnetic fields, 3 khz to 300 ghz," *IEEE Std C95.1-1992*, 1992.

[40] K. Fotopoulou and B. Flynn, "Optimum antenna coil structure for inductive powering of passive rfid tags," in *RFID, 2007. IEEE International Conference on*, 2007, pp. 71–77.

[41] M. Mark, "Powering mm-size wireless implants for brain-machine interfaces," Ph.D. dissertation, Univ. of California at Berkeley, 2011.

[42] C. Zierhofer and E. Hochmair, "Geometric approach for coupling enhancement of magnetically coupled coils," $IEEE_{JB}ME, vol.\ 43, no.\ 7, pp.708 - -714, 1996.$

[43] E. B. Rosa, "The self and mutual inductance of linear conductors," in *Bulletin of the National Bureau of Standards*.

[44] F. W. Grover.

[45] H. Greenhouse, "Design of planar rectangular microelectronic inductors," *Parts, Hybrids, and Packaging, IEEE Transactions on*, vol. 10, no. 2, pp. 101–109, Jun 1974.

[46] A. Ruehli, "Inductance calculations in a complex integrated circuit environment," *IBM Journal of Research and Development*, vol. 16, no. 5, pp. 470–481, Sept 1972.

[47] K. Finkenzeller, *RFID Handbook*, 2nd ed. John Wiley Sons, 2003.

[48] B. Park, S. Rajan, J. Guag, and L. Angelone, "A novel method to decrease electric field and sar using an external high dielectric sleeve at 3 t head mri: Numerical and experimental results," *Biomedical Engineering, IEEE Transactions on*, vol. 62, no. 4, pp. 1063–1069, April 2015.

[49] B. Park, A. G. Webb, and C. M. Collins, "A method to separate conservative and magnetically-induced electric fields in calculations for {MRI} and {MRS} in electrically-small samples," *Journal of Magnetic Resonance*, vol. 199, no. 2, pp. 233 – 237, 2009.

[50] M. Ghovanloo and K. Najafi, "Fully integrated wideband high-current rectifiers for inductively powered devices," *IEEE J. Solid-State Circuits*, vol. 39, no. 11, pp. 1976–1984, Nov. 2004.

[51] C. Sauer, M. Stanacevic, G. Cauwenberghs, and N. Thakor, "Power harvesting and telemetry in cmos for implanted devices," *IEEE Trans. Circuits Syst. I*, vol. 52, no. 12, pp. 2605–2613, Dec. 2005.

[52] F. Kocer, P. Walsh, and M. Flynn, "An injection locked, rf powered, telemetry ic in 0.25 mu;m cmos," in *VLSI Circuits, 2004. Digest of Technical Papers. 2004 Symposium on*, Jun. 2004, pp. 24–27.

[53] Q. Fu, N. Gay, C. Bansleben, R. Hildebrand, M. Heiss, A. Turke, and W.-J. Fischer, "Optimization of the nmos and pmos gate cross-connected rectifier for rf power extraction in rfid applications," in *Microwave Conference, 2008. APMC 2008. Asia-Pacific*, dec. 2008, pp. 1–4.

[54] T. Bhatti and F. Bhatti, "Charged based mos transistor modeling in weak inversion," in *Electro/Information Technology, 2008. EIT 2008. IEEE International Conference on*, May 2008, pp. 294–299.

[55] D. M. Dobkin, *The RF in RFID: UHF RFID in Practice*. Newnes, 2007.

[56] P. V. Nikitin, K. Rao, and R. Martinez, "Differential rcs of rfid tag," *Electronics Letters*, vol. 43, no. 8, pp. 431–432, 2007.

[57] C. A. Balanis, *Antenna Theory*. John Wiley Sons, Inc., 2005.

[58] R. Hansen, "Relationships between antennas as scatterers and as radiators," *Proceedings of the IEEE*, vol. 77, no. 5, pp. 659–662, May 1989.

[59] ——, "Relationships between antennas as scatterers and as radiators," *Proceedings of the IEEE*, vol. 77, no. 5, pp. 659–662, May 1989.

[60] F. Fuschini, C. Piersanti, F. Paolazzi, and G. Falciasecca, "Analytical approach to the backscattering from uhf rfid transponder," *Antennas and Wireless Propagation Letters, IEEE*, vol. 7, pp. 33–35, 2008.

[61] Z. Shen, A. Athalye, and P. Djurić, "Phase cancellation in backscatter-based tag-to-tag communication systems," *Internet of Things Journal, IEEE*, submitted for publication.

[62] K. Kurokawa, "Power waves and the scattering matrix," *Microwave Theory and Techniques, IEEE Transactions on*, vol. 13, no. 2, pp. 194–202, 1965.

[63] B. Marshall, M. Morys, and G. Durgin, "Parametric analysis and design guidelines of rf-to-dc dickson charge pumps for rfid energy harvesting," in *RFID (RFID), 2015 IEEE International Conference on*, April 2015, pp. 32–39.